Computer Simulation of an Excess Proton in Aqueous Systems

Amani Naser Tahat

Departament de Fisica
Universitat Politecnica de Catalunya - Barcelona Tech

Dissertation of the doctoral thesis supervised by

Dr. Jordi Marti

2016

UNIVERSITAT POLITÈCNICA DE CATALUNYA
BARCELONATECH
Escola de Doctorat

Acta de calificación de tesis doctoral	Curso académico:

Nombre y apellidos

Programa de doctorado

Unidad estructural responsable del programa

Resolución del Tribunal

Reunido el Tribunal designado a tal efecto, el doctorando / la doctoranda expone el tema de la su tesis doctoral titulada

____

____

____

Acabada la lectura y después de dar respuesta a las cuestiones formuladas por los miembros titulares del tribunal, éste otorga la calificación:

☐ NO APTO ☐ APROBADO ☐ NOTABLE ☐ SOBRESALIENTE

(Nombre, apellidos y firma) Presidente/a	(Nombre, apellidos y firma) Secretario/a

(Nombre, apellidos y firma) Vocal	(Nombre, apellidos y firma) Vocal	(Nombre, apellidos y firma) Vocal

_________________________, ________ de ____________________ de ________________

El resultado del escrutinio de los votos emitidos por los miembros titulares del tribunal, efectuado por la Escuela de Doctorado, a instancia de la Comisión de Doctorado de la UPC, otorga la MENCIÓN CUM LAUDE: SÍ ☐ NO ☐

(Nombre, apellidos y firma) Presidente de la Comisión Permanente de la Escuela de Doctorado	(Nombre, apellidos y firma) Secretario de la Comisión Permanente de la Escuela de Doctorado

Barcelona a ________ de ______________________ de ___________

ACKNOWLEDGEMENTS

I would like to express my special appreciation and thanks to my advisor Professor Dr. Jordi Marti Rabassa, you have been a tremendous mentor for me. I would like to thank you for encouraging my research and for allowing me to grow as a research scientist. Your advice on both research as well as on my career have been priceless. I would especially like to thank Mr. Alfredo Soldevilla, who is a general system manager at the Physics department at UPC for providing me technical support and help when collecting data for my Ph.D. thesis.

Special thanks to my family my lovely father and mother. Words cannot express how grateful I am to my mother and father ((may his soul rest in peace)), and my brother Kaher for his financial support also my sisters Noura and Maha. I would also like to thank the Canon Foundation (UK) and the Department of Physics of the Technical University of Catalonia for their financial support of this thesis.

Contents

1 An overview of this thesis

This is an introductory chapter, providing an overview of this document; therefore, the purpose of the thesis in addition to the structure of the work and the thesis will be briefly described in the following sections.

1.1 Overview

The work presented in this thesis focuses on the investigation of the proton transfer (PT) and its mechanism for the transferring, when the proton species is confined in pure liquid water. Our analysis is carried out by performing semi-classical molecular dynamics (MD) using the multistate empirical valence bond (MS-EVB) method, to reproduce intermolecular PT in liquid water and low-density amorphous ices, in bulk and in confined systems. The artificial neural network (ANN) approach along with statistical methods is then employed for modeling as well as analyzing the PT properties we are interested in [1-4].

PT in aqueous environments is a fundamental process in many biological and chemical processes with interesting technological applications, from energy production to aerosol industry and to atmospheric chemistry [5-7].Due to this wide range of PT applications, many researches, experimental [8,9] as well as theoretical, are devoted to a deep analysis. A complete understanding of the PT process in aqueous environments even though the PT process in water and aqueous media is still a challenging topic to be understood, and an exhaustive description of the phenomena occurring in presence of the excess positive charge among water molecules is still lacking. The mechanism responsible for the charge migration is not yet completely characterized on the microscopic scale and is object of controversy because PT details cannot be captured by experimental measurements and the modeling of water, at the basis of a theoretical approach, is difficult as well. Nevertheless, understanding the behavior of the excess charge in water is a first step towards more complicated applications, e.g., in biology, bioenergetics, enzyme functions and processes as complex as viral replication are connected to proton transport and storage or, in material science, proton migration through polymer electrolyte membranes is a critical components of the energy production process in hydrogen fuel cells [10 - 12].

The main purpose of this thesis is to analyze the structural properties and dynamics of solvation of an excess proton in different geometries in the nanoscale. In a first step, we will analyze the case of proton transfer in liquid water and low-density amorphous ices without confinement, to later move on to simulate the proton transfer in liquid water confined inside two graphene slabs. The three relevant structures playing a fundamental role are the so called Zundel dimer, the hydronium ion and the Eigen complex.

The work is organized as follows. Firstly, we have to identify the numerical method we want to use in order to produce our simulations in line with (1) the available computational models of PT in water which have a significant variation in their accuracy, efficiency, as well as complexity and obstacles, (2) the supplementary tools (e.g., ANN application) that has been designed to generate the outcome. Hence, nowadays, ANNs is common tools in computer science and mathematics [13]. They are mainly used in classification problems such as PT [14, 15]. In all applications, the general purpose of ANNs is to construct some input-output relations and to use these relations to analyze and classify data sets. On the other hand it will be interesting to evaluate our new developed ANN application; i.e., the use of the artificial neural networks AANs methodology in the classification of proton transfer events, fitting data as well as in the prediction of the outcome of a reaction without computing the individual MD trajectories, based on applying the feed-forward back propagation neural network methodology to EVB output data to work as a classifier to distinguish between these two transfer cases “occurred” and “not occurred” which could be a good tool for further investigations of PT in future studies of presenting structural and dynamical properties of the solvated proton in confined and unconfined environment. Secondly, on the basis of the results widely discussed in the literature, we can identify the most important properties, local structure of the excess proton, dynamics of proton transfer, proton diffusion and velocity and proton spectroscopy. We will analyze these properties to discuss our observations on the PT mechanism and to compare them with the results available from the literature.

1.2 Structure of the thesis

The thesis is organized as follows. **Chapter 2** sheds light on the literature review and definitions to determine the state of the art in relation to the research question for the most relevant components of this thesis. In the first instance, aqueous proton transfer PT definition and its peculiar features, structure of excess proton in water, and PT under confinement followed by the proposed analysis. Subsequently**, chapter 3** describes the computational methods used in this work in conjunction with a brief literature review of some available computer modeling of hydrated protons and supplementary applications for PT modeling including our ANN application, followed by a full description of our computational framework as follows: The adopted computational methods to study PT, including MD and MS - EVB tool that used throughout the thesis including the calculated quantities followed by an example for evaluating the use of ANN and the conclusions of this chapter.

Chapter 4 presents a complete analysis by comparing our results with those presented in the literature. Results and discussions of PT will be reported by thorough analysis of the structure and dynamics of an excess proton based on investigating the PT in liquid water, without confinement and confined inside graphene slabs. More explanation about the chapter contents of its key sections and related subsections are fully described in the introduction section of the chapter. Finally the main conclusions from this thesis will be summarized at the end of chapter 4 followed by recommendations for future studies.

2 Description of Proton transfer in water

The hydrogen ion H+ in aqueous solution is no more than a proton, a bare nucleus (aqueous proton). Although it carries only a single unit of positive charge, this charge is concentrated into a volume of space that is only about a hundred-millionth as large as the volume occupied by the smallest atom. The resulting extraordinarily high charge density of the proton strongly attracts it to any part of a nearby atom or molecule in which there is an excess of negative charge. In the case of water, this will be the lone pair (unshared) electrons of the oxygen atom; due to the electronic structure of water that is featured by two "lone pair"s electrons, which can interact with the hydrogen atoms in another water molecule forming O-H· · ·O hydrogen bonds, so that the tiny proton will be buried within the lone pair and will form a shared-electron (coordinate) bond with it, creating a hydronium ion, H_3O^+. This indicates the peculiar features of the PT process in water where lone proton H^+ does not exist in an isolated way. It is rather an “electron hole” with one missing electron from the excess proton and it is constantly moving. In a sense, H_2O is acting as a base here, and the product H_3O^+ is the conjugate acid of water. In a related context it is worth mentioning here that hydrogen bonding and PT are not only between water molecules or between oxygen atoms, the donor and acceptor could be any two atoms with large negativity, such as nitrogen, chlorine or fluorine atoms.

Herein, from the fundamental point of view, PT is the main reason for the neutral pH of water due to the process of water autoionization [16] and it plays a key role in energy conversion processes such as in photosynthesis and in cellular respiration [7]. Hydronium species can be found in most aqueous environments, even in interstellar media [17]. From a general point of view, the high mobility of hydrogen cations in water stimulated great interest in numerous disciplines of science such as chemistry, biology and physics that allows the PT phenomenon to work as an essential process that playing a key role in a wide variety of technological, medical, and chemical processes, such as in the energy production in fuel cell membranes [18,19], in fundamental molecular mechanisms occurring in viruses, such as the human immunodeficiency-1 protease (HIV-1PR) [12], in the activation of nicotine as it enters an aqueous environment [6], or as the main component in molecular reactions in aerosols [20] which are the base of atmospheric chemistry, to mention only a few. We refer to [10–12, 21, and 22] and references therein for a full description of the wide range of applications of PT in aqueous synthetic and biomolecular systems.

Due to this wide range of PT applications, many researches, experimental [8, 9] as well as theoretical, are devoted to a deep analysis in addition to a complete understanding of the PT process in aqueous environments even though the PT process in water and aqueous media is still a challenging topic to be understood also an exhaustive picture of the phenomena occurring in presence of the excess positive charge among water molecules is still lacking. The mechanism that is responsible for the charge migration is not yet completely characterized on the microscopic scale and is object of controversy because PT details cannot be captured by experimental measurements and the modeling of water, at the basis of a theoretical approach, is difficult as well. Nevertheless, understanding the behavior of the excess charge in water is a first step toward more complicated applications, e.g., in biology, bioenergetics, enzyme functions and processes as complex as viral replication are connected to proton transport and storage or, in material science, proton migration through polymer electrolyte membranes is a critical components of the energy production process in hydrogen fuel cells [23, 24].

Our purpose in this thesis is to model the transfer process of one excess proton and its mechanism for the transfer, when the proton species is confined in pure liquid water taking into account the influence of confining surfaces on microscopical structure and dynamics of the system. In the next section we qualitatively describe PT by means of the most recent results proposed in the literature and we introduce our approach to the study of proton transfer processes in confined pure liquid water besides the proposed analysis.

2.1 Structure of excess proton in water

Water behaves differently from most other chemical compounds with a number of unique and still mysterious chemical properties that make it an essential molecule to life on earth, thus, due to the capability of water molecules to form a highly dynamic hydrogen bond (HB) network. For example, it has a high freezing and boiling points; heat capacity, surface tension, in addition to smaller density in its solid phase (ice) than in liquid phase with maximum located at $4^\circ \mathrm{C}$. Furthermore, proton mobility in water at room temperature 300 K is at least 4.5 times faster than that of any other cations in water, which can be concerned as a consequence of proton transfer PT along the HB in water. Explanations for this anomalously high mobility of protons in liquid water began with Grotthuss's idea of “structural diffusion” more than two centuries ago. The Grotthuss mechanism for PT was first proposed in 1806 by T. Von Grotthuss [25] even though he did not know the chemical formula of water (he considers water as OH) in the following chemical reaction form:

$$\mathrm{H2O} \cdot \mathrm{H}+\cdots \mathrm{OH2}\,\_\,\mathrm{H2O}\cdots \mathrm{H}+\cdot\ \mathrm{OH2}. \qquad (2.1)$$

According to this mechanism the excess proton hops between adjacent water molecules in the water wire through successive covalent bond formation and breaking events. Grotthuss, suggested that the mechanism of PT at normal (ambient) conditions is due to a fast jump between neighboring water molecules and the HBs dynamics produces a structural diffusion of the complex formed around the excess charge. This model accounts for the excess positive charge migration without an effective migration of the proton itself, because not only one but numerous protons are concerned in the shuttling process. Herein, the charge migration is the outcome of successive proton jumps between the oxygen atoms in the water molecules; therefore the chemical bonds rearrangement is responsible for the PT. Moreover, the HB network reorganizes as well because the transfer takes place preferentially along HBs. Several variants to this description have been proposed. Although "Grotthuss mechanism" is physically insightful, people still try to understand the detailed molecular mechanism of this fundamental process. Subsequent explanations have refined this concept by invoking thermal hopping [26], proton tunneling [27] or solvation effects [28].

According to Conway and Bockris [29] a field induced (the excess charge electric field) molecular reorientation of a water molecule in the first solvation shell of the hydronium ion allows the proton to hop between the two oxygen atoms but the activation energy for the transfer to a water molecule, not hydrogen bonded to molecules in the second solvation shell, is too high; Bernal and Fowler [30] proposed a model for proton diffusion as a succession of transfers to freely rotating nearest neighbor water molecules that achieve the right orientation to accept the transferring proton, but even if the time of reorientation is similar to the PT rate, also in this case the energetic cost to break HBs is too high; the 'Moses mechanism', proposed by Agmon [27], describes the HBs cleavage in the second solvation shell of the hydronium ion as the precursor of the PT event. Actually, it has been known for a long time [28, 31] that small changes in the O–O distance can largely impact the proton shuttling along the respective HBs. This illustrates that PT process is generally very sensitive to its local micro-environment. After years of investigations and discussions the current widest accepted microscopic picture of the hydrated proton in water involves a series of structures intermediate between two limiting cations: the Zundel cation [32] and the Eigen cation [33, 34] (see figure 2.1).

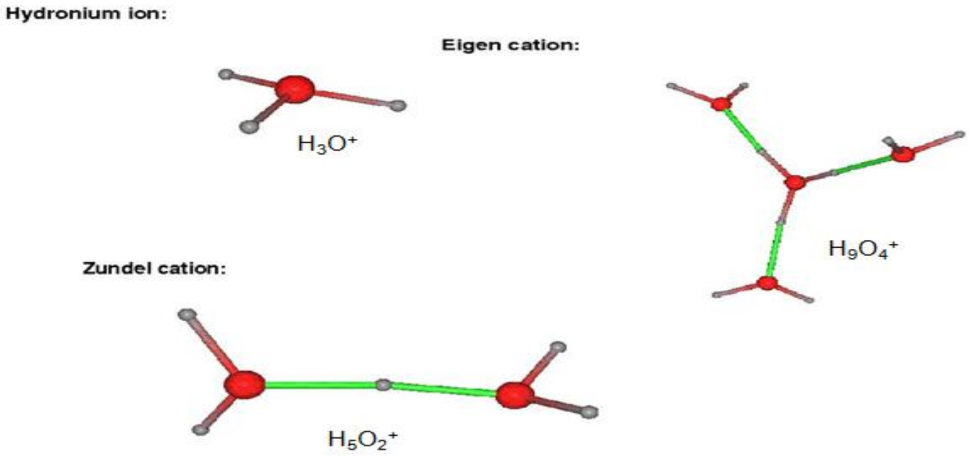

Figure 2.1: Structure of excess proton in water.

Modern research suggests that Grotthuss shuttling occurs by the Eigen-Zundel-Eigen (EZE) mechanism (see figure 2.2), whereby one distorted Eigen cation ('resting' state of the solvated proton) is converted into another with the Zundel cation as an intermediate**.** The ratio of the population of two species is not clear but the interconversion between the two configurations [35, 36], due to the dynamics of the local solvent, plays a key role in PT to occur.

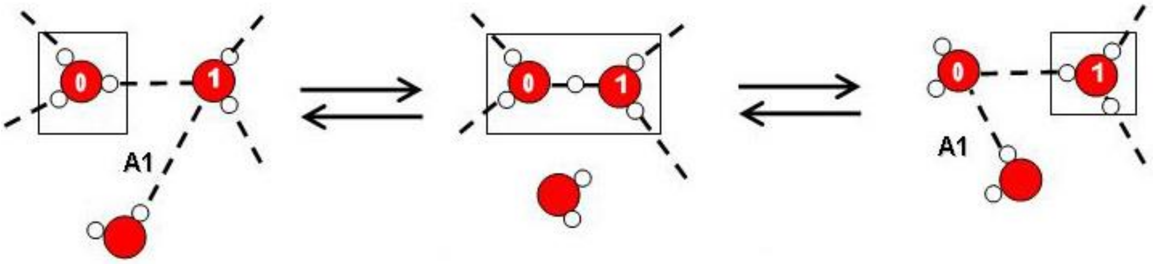

Figure 2.2: EZE mechanism [37].

The PT event is the consequence of the isomerization of the Zundel and Eigen structures $H_9O_4^+ \rightleftharpoons H_5O_2^+ + 2H_2O$ showing that the Zundel configuration is an important intermediary step for PT, even if the Eigen configuration is the lowest in energy. Herein, Eigen proposed the formation of an $H_9O_4^+$ complex. In which the central protonated water molecule, $H_3O_a^+$ is surrounded by three hydrogen-bonded water molecules H_2O, giving rise to the structure Eigen-like conformation**.**

However such an Eigen complex is not symmetric because the three water molecules in the first solvation shell are not equal as shown in the figure below. One water molecule H_2O_b has a shorter hydrogen bond to the O_a atom than the other two, forming a Zundel-like $H_5O_2{}^+$ conformation in a distorted Eigen structure. Zundel complex will be a symmetric configuration that is achieved when the excess proton is exactly shared by two water molecules. Herein, the identity of H_2O_b changes within the three water molecules in the first solvation shell without actual PT occurrence, which is named "special pair (SP) dance" by Agmon and Voth , the donating hydronium and the receiving water molecule and happens on an average of 40 fs (shown in figure 2.3).

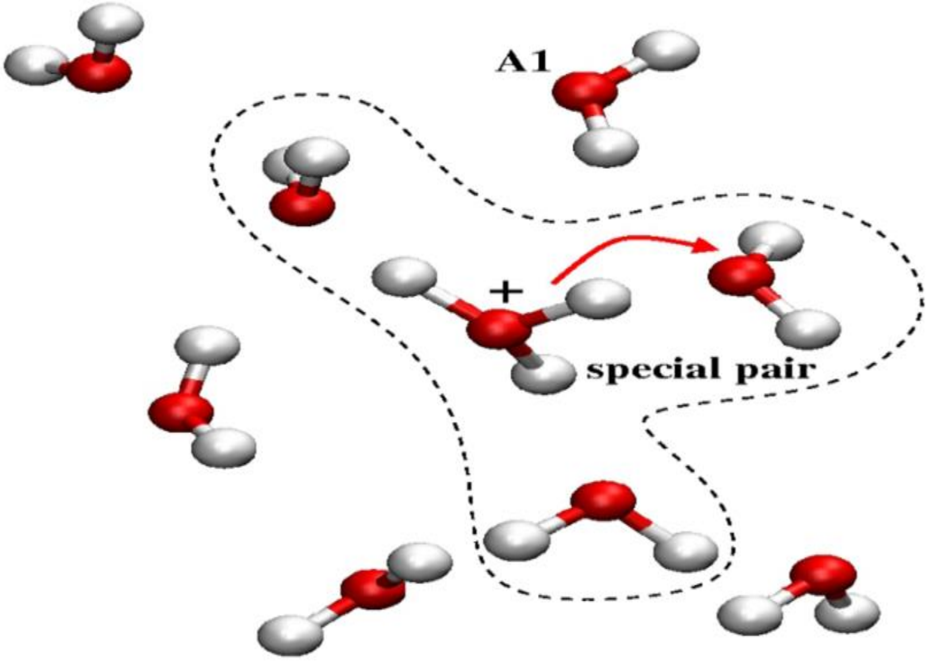

Figure 2.3: Special pair [38].

The outcome of such SP-dance process is the randomization of the proton hop direction so the proton mobility is diffusive as well as uncorrelated. The real PT happens when fluctuations in H-bond network cause a hydrogen bond between O_b and one water molecule in the second solvation shell to break and thus reduce the coordination number of H_2O_b from 4 to 3 because the local solvent fluctuations around the $H_9O_4^+$ complex produce a HB rearrangement in the second solvation shell with a reduction in the coordination of one water molecule in the first solvation shell of the central hydronium $H_3O_a^+$. The under-coordinated water molecule participates in only three HBs, instead of four as typically observed in pure water, acquiring a hydronium-like coordination structure (the hydronium ion is 3-fold coordinated in water).

The proton in the 'activated' HB becomes equally shared by two water molecules and, since the potential energy surface (PES) for the PT is symmetric, the proton can either be transferred to the H_2O acceptor or return to the donor molecule. The SP is transformed now to a Zundel complex $H_2O_a - H^+ - O_bH_2$, in which the proton may rattle many times between O_a and O_b, and finally a new Eigen complex centered at $H_3O_b^+$ may form.

This qualitative description illustrates PT as an Eigen-to-Zundel-to-Eigen (EZE) process [37], in which the Zundel configuration represents the transition state (because it is less stable), but some observations depict a different mechanism, the Zundel-to-Zundel **(**ZZ) process that is the interchange between two adjacent Zundel configuration during the PT event[37]. These observations are proposed on the basis of numerical simulations that are fundamental in the study of PT because proton is an elusive particle and it is not accessible by experiments. In the special-pair (SP) dance, the length of these hydrogen bonds fluctuates rapidly over time, with any one of the three bonds being shorter than the remaining two. This dance is a preparatory stage of proton transfer, during which the central hydronium ion searches for a partner.

The successful partner accepts only one hydrogen bond, whereas most water molecules accept two. Once a successful partner is identified, the proton transfer event occurs between the special pair SP**.** The partner transfers significant electronic charge to the hydronium cation along the strong SP hydrogen bond. The SP dance demonstrates the sensitive coupling between the excess proton along with its surrounding hydrogen bond network. Proton transfer, therefore, occurs by means of a cooperative, diffusive process rather than by simple hopping. The rate-limiting step is the hydrogen bond cleavage between the first and second solvation shell. During computer simulations continuous interconversions between the two structures are usually seen, producing a hybrid $(H_9O_4)^+/(H_5O_2)^+$ complex [39, 40]. The timescale for such interconversions is that of picoseconds, involving changes of oxygen-oxygen $(O-O)$ distances and modifications of the hydrogen connectivity pattern between the hybrid complex at its coordination shells. During the whole process, neither a large delocalization of proton [27] nor proton tunneling [26] is likely to happen.

2.2 Proton transfer under confinement

Confinement in nanometer-sized environments can modify the behavior of liquid phases substantially. Evidences of this are the changes in most of the thermodynamic properties of these phases, reflected in shifts of equilibrium constants and corresponding changes in the phase diagrams. Perhaps one of the clearest examples of this is the phenomenon known as 'drying transition'.

This phenomenon is the total elimination of the aqueous phase plates located between two macroscopic hydrophobic plates when the distance between them is the order of a few nanometers. This phenomenon is the result of a subtle balance between the magnitude of the intermolecular water-water and water-wall forces and the competition between surface properties and properties of "bulk" water [41]. The analysis of liquid mixtures is equally interesting: the solvation in porous glasses like "Vycor" significantly affects the phase equilibrium in mixtures water/luditine and the critical behavior of mixtures formed by n-hexane/perfluorooctane, to cite two examples [42].

In addition to the structural changes, major changes are also observed in the dynamic properties: in these cases, the changes involve significant slowdown of all dynamic modes, translational as well as rotational. These changes represent critical elements for the correct interpretation of many processes with direct practical applications such as nanoscale flow control through nanotubes [43] and membranes [44] the design of devices for the storage of gases [45] or processes of controlled release of drugs [46]. In a still broader context, the effects of confinement on water phases is relevant for understanding the behaviour of solvation layers to modulate the function of self-assembled structures and complex molecules such as proteins [47], DNA [48], or lipid bilayers. To cite some relevant examples [49] the analysis of protons under confinement has been performed from different perspectives. The case of aqueous reverse micelles is perhaps one of the clearest examples. There are at present a large number of publications that have analyzed its role as local pH control agents, such as in acid-base equilibrium and in catalytic processes. On the other hand, the research group responsible for this thesis has analyzed the case of protons dissolved in non-ionic micelles [50]. When confined in constrained geometries, the microscopical properties of the proton also suffer drastic changes. So, studies of PT near alumina surfaces [51] and in Nafion fuel cell membranes [52] reported changes in frequencies of vibrational motions and orientational relaxation times induced by the presence of the surface.

Although many unanswered questions remain regarding the proton transfer as well as transport mechanisms in water, the findings of a recent experimental study based on ultrafast two dimensional infrared spectroscopy which was conducted for investigating the excess proton in liquid water (in aqueous hydrochloric acid solutions) [53], suggests a key role for the Zundel complex in aqueous proton transfer that place important constraints on the role of the Zundel complex in this process as were observed by determining a lower limit on the lifetime of this complex of 480 fs when exciting O–H stretching vibrations and detecting the spectral response throughout the mid-IR region. The interaction between the stretching as well as bending vibrations characteristic of the flanking waters of the Zundel complex, $[H(H_2O)_2]^+$, at 3200 and 1760 cm^{-1}, respectively were observed. Drawing conclusions regarding to Eigen species stability or role in aqueous proton transfer was not provided in the study because they did not observe the Eigen species in the described experiments. However, notations were addressed in which no sign of vibrational excitation transfer was observed from the Zundel stretch into the region characteristic of Eigen configurations (2000 to 2800 cm^{-1}). A relatively long-lived Zundel complex represents an important part of the proton transfer mechanism; this configuration is not merely a fleeting transition state traversed during an Eigen-to-Eigen proton transfer. In addition to Zundel-to-Zundel transport, exchange processes involving Zundel-to-Eigen transport are still consistent with their data.

2.3 Model of hydrophobic walls: flat graphene

Confined water is generally liquid water held within nanometer-sized vessels. It is found widespread in nature in granular as well as porous material and around and within cells, macromolecules, supramolecular structures along with gels. It has recently been reviewed that its properties are difficult to predict and may be very different from those of bulk water [54]. This is particularly true when the confinement is on the nanoscale. Recently, it was experimentally found that confined water exists as a quasi two-dimensional layer with different properties than those of bulk water. Moreover, much theoretical and experimental work has studied the effects of nanoscale confinement on PT in water based on the constrained geometries hydrophilic (silica) versus and hydrophobic (graphene). Hence the term 'hydrophobic' is derived from *hydro-* (water) and *phobos* (fear) .In terms of chemistry, hydrophobicity is the physical property of a molecule (known as a hydrophobe) that is seemingly repelled from a mass of water. In contrast to hydrophilic materials, such hydrophobic material has lacking affinity for water; tending to repel and not to absorb water; tending not to dissolve in or mix with or be wetted by water. However, smaller hydrophobic materials can be dissolved to a small extent in water as water molecules can arrange around them without breaking hydrogen bonds or losing much energy and the hydrophobic molecule can interact with these water molecules with multiple van der Waals interactions, due to the small size of water molecules in addition to the flexibility in their spatial arrangement [55, 56].

In this thesis, we considered two graphene slabs as hydrophobic containers of water to analyze the effects of water confinement, on proton solvation structure and on its dynamical properties. The water-graphene interaction has not been included here, so that this section will generally shed light on the graphene definition, atomic structure and properties as an introduction for our future studies. The graphene interaction with water will be considered when studying the PT under confinement (see chapter 4 section 4.5).

2.3.1 Graphene properties

Graphene the two-dimensional crystalline allotrope of carbon and is usually a hydrophobic material which was used in a recent experiment to confine water into monolayer, bilayer and three layered structures. Allotropy is the property of chemical elements to exist in two or more forms. Graphene has many extraordinary properties, based on its ability to conduct heat and electricity better than anything else, even though it is currently in its infant stages and is undergoing many applications and studies mean that it can be integrated into a huge number of applications such as photovoltaic cells; composite materials; biological engineering; optical electronics, lightweight aircraft/vehicles OLED Technologies and Energy Storage [57].

2.3.1.1 Atomic structure

Graphene is a flat monolayer of carbon atoms tightly packed into a two-dimensional (2D) honeycomb lattice, and is a basic building block for graphitic materials of all other dimensionalities. Also graphene could be defined as an isolated atomic plane of graphite (singular layer of graphite) as shown in figure (2.4). The atomic structure of isolated, single-layer graphene was studied by transmission electron microscopy (TEM) on sheets of graphene suspended between bars of a metallic grid. Electron diffraction patterns showed the expected hexagonal lattice of graphene. Suspended graphene also showed "rippling" of the flat sheet, with amplitude of about one nanometer. These ripples may be intrinsic to graphene as a result of the instability of two-dimensional crystals or may be extrinsic, originating from the ubiquitous dirt seen in all TEM images of graphene. Atomic resolution real-space images of isolated, single-layer graphene on SiO_2 substrates were obtained by scanning tunneling microscopy. Graphene processed using lithographic techniques is covered by photoresist residue, which must be cleaned to obtain atomic-resolution images.

Graphene sheets in solid form (density > 1 g/cm^3) regularly show evidence in diffraction for graphite's 0.34 nm (002) layering. This is true even of some single-walled carbon nanostructures. Transmission electron microscope studies show faceting at defects in flat graphene sheets.

Furthermore, graphene physically acts as a 2D material (crystal of carbon) with many potential applications such as flexible electronics, efficient transistors and novel sensors. Due to this 2D structure, it is the only form of carbon (or solid material) in which every atom is available for chemical reaction from two sides. The atoms at the edges of a graphene sheet have special chemical reactivity. Moreover, it has the highest ratio of edge atoms of any allotrope. Defects within a sheet increase its chemical reactivity. It is commonly modified with oxygen- and nitrogen-containing functional groups and analyzed by infrared spectroscopy and X-ray photoelectron spectroscopy. However, determination with oxygen [58] and nitrogen [59] functional groups requires the structures to be well controlled.

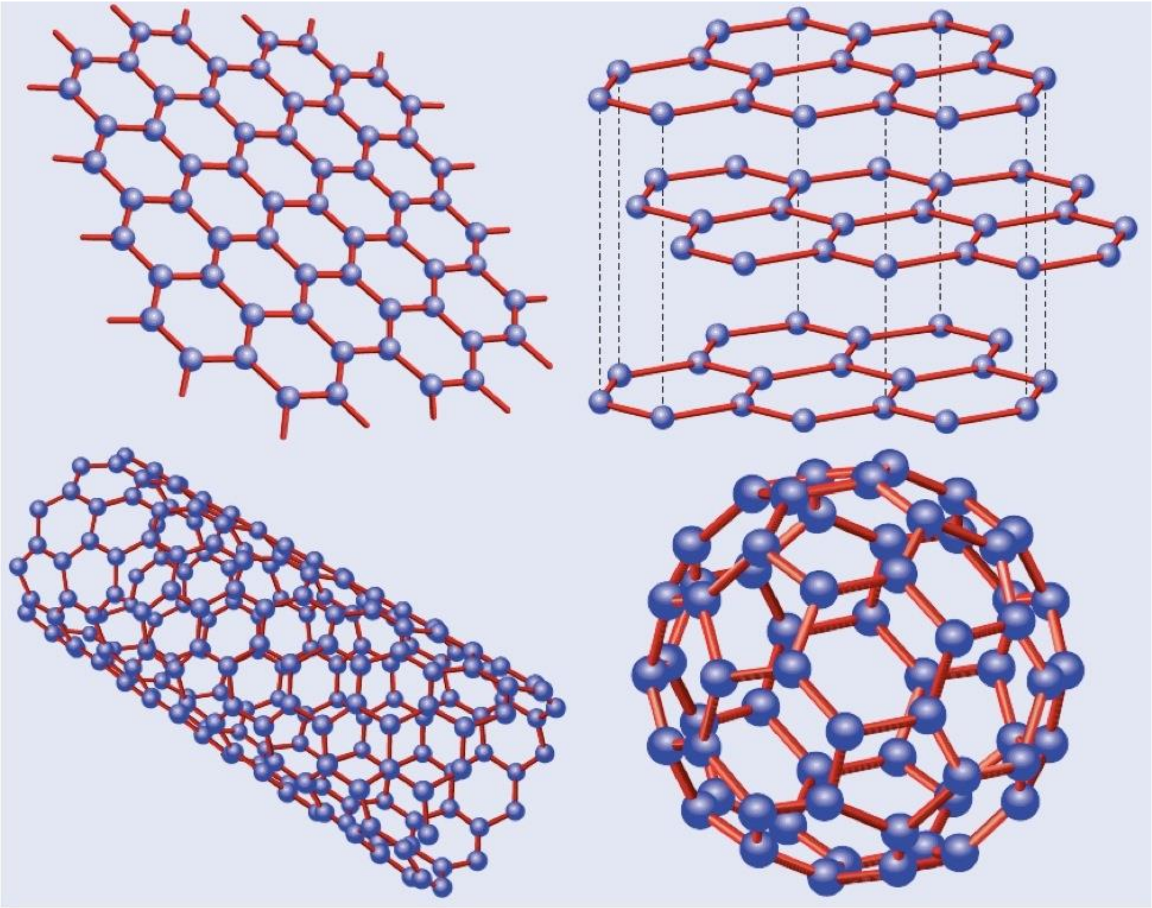

Figure 2.4: Graphene versus other allotropes. Graphite (top right), Graphene (top left), carbon nanotube (bottom left), fullerene (bottom right).

2.3.1.2 Electrical properties

Graphene differs from most conventional three-dimensional materials. Intrinsic graphene is a semi-metal or zero-gap semiconductor. Understanding the electronic structure of graphene is the starting point for finding the band structure of graphite. Scientists have theorized about graphene for decades. Graphene theory was first explored by P.R. Wallace (1947) [60] and it was originally observed in electron microscopes in 1962, but not studied further [61]. That the equation describing the E-k (energy-momentum) relation is

$$E = \hbar v_f \sqrt{k_x^2 + k_y^2}, \tag{2.2}$$

where the Fermi velocity is $v_F \sim 10^6$m/s. This relation is linear for low energies near the six corners of the two-dimensional hexagonal Brillouin zone, leading to zero effective for electrons and holes. Due to this linear (or “conical") dispersion relation at low energies, electrons and holes near these six points, two of which are inequivalent, behave like relativistic particles described by the Dirac equation for spin 1/2 particles. Hence, the electrons and holes are called Dirac fermions, and the six corners of the Brillouin zone are called the Dirac points.

The material was later rediscovered, isolated and characterized in 2004 by Andre Geim and Konstantin Novoselov. This work resulted in the two winning the Nobel Prize in Physics in 2010 "for groundbreaking experiments regarding the two-dimensional material grapheme [62]. In 2013, physicists from Stanford University reported that single-layer graphene is a hundred times more chemically reactive than thicker sheets.

This leads to many properties that are electrically beneficial, such as high electron mobility and lowered power usage. Also electrons in grapheme have an ability to travel short distances without scattering which makes it one of the best materials for electrical applications. Some of its electrical properties can be summarized as follows [63]:

- The Fermi level can be changed by doping to create a material that is better at conducting electricity
- Experimental graphene's electron mobility is 15,000 cm^2/(V*s) and theoretically potential limits of 200,000 cm^2/(V*s)
- Graphene electrons are like photons in mobility due to lack of effective electron and hole mass
- These charge carriers are able to travel sub-micrometer distances without scattering

2.3.1.3 Mechanical and optical properties

Graphene's mechanical and optical properties (e.g., absorbs 2.3% white light, optical electronics absorb <10% white light; highly conductive; strong and flexible) allow its use to go beyond electrical applications. The mechanical strengths of graphene can be summarized as follows [64]:

- Bond length is .142 nm long = very strong bond

- Strongest material ever discovered, graphene is about 100 times stronger than the strongest steel with a hypothetical thickness of 3.35Å which is equal to the thickness of the graphene sheet ultimate tensile strength of 130 gigapascals compared to 400 megapascals for structural steel
- Very light, at 0.77 milligrams per square meter (paper is 1000 times heavier).
- Single sheet of graphene can cover a whole football field while weighing under 1 gram
- Also, graphene is very flexible, yet brittle (preventing structural use)

2.3.1.4 Thermal properties

The near-room temperature thermal conductivity of graphene was recently measured to be between (4.84±0.44) $\times 10^3$ to (5.30±0.48) $\times 10^3 Wm^{-1}K^{-1}$. These measurements, made by a non-contact optical technique, are in excess of those measured for carbon nanotubes or diamond. By using the Wiedemann-Franz law, it can be shown that the thermal conduction is phonon-dominated [65]. However, for a gated graphene strip, an applied gate bias causing a Fermi energy shift much larger than k_BT can cause the electronic contribution to increase and dominate over the phonon contribution at low temperatures. Furthermore, graphene burns at very low temperature (e.g., 350 °C (620 K)).

After reviewing the fascinating properties of graphene, we should be convinced of its interest of being considered as our hydrophobic water-proton container.

2.4 Proposed analysis

As explained in the above section a modern image of the lone proton has arisen after recent findings from both experimental and theoretical studies. From this image, there is a general consensus that for bulk water proton dynamics is directly associated with dynamics of the HB network of water. Nevertheless, aqueous proton transport processes occurring in complex, strongly confined environments, are not yet fully understood. In many cases proton conduction takes place in confined volumes [23, 24]. The understanding of proton conduction in confined geometries is thus essential to comprehend and ultimately control a wide variety of biological and technological systems of fundamental and practical interest. Despite the large scientific and industrial relevance of PT, the mechanisms of proton conduction are still a largely unexplored area of research. The main reason for this missed knowledge is essentially the limited number of experimental techniques sufficiently sensitive to probe proton conductivity in confined spaces, and also the lack of accurate predictions coming from theory and simulation. Up to date, it has been observed that when confined in restricted geometries, microscopical properties of the proton also suffer drastic changes from those at bulk states. At the surroundings of the lone proton we should expect significant differences with local coordination shells of pure liquids, ices and vapors. However, since the calculation of the phase diagram of the water model employed by us is out of the scope of this thesis, we will consider a series of equally distributed thermodynamical states from low density amorphous (LDA) ices to dense liquids at variable densities and temperatures and explore the influence of such factors on the structural and dynamical characteristics of PT.

Herein, analysis of protons under confinement has been performed from different perspectives. In this thesis, we will concentrate ourselves in the study of the topological characteristics of confinement in three- dimensional (3D) towards 2D geometries. Protons in condensed phases confined in 3D environments and also with dimensionality close to 1, such as carbon nanotubes [46] have been previously analyzed, and qualitative changes in their equilibrium properties and transport, with reduced dimensionality, were found. Several previous studies have analyzed the behavior of quasi two dimensional aqueous phases, confined between graphene sheets. However, to our best knowledge, no previous studies have considered the presence of aqueous protons inside narrow grapheme slabs in a wide variety of thermodynamic conditions. We believe therefore that it is a relevant topic, which will complete the previous analysis. Furthermore, we expect that the problem will have a number of features that can hardly be extrapolated from the knowledge in one and 3D. Hence, our interest to address the direct study of this type of problem should not be considered as an incremental aspect of previous studies, but as a project with its own scale. A prototype system to study is that of the aqueous proton confined inside a rectangular slab, changing gradually from a slab containing a large bulk part, up to a system with compressed water forming one or two layers, namely a quasi-two-dimensional water network inside a graphene slab.

A very recent contribution that is worth mentioning here, in a similar fashion to the present work produced by Bankura and Chandra [66] who employed ab initio and quantum-classical simulations to model proton transfer in two-dimensional water layers, with fixing the interpolate distance to 1.2 nm to indicate that when water is strongly confined in two-dimensional environments, the lone proton is likely to be solvated as the Eigen cation and that PT rates are significantly lower than in the quasi-one-dimensional case. In the present work, we considered variable interplate distances between 3.1 and 0.7 nm and variable temperatures (100- 600 k). At the environment of an excess proton, we should expect further significant differences with local densities of pure liquids and solids due to the presence of the lone proton. Therefore, we should expect significant changes in the proton microscopical structure formed (in pure water at ambient conditions) by a series of structures intermediate between two limiting cations: the Zundel dimer $(H_5O_2)^+$ and a hydronium species $(H_3O)^+$ coordinated by water, i.e., the Eigen cation $(H_9O_4)^+$. We also expect significant changes of the time scale of PT due to the presence of confining surfaces and also compared to the case of water inside carbon nanotubes.

Accordingly, we will analyze the structural properties and dynamics of solvation of an excess proton in different geometries in the nanoscale. In a first step, we will analyze the case of proton transfer in liquid water and low-density amorphous ices without confinement, to later move on to simulate the proton transfer in liquid water confined inside graphene slabs.

Our analysis is carried out by performing MD simulation and MS-EVB methods supported with an artificial neural network (ANN) pattern recognition and data mining software applications. Herein we have adopted the evaluation of the use of AANs methodology in the classification of PT events and chart patterns, thus to facilitate the modeling process by using these simulation methods, overcoming their limitations and allowing statistical filtering of the data along with the predicting of the PT dynamics in aqueous environments. Therefore besides presenting our evaluation of the use of our

ANN tool in the following chapter, let us describe some relevant aspects of PT in restricted aqueous geometries that this thesis will attempt to understand.

1) It will be very important to know how, under restricted geometry of the aqueous phase by the presence of hydrophobic plates kept at fixed distance, the balance between the common Eigen and Zundel species in water should change from the typical situation at bulk unconfined solutions, where an equilibrated mixture of the two species exists. In addition, force fields between proton, water and constraining walls will need to be set up.
2) Analyzing the characteristic time scales (for proton transfer rates, water and proton diffusion, residence times in coordination shells) under confinement. Evaluating what changes are introduced based on previous simulations in pure water to analyze the dynamics of hydrogen bonds.
3) Predicting and interpreting the changes that will appear in the location of the characteristic frequencies of new modes and the overall shape of the spectrum, introduced by the confinement.

3 Computational Methods

From the perspective of atomic level PT is difficult to be observed experimentally. Instead, the majority of knowledge about the PT mechanistic details is being obtained from computer simulations. A number of methods have been developed for simulating PT with a significant variation in their accuracy, efficiency, as well as complexity. In this work, we developed and tested a new computational framework to simulate and describe PT that meets these criteria in terms of technical analysis and software developments. Our analysis is carried out by performing semi-classical molecular dynamics using the multistate empirical valence bond method, to reproduce intermolecular PT in liquid water and low-density amorphous ices (confined and unconfined environments).

The systems considered in the present work consisted in two parts: (1) a quantum particle (excess proton) and (2) a classical bath (liquid water, steam or amorphous ice) formed by 125 water molecules. We are going to illustrate in this chapter the theoretical background at the basis of the techniques we used to study the PT process in water. Here we should distinguish between the effects of the quantum nature of the proton on its dynamics.

In this study we employed a MS-EVB approach to model the quantum nature of proton, observed through its delocalization, together with MD techniques which allowed us to monitor the trajectory of all particles in time. The artificial neural network approach along with statistical methods is then employed for modeling as well as analyzing the PT properties we are interested in. On the one hand, this combined methodology has been widely used to study chemical reactivity in solution [67-71]. In particular this chapter will focus on the descriptions of our new developed computational framework based on ANN application, including its validity and the network ability to learn PT chart patterns corresponding to the properties of the aqueous environments. This chapter will also present the evaluation of the need for such pattern recognition software in the PT investigation as well as analysis how the learning approach in error back propagation (multilayer perceptron MLP algorithms) could be satisfactorily employed in studying the aqueous proton transfer processes. In the meantime we will refer to several references for describing the theoretical background of the ANN method as it is a well known method this work will not focus on its topology or theoretical structure details.

For the sake of concision, the following sections will restrict on describing our computational framework in line with reviewing some available computer modeling of hydrated proton with a focus on the MS-EVB and MD, besides identifying the most important computational terms related to ANN, to mention some: (chart pattern recognition and ANN, automated chart pattern, physical mechanisms of our ANN application, the computing process via it, and its data resource).The validity of this method in detecting PT chart patterns via a case study will be shown at the end of this chapter with describing the statistical methods of the calculated quantities as well.

3.1 Computer modelling of hydrated protons

Numerical simulations are not yet resolutive for a full understanding of the PT mechanism. A model for proton solvation and PT must be able to describe the continuously changing network of hydrogen-bonded water molecules surrounding a hydrated proton. Moreover, the force fields, used in the simulations, have to be flexible [72] because they must allow for the bond-breaking and bond-forming at the basis of the chemical reaction in equation (2.1) and for the atoms identity to change. Traditional force fields, however, are not reactive; they lack the ability to describe the formation and cleavage of chemical bonds. Then, they have to conveniently reproduce the complex nature of the HB network in water, that is a very difficult solvent to model [e.g., several models exist to reproduce bulk water properties] and have to account for the solvent effect on the potential energy surface PES for PT.

Furthermore, quantum effects are supposed to be important, even at room temperature, due to the small mass of the proton, whose thermal de Broglie wavelength is around $\approx 1 \mathrm{A}^{\circ}$ thus of the same order of magnitude of proton displacements. It is important to note that quantum effects may be described in a variety of ways, whose choice will depend strongly of the characteristics of the system under study. So for fully quantum systems such as liquid helium or hydrogen, the choice of methods such as path integral Monte Carlo or *ab initio* Car-Parrinello molecular dynamics is in order. When the system under study consists of a quantum particle in a sea of classical molecules, other semiclassical methods such as empirical valence bond EVB are also very appropriate. A full classical description in a MD fashion is not possible to simulate the Grotthuss mechanism because classical force fields, used in standard MD, do not allow for bond-breaking as well as bond-forming, processes which are at the basis of a chemical reaction. The inconvenient of using first principles techniques is the computational cost that allows for simulations of only about a hundred of atoms for tens of picoseconds.

A good compromise is represented by the empirical valence bond model an approach in which the interatomic interactions are modeled using molecular mechanics force fields, that was firstly introduced in the work of Warshel and Weiss [73]. The EVB method incorporates an ab initio derived PES for a small set of coordinates representing the reaction in an empirical potential model, yielding an accurate as well as efficient description of the process typically in the form of reactant-like along with product-like states, as shown here. In its first form [74], the method was used for simulating the Zundel cluster $H_5O_2^+$ dynamics in bulk water, by means of a two states EVB model. The generalization to a multistate model was then proposed by Vuilleumier and Borgis [75] in order to account for multiple pathways that are possible, from the same starting structure, in the PT reaction due to the combined effect of molecular diffusion and HBs rearrangement. The use of the MS-EVB model in this thesis is described in section 3.2.2.

On the other hand, the vibrational transitions associated with intermolecular proton transfer or “low-barrier” hydrogen bonds are very sensitive to the chemical environment, and the infrared signatures exhibit a very diffuse character [76, 77]. These make computational simulations, valuable for assigning spectra and obtaining energetices and dynamics of the studied system especially when combining “molecular dynamics (MD) simulations” with EVB calculations. Accordingly, spectroscopic methods such as Fourier-transform infrared (FTIR) allowed Devlin and coworkers [78,79] to monitor the hydrogendeuterium exchange in water an hydrogen chloride adsorbed in ice surfaces and to obtain activation energies of Bjerrum defect formation. Ohmine and coworkers [80, 81] have reported results from *ab initio* calculations and observed that PT in cubic ice Ic is still fast, but significantly less than in liquid water. Experiments on amorphous ice films by reactive ion scattering and low-energy sputtering have revealed that PT occurs up to temperatures of the order of 100 K [82,83]. A recent study by means of reactive ion scattering and infrared spectroscopy [84] indicates the existence of efficient proton-relay channels for hydronium on amorphous ice surfaces.

In recent years, new advanced PT pattern recognition and data mining computer applications have been developed based on ANN techniques to support the theoretical investigations of PT process and chemical reactions in aqueous environments (e.g. MD , Monte Carlo simulations, *ab initio*…etc) and to overcome the limitations of the outcome of these PT simulations (e.g. quality of the underlying potential-energy surface (PES), accuracy of the energies and atomic forces, crowed chart pattern and large set of the simulated output data, non linearity of input data, time and length scales of molecular simulations). In this regard, it is worth mentioning some related applications here, such as those innovative classes of interatomic potentials simulations based on ANN which has emerged as supplementary applications “tools” for molecular modeling in order to enhance the simulation accuracy, efficiency, and to reduce complexity when dealing with their input and output data (e.g., plotting a large set of the output data of such PT simulations will give noisy and crowd charts and finding appreciated PT patterns would be impossible) [1, 14, 85].

The next section will briefly describe our ANN techniques in line with reviewing the main concepts of ANN methods , related literature of using ANN applications in PT simulation in water, definition of related terms (e.g., chart, automated pattern recognition, data mining…etc) to finally introduce a brief description of the computational framework of this study including MS-EVB and MD plus its add- on ANN tool, how it works, the resource of data, its validity, and it ability in predicting beside explaining the calculated quantities followed by the conclusion. Our results in turn proved to be fully compatible with previous PT studies and it has been recently published [1].

3.1.1 Supplementary computer applications for PT modelling: Automated pattern recognition

In general, charts can be used to formulate physical information including quantum information that is contained in a physical system and can even be the only tool a researcher utilizes. Even though creating charts and finding patterns on charts were difficult before the advent of computers and data feeds. With the advancement of technology and the increased popularity of data mining technical analysis, the use of charts has greatly increased nowadays, making them one of, if not the most important, tools used by scientific analysts to study physical phenomenon, such as the proton transfer PT phenomena in aqueous environments. Herein using automated pattern recognition and data mining tools to support theoretical investigations of PT in aqueous environments via the above mentioned high performance computational PT simulations are currently of great interest to understand this phenomenon, since PT could be viewed as a pattern classification problems in terms of a set of input features that allow the classification of the proton motion into two categories: transfer ‘occurred’ and transfer ‘not occurred’.

Hence, chart patterns refer to the graphical representations of the output data of specific software “PT model”, which is being used in the required simulation (e.g., MS-EVB, etc). Achieving the best results of using charts requires correctly identifying chart patterns on the required chart, for distinguishing one thing from another; so researcher must be able to identify chart patterns properly by defining methods of recognition using new technological pattern recognition tools. An important point before we proceed, patterns itself could be defined as regularities in the output data when using computer simulation or an experimental results; however, the problem of searching for patterns in a large set of data is an essential problem of science and has a long and successful history [86-89]. Therefore, pattern recognition could be recognized as a key part of scientific investigation. Regularities in atomic spectra have been discovered in the early twentieth century and later on played a key role in the development of the quantum theory of the atom and so forth. The automatic discovery of regularities in data in the field of pattern recognition had become relevant through the use of computer algorithms and the analysis of these regularities by means of classifying the data into different categories; therefore, this problem had been considered and studied in many situations (e.g., medicine, finance, robotics, physical phenomena, PT). When automatic identification of patterns are required, the aim of pattern recognition is the same at all of these situations and would focus on classifying data patterns with respected to either the extracted statistical information from the patterns or on using some a priori knowledge for providing a reasonable answer for all possible inputs and to do "fuzzy" matching of inputs. Most commonly the patterns to be classified depended on using groups of observations and measurements, which served as defining points in a relevant multidimensional space [89]. Nevertheless the problem might be nonlinear (e.g.PT) in such a case we would need different classifying methods.

For example, imagine a two-dimensional data set of the heights and weights of some different animals if there were two types of animal in that data collection as presented in figure. (3.1.a) The green circles showed examples of animals of class 1 (snarks) and the yellow diamonds showed examples of animals of class 2 (boojums). Given a new data point, which type of animal is it? In this case someone would look at some methods that draw a straight between classes – linear classifiers and then the decision boundary (dashed line) would present the set of points at which both classes would be equally likely.

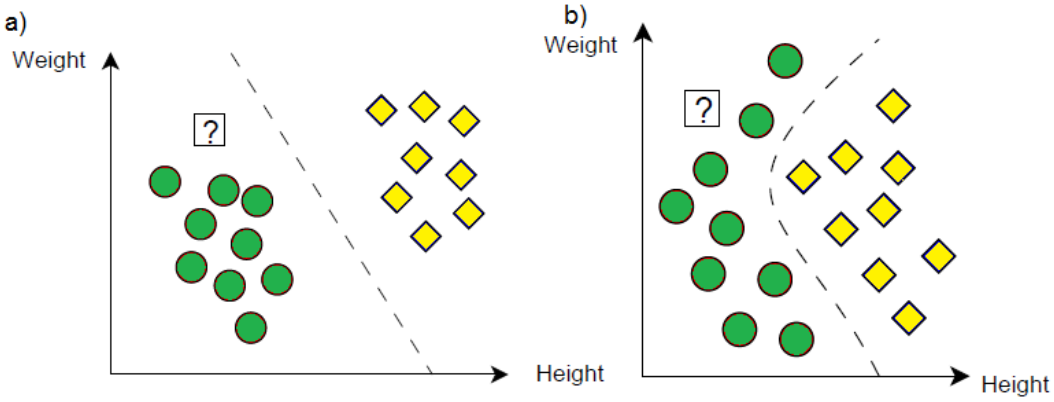

Figure.3.1: Different patterns in data analysis

Hence, data mining is the computational process of discovering patterns in large data sets involving methods at the intersection of artificial intelligence ANN, machine learning, statistics, and database systems [88, 89]. The overall goal of the data mining process is to extract information from a data set and transform it into an understandable structure for further use. Nowadays many data mining algorithms exist [90, 91]. While these algorithms are able to extract useful information in large amounts of data, they will be affected by data complexity. Among others ANNs has become the most common tool in computer science and mathematics with its good advantage of parallel computing, distributed information storage, fault tolerance capability, with adaptive learning ability, fitting capability, classification and predicting ability etc, [92-95]. They are mainly used in classification problems such as PT. This technique could be used for several purposes after generating the required data using a powerful theoretical simulation (e.g., data resampling (statics), data fitting capability, data analysis, data mining, pattern recognition, big data problems data corruption in output files, automatic estimation of data, predicting results, etc).

In this, ANNs mimic human brain when coping with incomplete and confusing information sets. Another important issue with implementing the ANN method here is that it is based on supervised learning which requires a data set, in many situations of considerable size, for which the target output is known taking into account the correlation between the inputs [88]. Output refers to an experimental data or output of computer simulation that work as input of ANN network to start analyzing and classification of data this means that ANN allows learning by example. Therefore, to find an automated method for classifying data, we need a way for plotting data; so that the classes would be separated, then the need of a visualization tool would be important to see the characteristics of the data after finding ways of incorporating background a priori knowledge about the problem into a specific method. For example the implementation of the approach of learning in a multilayer perceptrons network which is the most suitable type of the artificial neural networks [88] types. We refer to the following references [96, 97] for more information about the ANN structure and functionality, theory and applications.

Although many ANN applications are possible but there is a little work that can be found in the literature since it has been developed by McCulloch and Pitts in 1943. Who developed ANN to investigate the neural signal processing in the brain [98]. The first application from which a physics results was extracted with using ANN was for the decay of the Z boson [99], the results used further for determining the decay probability of Z into the corresponding states. A good review of these applications until 1999 was published [92]. Other important physics results were obtained with such ANN applications in high-energy physics [93, 94]. In the meantime there are so many several data analysis applications that used standard method instead of using ANNs for automatic estimation of data and chart patterns in physics and some other related fields such as [100-101]. Even though, in all applications, ANNs gave better results than standard methods, mainly due to the highly non-linear character of the method [99]. In this regard, there are many new opportunities for using ANNs in physics nowadays, mapping sets of physical problems to analogous applications in other areas of science as well as engineering, such as medical diagnosis disease applications [101,102], where ANNs showed significant results in dealing with data represented in symptoms and images i.e. chart patterns. Therefore, we can say that ANNs are currently favored by the majority of the research scholars for supporting the theoretical simulations of PT including the current study.

3.1.2 Artificial Neural Networks application in PT simulation

In all ANN applications, the general purpose of ANNs is to construct some input-output relations and to use these relations to analyze and classify data sets including chart patterns. In this regard the ANN modeling technique has many favorable features such as efficiency, generalization as well as simplicity, which make it an attractive choice for modeling of complex systems, such as PT, that allows the fitting and the predicting of the structural and dynamical properties of the solvated proton in confined and unconfined environment. The most promising application of the method published to date is to water clusters [14, 15,103].

Our PT investigations were based on the MS EVB simulation which had been proved to be a very successful method for the simulation of the PT in condensed media and that could be used for a variety of solvents, from pure water to mixtures in order to model PT processes for water complexes. However, using MD-EVB simulations is mainly based on analyzing the chart patterns of its output data, even though there are some obstacles that decreased its efficiency (e.g., number of water molecules, size of length measurements in three dimensions simulation of box volume, etc), also it does not support plotting charts and it has a huge set of tabulated output data that needs to be extracted and exported manually to any external plotting program (e.g., MS-Excel). This consumed more time and required greater attention for different quality characteristics, though, for large files it became tedious and error prone because plotting programs sometimes could not cope with very large files directly and had some limitations. Moreover plotting a large set of EVB output data will give noisy and crowd charts and finding patterns would be impossible (e.g., up to 10^8, records in a table).

An example of PT modelling limitations and obstacles could be based on the input of the simulation or the output of the simulation (e.g., plotting a large set of the output data of such PT simulations will give noisy and crowd charts patterns and making clear fits PT patterns would be impossible). Let us consider the pure water as an example of aqueous environments to show a sample of such chart patterns in a physical system based on EVB simulation. EVB simulation will provide a long simulation for PT when placed in bulk water that consists of 125 water molecules to study the microscopic of water by means of a series of molecular dynamics simulations as explained in chapter 2. In aqueous PT, two dominant structures arise, namely the Eigen ($H_9O_4^+$) and Zundel ($H_5O_2^+$) solvation structure patterns, both complexes being the result of the solvation of the primary hydronium water complex (H_3O^+). In both cases, PT could be viewed as a pattern classification problem based on a set of EVB input features (temperature, density, number of water molecules) to classify a proton transfer as ‘transfer occurred’ or as ‘not occurred’ [104,105]. Moreover the output chart will show two different chart patterns during this long simulation: a pattern that indicates proton transferred and a pattern that indicates proton non- transferred as a function of simulation time under a specified temperature. Such chart patterns are shown in figure 3.2.

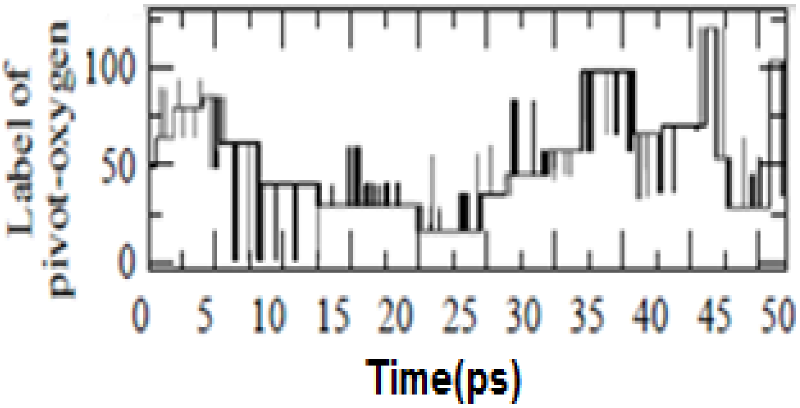

Figure.3.2: Graphical representation of original EVB simulation output data represent the time evolution of the hydronium (H_3O^+) molecule label (called *pivot* from here) in pure water at room temperature.

During the simulation as we could see from figure .3.2, each pivot will have an index, to determine the instantaneous tagged water molecule. Flat patterns indicate no transfer, whereas, permanent change of pivot label indicate that a PT has occurred. Spikes represent aborted transitions. Once characterizing the solvation of hydronium ion in water and the corresponding proton transfer episodes, chart patterns that represent ‘transfer occurred’ are the required information needed for technical analysis, in order to extract the chemical properties of this system. Herein, the excess proton will attach itself to “one” water of 125 water molecules, forming a hydronium cation with dynamical label along the simulation; many separate pieces of information may share the same pattern, and give the same shape for a series of proton transfer that may attach itself to the remaining water molecules. For example, as in this simulation the proton was attached exclusively to a little group of molecules tagged 46, 49, 100 and 20. When it comes to analyze such chart patterns, we can say that all patterns are copies of each other and do not give a clear pattern information when trying to determine the tagged water molecule, which carries the excess proton in the system, as a function of simulation time. In other words such EVB output graphical representations could not make predictions of proton movement (transferred, non-transferred). Extracting the information beyond such chart pattern is complicated because it is a crude chart pattern, and presents a totally unclear (unpredictable) scenario of proton movement along hydrogen-bonded water molecules, where the motion could be described with the wired line between two flat peaks. It is essentially a statistical problem, with the particularity that the underlying mechanism of PT is based on a quantum process. So, a correct study will need to produce more charts by changing the temperature and again that would give another chart pattern, in general many simulations will give patterns that seem similar in nature, but in fact no two patterns are exactly alike. The challenge here is how to identify the specific pattern, which help in determining the molecular chemical properties, such as proton transfer rates, diffusion coefficient of the proton, and water local density at different temperatures and so on. Finding a normal fitting linear or logarithmic line for such chart is impossible by using automatic fitting techniques of chart plotting software (e.g., Origin, Excel). Therefore, it is difficult to find pattern on such charts to enable extracting information (e.g., slope), then a pattern recognition technique would be needed here for plotting and controlling the required smooth and clear charts that leads to better visualizing and analyzing.

So, we can assume that the ANNs is an efficient approach to be applied to solve this problem in our adoptive case that do not have algorithmic solutions in which inputs and outputs variables does not have a clear relationship between them (e.g., between temperature and pivot label there is not a linear relationship). Therefore applying ANNs, for handling these PT nonlinear functions in the data filtering, data mining as well as chart pattern recognition to find a solution was adopted in this study.

Additionally, ANN fitting capability makes an attractive tool for the construction of potential-energy surfaces PES and for evaluation many physical quantities and properties based on powerful simulations. Hence, in case of PES, generally, it will be a tedious task when it comes to the construction of accurate potentials where result might need several months of ‘‘laborious iterative fitting’’. When an acceptable potential has been found, an extension for describing further bonding situations could then be very difficult due to the complex interdependence of all parameters. Over and over again a complete restart of the work is necessary. In particular in the case of force fields along with simple empirical potentials an extension to new systems regularly requires the introduction of new energy terms on a trial and error basis. Artificial neural networks approach could be considered here as a promising mathematical technique to construct PESs because ANN can ‘‘learn’’ the topology of a potential-energy surface from a set of reference points. So that in recent years, a new class of interatomic potentials based on ANN has emerged. These potentials have a very flexible functional form and can therefore accurately adapt to a reference set of electronic structure energies. Additional examples of using ANN are the construction of the relationship between experimental vibrational spectra and a multidimensional PES of macromolecules, the prediction of the outcome of a reaction without computing the individual MD trajectories, the prediction of probabilities and rates of chemical reactions the prediction of force constants and vibrational frequencies in large organic molecules and the prediction of the outcome of trajectories in atomic and molecular scattering processes [14,15,106-108]. The current status of neural network potentials has been reviewed in [109]; open problems and limitations of the use of such ANN technique besides some possible solutions were presented as well. The study addressed that ANN techniques are promising candidates for future applications in large-scale molecular dynamics simulations, because they can be evaluated several orders of magnitude faster than the underlying electronic structure energies. However, further methodical developments are needed to reach this goal. Herein [14] is a very recent study that has simulated PT reactions in liquid water by using ANN based on *Ab* initio molecular dynamics (AIMD) simulations to generate new class of reactive interatomic potentials which overcomes the limitations of AIMD simulation. The study also demonstrated the capability of ANN potentials to describe chemical reactions in the condensed phase. Another example is [15] presenting a reactive full-dimensional potential for protonated water clusters up to the octamer. A detailed investigation of this potential shows that the energetic, structural, and vibrational properties are in excellent agreement with DFT results making the ANN approach a very promising candidate for developing a high-quality potential for water. This finding is further supported by first preliminary but very encouraging ANN-based simulations of the bulk liquid [15].

In terms of molecular dynamics simulation and computer modeling, choosing the unavoidable assumptions along with an approximation and simplifications of the computational procedure without affecting extensively the property of interest is an important part of the art of such computer simulation because one of the two basic problems in the field of molecular modeling and simulation is how to efficiently search the vast configuration space which is spanned by all possible molecular conformations for the global low (free) energy regions which will be occupied by a molecular system in thermal equilibrium. The derivation of a sufficiently accurate interaction energy function or force field for the molecular system of interest is the other basic problem. A recent study [110] reports a method of conducting molecular dynamics simulations that uses an ANN to significantly increase computational speed. The technique enables dynamical simulation of hard objects with essentially arbitrarily complex geometry and is well suited to the simulation of granular matter over a wide range of densities.

Another study [111] proposed a novel potential for the water dimer, trimer, tetramer, pentamer, and hexamer that includes polarization explicitly, for use in molecular dynamics simulations. Using thousands of dimer, trimer, tetramer, pentamer, and hexamer clusters sampled from a MD simulation lacking polarization, the authors train artificial neural networks for predicting the atomic multipole moments of a central water molecule. Moreover, as mentioned before in a recent paper based on the current study we have successfully evaluated the use of the AANs methodology in the classification and predicting of PT events, and PT structure patterns and dynamical properties based on MD-MS-EVB simulations [1] which could be added to the current available literature that has been considered the ANN applications to support the theoretical modeling of PT in water.

For the sake of concision, in this section we will restrict ourselves on providing a description on how to design a learning machine tool, which mapped sets of input data onto a set of appropriate output for recognizing EVB chart patterns automatically based on ANNs networks, this tool will also allow predicting PT properties based on one test EVB simulation: (Temperature =300 K, changing the density and then predicting PT transition rate, or predict it with using greater or smaller number of water molecules, etc) as will be explained in the following sections.

3.2 Computational framework

We are going to illustrate in this section the theoretical background at the basis of the techniques we used to study the PT process in water and they are MD, MS-EVB and ANN respectively. The main structural, dynamical, and properties computed in this thesis from ensemble averages are also summarized in this section. In section 3.2.1 we will introduce a general introduction of MD, as we used numerical simulations of classical dynamics to reproduce the excess charge migration in water. Section 3.2.2 describes in particular, how we used the empirical valence bond model to numerically simulate the two relevant PT structures: called Zundel dimer and the hydronium or Eigen complex. This will be followed by section 3.3, that include the calculated quantities and computing process in line with physical mechanism of the ANN method, the source of the data set, fitting statistical functions and method validity.

3.2.1 Computer simulation experiments: Molecular Dynamics

The method of molecular dynamics solves Newton's equations of motion for a molecular system, “a given many-body systems obeying classical dynamic” which results in trajectories for all atoms in the system. It is a technique for computing trajectories. From these atomic trajectories a variety of properties can be calculated as a function of time. In this section the basic principles and approximations of MD simulations are outlined. More detailed description, several books and reviews are available [112-115]. Two main characteristics of MD, required for an N-body simulation:

- Given the following many body system that includes many particles interacting with each other (Solid/liquid: Box of Volume V, Temperature T and Pressure P: Periodic boundary conditions) in which the finite size systems clusters: Free boundary conditions).
- Given the forces acting on all the ions, and initial state at time t=0, Compute trajectories of all the particles as a function of time t, by using Newton's laws: Essentially exact

Then, the main aim of such computer simulations of molecular systems is to compute macroscopic behavior from microscopic interactions. The most important contributions a microscopic consideration can offer are (1) the understanding and (2) interpretation of experimental results, (3) semiquantitative estimates of experimental results, in addition to (4) the capability to interpolate or extrapolate experimental data into regions that are only difficultly accessible in the laboratory [116].

At this point, we have entire phase space trajectories, therefore all the information to compute various statistical quantities from microscopic description. We may write the Hamiltonian for an N-particle system as the sum of their potential energy in addition to kinetic energy when the classical description of our systems is not subject to any external field as follows:

$$H(\vec{p},\vec{r}) \equiv H(\vec{p}_1 \ ,....,\vec{p}_N,\vec{r}_1 ....,\vec{r}_N) = \sum_{i=1}^{N} \frac{p_i^2}{2m_i} + U(\vec{r}_i,...\vec{r}_N) \tag{3.1}$$

Where $(\vec{p}_1;....,\vec{p}_N)$ and $(\vec{r}_1;....,\vec{r}_N)$ represent the momenta of the particles and their positions, respectively. Newton's equation of motion can be constructed straightforwardly with the help of the Hamiltonian in order to describe the time evolution of the system, given some initial coordinates and momenta: $\dot{r}_i = \frac{\partial H}{\partial p_i} = \frac{p_i}{m_i}$,

$$\dot{p}_i = \frac{\partial H}{\partial r_i} = -\frac{\partial U}{\partial r_i} = F_i(r_i,...,r_N).$$

Herein, the Hamiltonian is conserved by these equations of motion and equivalent to the total energy conservation of the system. This provides a link between MD along with Statistical Mechanics, in view of the fact that a trajectory described by this Hamiltonian will correspond to a sample of a constant energy surface in the phase space of the microcanonical ensemble of the system.

In Physics and Thermodynamics, the ergodic hypothesis [117] says that, over long periods of time, the time spent by a system in some region of the phase space of microstates with the same energy is proportional to the volume of this region, i.e., that all accessible microstates are equiprobable over a long period of time. The ergodic hypothesis is often assumed in the statistical analysis of computational physics. The analyst would assume that the average of a process parameter over time and the average over the statistical ensemble are the same. This assumption that it is as good to simulate a system over a long time as it is to make many independent realizations of the same system is not always correct. See, for example the Fermi–Pasta–Ulam experiment of 1955 [118].

3.2.1.1 The integration of the equation of motion

Analytical solution of the equation of motion is not possible to be found in case of many particle systems, such as molecular N-body systems, consequently an approximate solution is sought. The phase space trajectory is discretized in time in addition to that the

Newton equations are solved by means of finite difference methods. Since the advent of MD [119, 120], various schemes based on finite differences have been proposed. As a rule leap-frog Verlet scheme has been used in this thesis.

$$v(t+\frac{1}{2}\delta t) = v(t-\frac{1}{2}\delta t) + \delta t a(t) \qquad (3.2)$$

$$r(t+\delta t) = r(t) + \delta t v(t+\frac{1}{2}\delta t) \qquad (3.4)$$

At intervals of mid step the velocities and current accelerations are stored and used for updating positions to the next time step $t+\delta t$. For the duration of this step, current velocities may possibly be calculated as $v(t) = \frac{1}{2} v(t+\frac{1}{2}\delta t) + v(t-\frac{1}{2}\delta t)$.

We are interested in using the largest possible time step δt for the purpose of performing simulations, with the aim of ensuring an acceptable energy conservation in addition to that it will be always shorter than the characteristic time of the fastest motions of the system. This way will allow sampling trajectories by the side of constant volume as well as energy in the microcanonical ensemble. In view of the fact that temperature and pressure correspond to the most common conditions in condensed-phase experiments, studying the properties as a function of temperature along with pressure is a much more extensive issue to be adopted, which is the case of all the works performed in this thesis, with a focus on controlling our system temperature at constant volume. Herein the Berendsen thermostat [121] has been used for the purpose of thermalizing and on average maintaining constant temperature in the simulations. In this case the idea is that by scaling the velocities at every step by a factor of $\lambda = 1 + \frac{\Delta t}{\tau}[\frac{T}{T_0} - 1]$ the system will be weakly coupled to an external heat bath by means of fixed reference temperature T_0,where τ , is the empirical parameter of adjusting the coupling to the thermal bath and T is obtained from the instantaneous kinetic energy.

Hunenberger [122] reviewed the various thermostat algorithms proposed to date, their physical basis, their advantages and their shortcomings. It is worth mentioning here his general findings about the Berendsen equation of motion which is smooth and deterministic, but time irreversible where the ensemble generated by the Berendsen equations of motion is not a canonical ensemble but the equation can produce a weak-coupling ensemble, and slightly underestimating temperature fluctuations from a truly (NVT) ensemble. Hence in the canonical ensemble (NVT), the temperature has a specified average (macroscopic) value, while the instantaneous observable representing the total energy of the system (i.e., the Hamiltonian H) can fluctuate. Accordingly, when possible, Berendsen thermostat has been used here for equilibrating the samples as well as creating runs under conditions of constant energy.

3.2.1.2 Force Fields

The quality of the model that represents the dependence of the energy of the system on its particles' coordinates plays a vital role in any successful MD simulation. The form of this potential function along with a set of adjusted parameters is what is recognized as force field (FF). In order to ensure a good accuracy in the description of the treated systems, in addition to affordable computational costs, the following potential formulations have been chosen in this Thesis. Here, we can distinguish three classes of potential models: (1) one accounting for water-water interactions, (2) carbon-water interactions and (3) proton-water interactions. Proton-carbon forces have not been considered, due to the fact that carbon atoms forming graphene sheets are neutral and, given proton's size (that of a hydrogen nucleus, without electronic cloud around, a mere point charge), and the short-ranged Van der Waals forces can be neglected.

3.2.1.2.1 Water-water forces

The expression for the potential energy invoking pair-additivity can be formulated for enormous part of condensed phase simulations of water as a sum of intermolecular ("inter") and intramolecular ("intra") terms [123]:

$$U_{\text{total}} = U_{\text{inter}} + U_{\text{intra}} \tag{3.5}$$

$$U_{\text{intra}} = \frac{1}{2}\sum_i k_r (r_i - r_{i0})^2 + \frac{1}{2}\sum_j k_\theta (\theta_j - \theta_{j0})^2 \tag{3.6}$$

$$U_{\text{inter}} = \sum_{i,j} 4\epsilon \left[\left(\frac{\sigma}{r_{ij}}\right)^{12} - \left(\frac{\sigma}{r_{ij}}\right)^{6} \right] + \sum_{i,j} \frac{1}{4\pi\varepsilon_0} \frac{q_i q_j}{r_{ij}} \tag{3.7}$$

where, in the intramolecular term: r_i is each of the atom-atom distances, r_{i0} are equilibrium values, θ_j stands for the intramolecular bending angle, with θ_{j0} being the equilibrium value. The parameters for the flexible TIP3P model employed in this Thesis are [124]:

$$\begin{aligned} k_{OH} &= 1059.2 \ \ \text{kcal/mol/}\AA^2 \\ k_{HH} &= 76.5 \ \ \text{kcal/mol/}\AA^2 \\ \theta_{HOH} &= 68.1 \ \ \text{kcal/mol/radian}^2 \end{aligned} \tag{3.8}$$

In the intermolecular term, r_{ij} is the distance between two atoms or charged sites i and j and q_i are the partial charges relative to the charge of the electron, so that the second term in equation (3.7) represents the Coulombic interactions where polarization effects occurring in condensed phases are taken into account in an average way by using effective charges. The Lennard-Jones term in water is usually applied only to the interaction between the oxygen atoms. So, the two parameters of the Lennard-Jones potential for water appearing at the first term of equation (3.7) accounts for Van der Waals interactions between oxygen particles and their values are:

$$\epsilon = 0.6364 \quad \text{kJ/mol}; \qquad \sigma = 3.1506 \quad \AA \tag{3.9}$$

Long-range interactions (Coulomb terms) were handled by Ewald sum techniques [125], assuming a uniform neutralizing background, in order to counterpart the excess proton charge included in all systems.

3.2.1.2.2 Water-carbon forces

The water-carbon interactions have been modeled by means of short-ranged 6-12 Lennard-Jones terms, where the functional form is that of first term in formula (3.7). The carbon-oxygen and carbon-hydrogen σ and ε parameters have been calculated using the Lorentz-Berthelot mixing rules [126,127]. The values obtained are [128]:

$$\begin{aligned} \sigma_{OC} &= 3.28\ \mathring{A}, \quad \sigma_{HC} = 2.81\ \mathring{A} \\ \varepsilon_{OC} &= 46.79\ \text{K} \ = 0.389\ \text{kJ/mol} \\ \varepsilon_{HC} &= 15.52\ \text{K} \ = 0.129\ \text{kJ/mol} \end{aligned} \tag{3.10}$$

where the energy equivalence is of 1 kJ/mol = 120.33 K per molecule.

3.2.1.2.3 Proton-water forces

The interaction of proton with water oxygens and hydrogens has been adapted from the successful model proposed by Voth and co-workers [71, 74, 129, and 130]. These authors considered the EVB model methodology on order to assign the closest water molecule to the proton as the *pivot* anchor, forming the hydronium ion H_3O^+, as it will be explained in the corresponding section (3.2.2). Once the hydronium ion is located, interactions with surrounding water have been taken into account. Within the EVB method, the diagonal h_{ii} and off-diagonal h_{ij} terms of the Hamiltonian are given by the following series of formulas. The diagonal terms include intramolecular interactions of hydronium and waters as well as intermolecular terms accounting for water-hydronium and water-water forces.

$$h_{ii} = V^{\text{intra}}_{\text{H}_3\text{O}^+} + \sum_{k=1}^{N_{\text{H}_2\text{O}}} V^{\text{intra},k}_{\text{H}_2\text{O}} + \sum_{k=1}^{N_{\text{H}_2\text{O}}} V^{\text{inter},k}_{\text{H}_3\text{O}^+,\text{H}_2\text{O}} + \sum_{k<k'}^{N_{\text{H}_2\text{O}}} V^{\text{inter},kk'}_{\text{H}_2\text{O}}, \tag{3.11}$$

where

$$V^{\text{intra}}_{\text{H}_3\text{O}^+} = \sum_{j=1}^{3} D_{\text{OH}}[1 - e^{-a_{\text{OH}}(R^{j}_{\text{OH}} - R^{0}_{\text{OH}})}]^2 + \frac{1}{2}\sum_{i=1}^{3} k_\alpha(\alpha_i - \alpha_0)^2, \tag{3.12}$$

and

$$V^{\text{intra}}_{\text{H}_2\text{O}} = \frac{1}{2}\sum_{j=1}^{2} k^{\text{H}_2\text{O}}_{\text{OH}}(s_i - s_{\text{OH}})^2 + \frac{1}{2}k^{\text{H}_2\text{O}}_{\theta}(\theta - \theta_0)^2, \tag{3.13}$$

and

$$V^{\text{inter},k}_{\text{H}_3\text{O}^+,\text{H}_2\text{O}} = 4\epsilon_{\text{OO}_k}\left[\left(\frac{\sigma_{\text{OO}_k}}{R_{\text{OO}_k}}\right)^{12} - \left(\frac{\sigma_{\text{OO}_k}}{R_{\text{OO}_k}}\right)^{6}\right] + c\sum_{m=1}^{4}\sum_{n_k=1}^{3}\frac{q^{\text{H}_3\text{O}^+}_{m}\, q^{\text{H}_2\text{O}}_{n_k}}{R_{mn_k}} + V^{\text{rep}}(R_{\text{OO}_k}), \tag{3.14}$$

with the function V^{rep} (R_{OOk}) is given by:

$$V^{\mathrm{rep}}(R_{\mathrm{OO}_k}) = B(1 - \tanh[b(R_{\mathrm{OO}_k} - d^0_{\mathrm{OO}})]) . \tag{3.15}$$

The Lennard-Jones parameters were given by Lorentz-Berthelot rules as:

$$\sigma_{\mathrm{OO}_k} = (\sigma_{\mathrm{O}}^{\mathrm{H_2O}} + \sigma_{\mathrm{O}}^{\mathrm{H_3O^+}})/2$$
$$\epsilon_{\mathrm{OO}_k} = \sqrt{\epsilon_{\mathrm{O}}^{\mathrm{H_2O}} \epsilon_{\mathrm{O}}^{\mathrm{H_3O^+}}} . \tag{3.16}$$

The off-diagonal terms include the coupling between diabatic states and are represented by:

$$h_{ij} = (V_{\mathrm{const}}^{ij} + V_{\mathrm{ex}}^{ij}) \cdot A(R_{\mathrm{OO}}, q) , \tag{3.17}$$

where $V_{\mathrm{const.}}$ is a constant coupling term and:

$$V_{\mathrm{ex}}^{ij} = \sum_{m=1}^{7} \sum_{k=1}^{N_{\mathrm{H_2O}}-1} \sum_{n_k=1}^{3} \frac{q_{n_k}^{\mathrm{H_2O}} q_m^{\mathrm{ex}}}{R_{mn_k}} , \tag{3.18}$$

so that

$$A(R_{\mathrm{OO}}, q) = f(R_{\mathrm{OO}}) \cdot g(q) , \tag{3.19}$$

with

$$
\begin{aligned}
f(R_{\mathrm{OO}}) = (1 + P\,\exp(-k(R_{\mathrm{OO}} - D_{\mathrm{OO}})^2))\\
\cdot\left(\frac{1}{2}(1 - \tanh[\beta(R_{\mathrm{OO}} - R^0_{\mathrm{OO}})])\right.\\
\left. + 10\,\exp[-\alpha(R_{\mathrm{OO}} - r^0_{\mathrm{OO}})]\right)\\
g(q) = \exp(-\gamma q^2).
\end{aligned}
\tag{3.20}
$$

Here R_{OO} represents the OO distance in the Zundel dimer resulting from the coupling of two diabatic states. Finally, we define:

$$
q = \frac{R_{\mathrm{OO}}}{2} - R_{\mathrm{OH}}
\tag{3.21}
$$

All parameters are reported in Table 3.1. The hydronium-carbon forces have been modeled simply using the same parameters as for water-carbon forces (3.10).

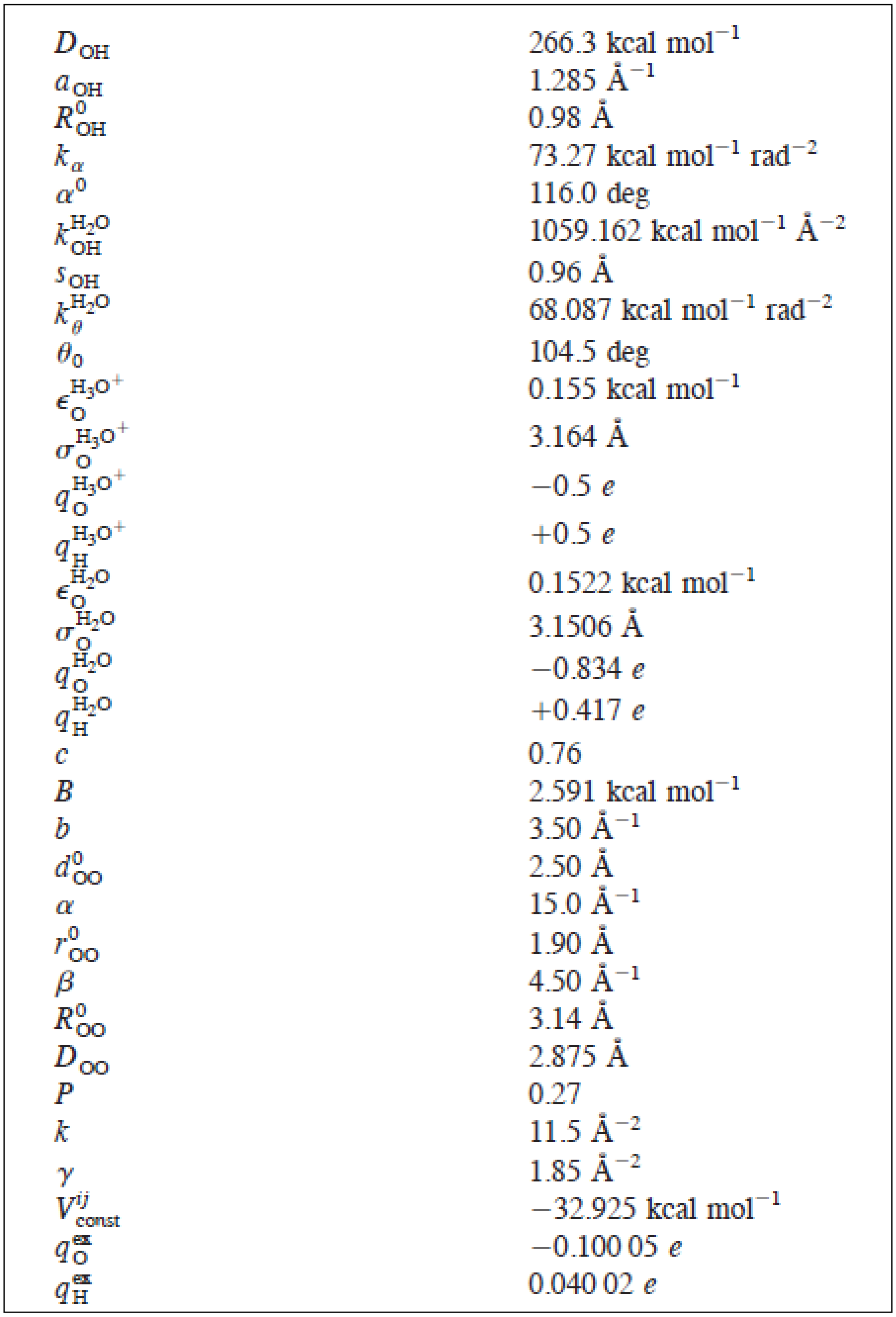

D_{OH}	$266.3\ \mathrm{kcal\ mol^{-1}}$
a_{OH}	$1.285\ \mathrm{Å^{-1}}$
R^0_{OH}	$0.98\ \mathrm{Å}$
k_α	$73.27\ \mathrm{kcal\ mol^{-1}\ rad^{-2}}$
α^0	$116.0\ \mathrm{deg}$
$k^{\mathrm{H_2O}}_{\mathrm{OH}}$	$1059.162\ \mathrm{kcal\ mol^{-1}\ Å^{-2}}$
s_{OH}	$0.96\ \mathrm{Å}$
$k^{\mathrm{H_2O}}_\theta$	$68.087\ \mathrm{kcal\ mol^{-1}\ rad^{-2}}$
θ_0	$104.5\ \mathrm{deg}$
$\epsilon^{\mathrm{H_3O^+}}_{\mathrm{O}}$	$0.155\ \mathrm{kcal\ mol^{-1}}$
$\sigma^{\mathrm{H_3O^+}}_{\mathrm{O}}$	$3.164\ \mathrm{Å}$
$q^{\mathrm{H_3O^+}}_{\mathrm{O}}$	$-0.5\ e$
$q^{\mathrm{H_3O^+}}_{\mathrm{H}}$	$+0.5\ e$
$\epsilon^{\mathrm{H_2O}}_{\mathrm{O}}$	$0.1522\ \mathrm{kcal\ mol^{-1}}$
$\sigma^{\mathrm{H_2O}}_{\mathrm{O}}$	$3.1506\ \mathrm{Å}$
$q^{\mathrm{H_2O}}_{\mathrm{O}}$	$-0.834\ e$
$q^{\mathrm{H_2O}}_{\mathrm{H}}$	$+0.417\ e$
c	0.76
B	$2.591\ \mathrm{kcal\ mol^{-1}}$
b	$3.50\ \mathrm{Å^{-1}}$
d^0_{OO}	$2.50\ \mathrm{Å}$
α	$15.0\ \mathrm{Å^{-1}}$
r^0_{OO}	$1.90\ \mathrm{Å}$
β	$4.50\ \mathrm{Å^{-1}}$
R^0_{OO}	$3.14\ \mathrm{Å}$
D_{OO}	$2.875\ \mathrm{Å}$
P	0.27
k	$11.5\ \mathrm{Å^{-2}}$
γ	$1.85\ \mathrm{Å^{-2}}$
V^{ij}_{const}	$-32.925\ \mathrm{kcal\ mol^{-1}}$
$q^{\mathrm{ex}}_{\mathrm{O}}$	$-0.100\,05\ e$
$q^{\mathrm{ex}}_{\mathrm{H}}$	$0.040\,02\ e$

Table 3.1: Parameters of MD simulation [130]

3.2.2 Empirical Valence Bond method

The essential idea is conceptually simple and is based on considering the dynamics of nuclei governed from the ground state of a valence bond Hamiltonian-type. This Hamiltonian is constructed by postulating that the possible states of the excess proton can be expressed as a linear combination of n diabatic possible states, each identified with the proton location at a specific water molecule. The Hamiltonian matrix of the system, expressed in the basis of this set of ***n*** states, has the following characteristics: The parameterization of diagonal elements include three contributions: (i) the kinetic energy of all particles, (ii) potential energy of the solvent and confining walls (considered through pseudo-potential classics that include the inclusion of intermolecular degrees of freedom) and (iii) interactions of the excess proton with the rest of the solvent and confining plates. On the other hand, the non-diagonal matrix elements are introducing the possibility of coupling between different diabatic states and thus enable the modelling of the proton transfer reaction. These elements are based on the reaction coordinate that describes the instantaneous transfer. In this section we briefly review the multi-state empirical valence bond model in order to introduce the terminology as well as setting the notation. For a more detailed description we refer the reader to the original work of Warshel [70, 73].

Herein, the EVB method assumes that the Born-Oppenheimer potential energy [131] surface $\mathcal{E}_0(\{R\})$ driving the dynamics of the nuclei with coordinates {R} can be obtained from the lowest instantaneous eigen value of the EVB Hamiltonian.

$$\hat{\mathrm{H}}_{\mathrm{EVB}}(\{\mathrm{R}\}) = \left|\varphi_{\mathrm{i}}\right\rangle \mathrm{h}^{\mathrm{ij}}(\{\mathrm{R}\}) \left\langle\varphi_{\mathrm{i}}\right|, \tag{3.22}$$

where we have adapted the criterion of summation over repeated indexes. The EVB Hamiltonian is represented in terms of the basis set $\left|\varphi_{\mathrm{i}}\right\rangle$ of diabatic (localized) VB states. In the case of an excess proton in water, these diabatic states are associated to configurations with the H^+ located in particular water oxygen. The ground-state $\left|\varphi_0\right\rangle$ of

$\hat{H}_{EVB}$ satisfies $\hat{H}_{EVB}\left|\psi_0\right\rangle = \varepsilon_0(\{R\})\left|\psi_0\right\rangle$, and it can be expanded as a linear combination of diabatic states as follows:

$$\left|\varphi_0\right\rangle = \sum_i c_i \left|\varphi_i\right\rangle \tag{3.23}$$

leading to the final expression for the potential energy surface given by the following equation $\varepsilon_0(\{R\}) = c_i c_j h^{ij}(\{R\})$, (3.24)

Dynamics of the nuclei of mass M_k is governed by the following Newton's equation of motion:

$$M_k \frac{d^2R_k}{dt^2} = -C_i C_j \nabla_{RK} h^{ij}(\{R\}), \tag{3.25}$$

In the framework of EVB methods, off-diagonal elements h_{ij} can be casted out in terms of nuclear coordinates, achieving an excellent agreement with results from full quantum calculations. The parametrization for water and hydronium species employed in the present work follows those proposed by Voth *et al.* [71, 74,129], which were applied to different environments and showed excellent agreement with experimental data. Diagonal elements h_{ii} include contributions from stretching and bending intramolecular interactions within the tagged H_3O^+ and also inside the rest of water molecules, which are modeled using a flexible TIP3P force field.

In addition, diagonal elements also include intermolecular interactions such as those between hydronium-solvent and solvent-solvent. Conversely, off-diagonal elements *hij* introduce the coupling between diabatic states *i* and *j* and have been modeled including interatomic contributions within a particular $H_5O_2^+$ Zundel water dimer spanned by states $\left|\varphi_i\right\rangle$ and $\left|\varphi_j\right\rangle$ plus Coulomb interactions between the dimer and the rest of solvent. A complete list of parameters [130] is provided in table 3.1.

Within this framework, Schmitt *et al.* were able to reproduce geometries and energies of relevant protonated water clusters ($(H_5O_2)^+$, $(H_7O_3)^+$, and $(H_9O_4)^+$), obtained from *ab initio* calculations. Oxygen-carbon and hydrogen-carbon forces were modeled by

Lennard-Jones terms with the same parametrization employed in previous works [128]. The construction of the EVB Hamiltonian was performed as follows:

Water molecule closest to the excess proton is located and identified. It constitutes the initial pivot H_3O^+ and the first diabatic state. From this pivot, the rest of the diabatic states are chosen in a tree-like construction via a HB connectivity pattern. The criterion to establish a HB is as follows: The maximum oxygen acceptor-proton donor distance is fixed up to 2.8 °A and the minimum threshold value of the H-O-O angle up to 30º.

All molecules lying in up to the third solvation shell and showing a connecting path with the original pivot were included in the construction of the L × L EVB Hamiltonian matrix, which was properly diagonalized. Typically L will be of the order of ∼10–20 units for the connectivity pattern, with fluctuations of total energy always below 1%. At every time step, PT will be made possible by reassigning the pivot oxygen label to the instantaneous state exhibiting the largest c_i^2 coefficient; from this state, the list of participating VB states was reconstructed using the connectivity branching procedure mentioned above.

Once the EVB matrix was formed, ground-state eigenvectors and Hellmann-Feynman forces were computed by means of

$$F_k = -\left\langle \psi_0 \right| \frac{\partial \hat{H}_{EVB}}{\partial X_k} \left| \psi_0 \right\rangle = -C_i C_j \frac{\partial \hat{H}_{EVB}^{ij}(X)}{\partial X_k} \tag{3.26}$$

where X_k stands for any spatial coordinate.

3.2.3 Characterization of the Hamiltonian

In this work we implemented two cases of simulations: PT in 3D (confined and unconfined water, and PT in 2D (confined systems). The last case was divided into cases of 2D simulations 1) a simulation based on investigating the effect of confinement on PT in water at 300 K (ambient conditions), 2) a simulation based on investigating the effect of temperature and confinement on PT in water.

In the case of 3D simulations, all simulation experiments corresponded to microcanonical runs at temperatures fluctuating around T =100,125,150,175,200,225,250,273, 298, 400, 500 and 600 K. In order to differentiate temperature from density effects, we kept densities constant at the value of ambient conditions ($\rho_{\omega} = 1g\ cm^{-3}$). According to the phase diagram of the rigid TIP3P model [132] such conditions would correspond to liquid water states (between 298 and 225 K) to ices (from 200 to 100 K) and to high T sub-critical states (between 400 and 600 K).

In case of 2D simulations when investigating the effect of confinement on PT, we simulated microcanonical runs at T = 100,200,300,400,500 and 600 K. In order to keep the HB network formed up to some extent (and, eventually to have the possibility of PT episodes at all states) we increased the density of the system from $0.02\,\overset{\circ}{\mathrm{A}}^{-3}$ (for a 3.1-nm-wide slab) to values $0.07\,\overset{\circ}{\mathrm{A}}^{-3}$ (for a 0.7-nm-wide slab). This means that the simulations were performed with 125 water molecules in all cases into a slab of width ranging from d = 3.1 to 0.7 nm. According to the phase diagram of the rigid TIP3P model the states at 300 K correspond to liquid water and those of 200 and 100 K to low density amorphous ices ices. States over 300 K (400 to 600 K) have not been evaluated for this case, but we believe that at the pressures considered in this work, all of them will correspond to liquid or very dense vapor states.

However, all of these assignments of physical states of our (3D and 2D) simulations are only approximate , since (1) our model includes flexibility of the molecular bonds and (2) the pressure in our system will fluctuate, given that we performed our simulations at the microcanonical ensemble (fixed number of particles, volume, and energy), allowing temperature and pressure to slightly fluctuate. As a matter of fact, temperature variations are always small (within 3%), whereas the range of pressure fluctuations is up to 15% of the mean value.

Finally in all cases the time step was set to $\Delta t = 0.5$ fs. We considered equilibration periods of approximately 20-30 ps, followed by trajectories of hundreds of ps, used to obtain meaningful statistical properties.

3.3 Calculated quantities

Under the ergodic hypothesis, averages over the trajectory of a system obeying Hamilton's equations are thus equivalent to averages over a microcanonical ensemble. This will allow using all statistical mechanics tools for connecting microscopic details available from the simulated trajectories to physical observables such as equilibrium thermodynamic properties, transport coefficients, and spectra. Through MD we are able to produce trajectories in the microcanonical or canonical ensembles by numerically integrating the equations of motion for a Hamiltonian that accurately describes the system under study. Our MD simulation will produce the related trajectory data, which consists of the position, velocity, and energy of each particle at every time point considered in our under study PT simulations. As a final point ergodic hypothesis can be invoked to justify equating trajectory averages with ensemble-based thermodynamic properties. But the strength of MD over statistical mechanics is that detailed trajectory histories are available and thus quantities defined in terms of atomic motion or position can be investigated in addition to statistical mechanics observables which can be used as an input for the ANN pattern recognition tool. Therefore, several “computing tools” ,i.e., plotting, chart fitting, automated chart pattern recognition and data mining tools have been linked to our EVB simulation in one framework to get better visualization and to enable analyzing , computing, and evaluating the following physical properties i.e., (dynamics of proton transfer, solvation structure, proton diffusion and spectroscopy) including the analysis of calculated radial distribution function RDF, via applying statistical mechanics to derive information on macroscopic observables from the generated microscopic data which will be saved in the database of the framework after each simulation. The physical mechanism of the use of these tools is presented in the following section including the calculated quantities. The details of the calculated quantities and their related statistical theories will be explained in section 3.3.3 in details.

3.3.1 ANN application: Pattern recognition and data mining tool

We proposed a chart pattern recognition tool that was optimally programmed by using Python to work as a first helpful ready to use add-on tool of the MS-EVB simulation. This tool is expected to provide a better visualization of the graphical representation of EVB output data, plus enabling automatic recognition of patterns on charts based on well-known filtering, correlating and classification functions.

It was designed to serve two purposes: 1) Facilitating the work of analysing output data of PT case under study after running separated specific simulations by the use of data mining and chart pattern recognition, to be applied with independent goals at each stage of the process to control charts in monitoring and filtering EVB output files with more accuracy, therefore, if any ‘out of control’ condition should be found, the reasons for the variation outside the stable patterns would be discovered. 2) Predicting PT chemical properties for future modelling (e.g., predict the number of water molecule at 300 K in case of changing the confinement volume based on historical or experimental data and so on). Afterwards, the proposed tool will simply enable the technical analysis of several important chemical properties, by means of the EVB simulation output graphical data, having the aim of enhancing the performance and efficiency for systems of large amounts of molecules.

In this pattern recognition tool, ANN with back propagation function were applied to the literature data generated by EVB simulation, and stored in a database to construct a classifier system which could be used to predict and analysis the chemical properties of proton transfer phenomena in aqueous environments based on chart patterns. These properties are: the proton transfer rate, the hydronium-water local density field, the diffusion coefficient of proton, and its velocity.

In other words, this model would be a physically based model. Firstly, EVB must be run to generate data of possible conditions based on changing the input parameters to compose the output data sets in the database. Subsequently, this data would be used as input in the current ANN model. Of course, the model techniques could only pickup the required behaviour if the available physical condition were accurate and describe the relevant process in detail. The challenge of composing the input file of the tool by choosing the right data and the right examples for the training phase is often the most complicated part of using the ANN pattern recognition technique.

The data must be processed before applying the ANN approach and there are some modifications that must be made to the data set to make it perform better in the training phase. Herein, from the normalized database, the ANN will be trained with N data points and tested (or validated) with N points based on the case study and the selected chemical properties to be predicted, for example, how to predict the proton transfer rate based on the chart patterns, as it is fully explained in the section of case study and presented in figure 3.3.

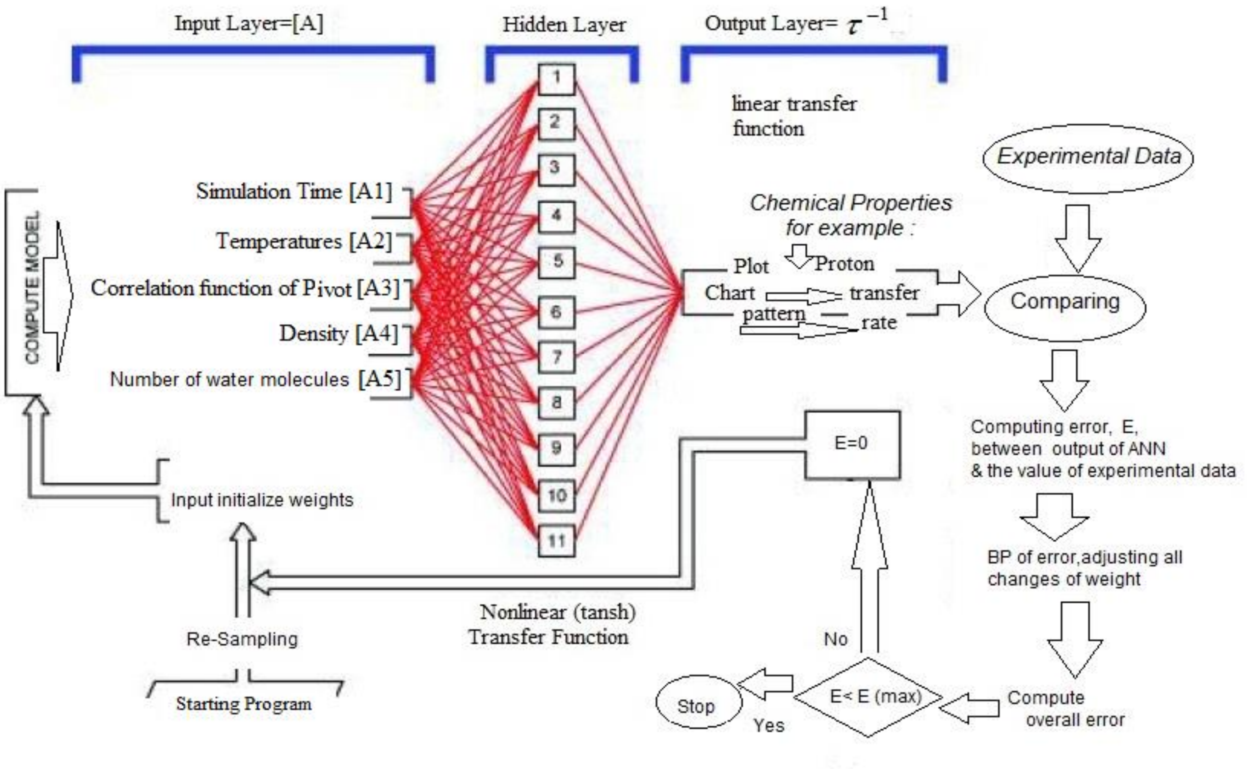

Figure 3.3: Optimal ANN structure, together with a flowchart of the back propagation (BP) algorithm [89] for the prediction of proton transfer rate, plus the basic algorithm loop of the proposed tool, that will be fully explain in the case study.

As the tool will provide an easy to use database, where the original EVB calculated and collected data would be represented in the form of database files (i.e. output of EVB) after several simulations, as shown in figure 3.3 and figure 3.4 ; these data might be then cleaned resampled or reduced by using ANNs data mining techniques; and feature extraction algorithms, the feature space dimension might be reduced; the system would then use description algorithms or classification algorithms based on the requested diagnostic purpose [89]. For instance, the system could predict the proton transfer and describe patterns in different classes depending on their characteristics thus to cope with the nonlinearity of the EVB input and output (see figure 3.1 and 3.4).

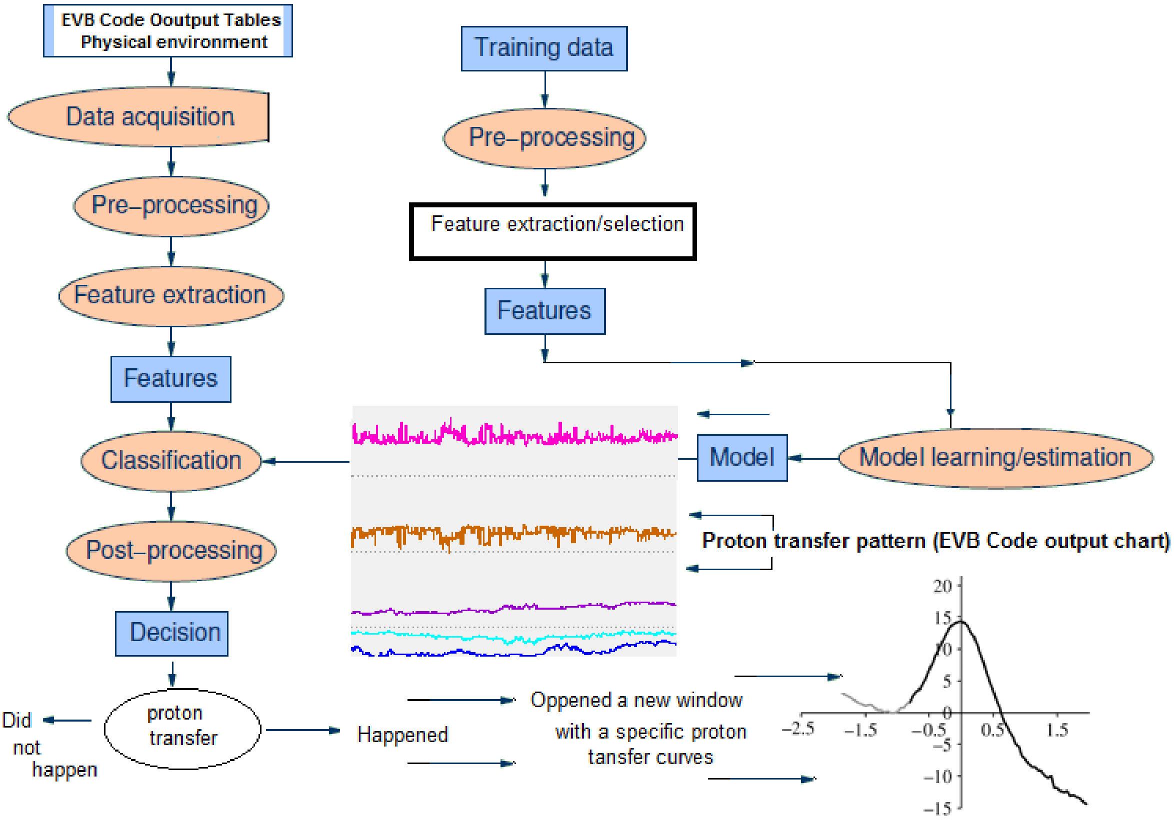

Figure 3.4: Object/process diagram of the proposed chart pattern recognition system following the typical pattern recognition system architecture of Schalkoff [133].

3.3.2 ANN Computing process

Generally, the computing process of the ANN algorithm are typically defined by three types of parameters: the interconnection pattern between different layers of neurons, the learning process for updating the weights of the interconnections and the activation function that converts a neuron's weighted input to its output activation. Consequently, during the computational process, our tool would allow the operating BP algorithm in two phases via its graphical user interface (GUI):

- **Training phase**, where the training data samples would be provided at the input layer for training the network with predefined set of data classes. The ANNs would be trained using a BP algorithm, based on the concept of improving the performance of network by reduction of the error from the output data [104]. Once the network is trained, it could be saved for further use. The program uses data files, which have been computed using EVB, as the main source of data for pattern recognition of proton transfer and it could be considered then as time series data of the selected required input. This is true for all other input and output parameters (e.g. ‘number of chemical species’; ‘masses’; ‘number of atoms of each species’; ‘temperature’; ‘simulation time’; ‘density correlation function of pivot’, etc). In short for training multilayer perceptron algorithm MLP the problem of estimating the weights consists of the following parts: Initializing the weights randomly; computing the derivative of the error function with respect to the weights via the error back propagation algorithm, updating the estimated weights via the gradient descent or scaled conjugate gradient method [134]. Hence, a multilayer perceptron (MLP) is a feedforward artificial neural network model that maps sets of input data onto a set of appropriate outputs [135]. An MLP consists of multiple layers of nodes in a directed graph, with each layer fully connected to the next one. Except for the input nodes, each node is a neuron (or processing element) with a nonlinear activation function. MLP utilizes a supervised learning technique called backpropagation for training the network.

MLP is a modification of the standard linear perceptron and can distinguish data that are not linearly separable [136].

- **Testing phase,** during this phase the input layer would be provided with a random test data (experimental) to predict the applied patterns. Several experimental data were conducted to the new tool database; to compare the ANN results with the experimental values in the testing phase for providing validity and accuracy [134].

For more explanation, the user of the proposed tool will start providing the algorithm with examples of target output data; furthermore the network will change the network's weights so that, when training will be finished, it will give the user the required output for a particular input. Each input pattern of this training set would be applied to the input units and then it would be propagated forward. The pattern of the activation arriving at the output layer would be compared with the correct (associated) output pattern for calculating an error signal. The error signal for each such target output pattern would then be back propagated from the outputs to the inputs in order to appropriately adjust the weights in each layer of the network. The procedure would be repeated until the error function would reach the range of the error tolerance factor that had been set by the user. After back propagation network had been learned the correct classification for a set of inputs, it could be tested on a second set of inputs to see how well it classifies untrained pattern. In this case, the back propagation network could make a reasonable prediction about what data that was missing from the current available information of a hidden data which is a very difficult task to be done in real world, but the use of BP technique of this tool would allow user to guide the tool to find some corrected pre-information (such as desired output) as shown in figure 3.3.

3.3.3 General steps of the data set preparations and calculated quantities

This part is very important because the ANN tool is only as good as the quality of the data set; in this part user can create the ANN input file by re-sampling output files of EVB that is available in the database. The proposed tool will consider a number of factors as input, in order to produce an output, which will give the result of whether a proton suffered a transfer episode or it did not. In many computational methods any small change in the input pattern might impose a drastic change in the desired output pattern [89,137], so that, in order to get the best classification performance evaluations, this tool provides two kinds of data modification techniques, which could be easily controlled from the main window on click. They are as follows:

3.3.3.1 The ANNs modification parameters of learning and testing

As the accuracy of the ANN network output is dependent upon the accuracy of the analytical numerical model used for training this network user of this tool can continue examining the behavior of changing the value of modification parameters of learning and testing algorithms on the output results with comparing it with an available experimental value, thus to investigate under what cases the pattern recognition tool could effectively be used for the prediction of proton transfer's chemical properties. Accordingly, these fitting parameters would be some constants for adjusting the algorithm of computational process [138] from the main window related to:

- The construction of the neural network itself (e.g. the number of hidden layers, the number of neurons in each hidden layer, the nature of the node nonlinearity that was used in the hidden layer (sigmoid or tansh) [134].
- The generalized delta rule (e.g. learning rate, momentum term and the set of initial weights) [134].

3.3.3.2 ANN input modification functions

These functions could be defined as regularities in the output data of EVB simulation to create the required chart patterns following statistical functions. In other words these function are a technique to modify the ANN input data set, firstly the tool will extract data set from the large EVB output tables subsequent to any specified case study, then the user will determine the related fitting function on click from the main window to generate the required fitting input to be learned and tested via neural network, any time user could adjust the two fitting techniques spontaneously, and continue attempting until reaching a smooth chart pattern instead of the original crowd chart pattern of EVB data that shown in figure 3.2 . This tool will provide a good statistical technique to enable plotting smooth charts patterns to study the local structure of the hydrated proton and the nature of proton transfer dynamics in different aqueous environment. On the other hand the tool provides four types of fitting function (physical regularities on PT) as follows:

3.3.3.2.1 Local structure of the hydrated proton: Hydronium-water local density field

As the presence of an excess proton in water promotes a disruption in its local hydrogen-bond structure, the structure of water is therefore fundamentally important for characterising the nature of the hydrogen bond at the atomic level. In confined environment with a similar fashion as it happens when a solvated ion in water produces a large anomaly in the tetrahedral structure of the bulk liquid, the presence of an excess proton also creates a disruption in its local hydrogen-bond structure. When a PT event occurs, the structure around the lone proton changes dramatically as explained in chapter 2, three relevant complexes may arise: the proton attached to a single water (single hydronium, H_3O^+), the so-called Zundel dimer $(H_5O_2)^+$ and the three-coordinated hydronium $(H_9O_4)^+$ known as the Eigen complex. It is commonly accepted that PT is the result of the continuous interconversion of the three above mentioned structures, with percentages of each depending on the thermodynamic conditions of the system. In most cases, continuous interconversions between the Zundel and Eigen complexes generate a hybrid $(H_9O_4)^+/(H_5O_2)^+$ structure. Each transfer of the lone proton between two water molecules will involve changes in pivot oxygen-water oxygen O^*-O and pivot oxygen-water hydrogen O^*-H distances and changes of the local hydrogen connectivity pattern between the complex at its closest solvation shells [39, 40].

Herein in condensed matter, pair distribution functions can be used for revealing the structural correlations. The structure of water is therefore fundamentally important for characterising the nature of the hydrogen bond at the atomic level. The radial distribution function (RDF) is a useful tool to describe the structure of a system, particularly of liquids and it is the most commonly used function for addressing the local structure in liquid-state physics. In general, when there are two solutes dissolved in water, the Brownian motion separates them by different distances r at different time. The radial distribution function, $g_{\alpha\beta}(r)$ gives the probability of finding a particle in the distance r from another particle. If we count the appearance of two molecules at separation r, from $r = 0$ to $r = \infty$, we can get the radial distribution function $g_{\alpha\beta}(r)$ (or pair correlation function) [131, 138].

This function describes the local environment of any reference particle, in this case the oxygen atom of the water molecules, in terms of the probability to find a neighboring particle located at a distance r. It gives the probability of finding a pair of atoms at a distance r apart, relative to the probability expected for a completely random distribution at the same density. RDF's reveal the local structure of the system but it only give information about inter-particle distances. The results can be compared as well with X-ray and neutron diffraction experiments. For computing it in numerical simulations, we average over several configurations the number of β particles n_β inside a spherical layer of thickness Δr at a distance r from α particles $g_{\alpha\beta}(r) = \frac{V}{N\beta}\frac{\Delta n\beta(r)}{4\pi r^2 \Delta r}$, Herein $V = L^3$, with L being the box length and $\Delta n_\beta(r)$ stands for the number of β particles inside a spherical layer of thickness Δr and radius r centered at an atom α. This will be a part of the output data but of the MD-EVB simulation. In this study we expect that both temperature and confinement will have observable effects on the local proton structure. In the case of a distinguishable particle, such as the proton, we can analyze solvation structures by means of local pivot oxygen-water (O, H) density fields given by:

$$\rho_{0*\alpha}(r) = \frac{1}{4\pi r^2}\left\langle \sum_i \delta\left(\left|r_{0*} - r_i^\alpha\right| - r\right)\right\rangle \qquad (3.\ 27)$$

This give us an information equivalent to RDF, when a tagged particle (O^*) i present at the system.

Using this fitting function will allow composing an input file for the ANN tool through spatial correlations with respect to the hydronium label, where r_{0*}, is the coordinate of the instantaneous pivot oxygen and r_i^{α} is the coordinate of site $(\alpha = \mathrm{O}, \mathrm{H})$in the i-th solvent molecule. This will allow displaying the oxygen-oxygen $\rho_{0-0}(r)$ and oxygen-hydrogen $\rho_{0-H}(r)$radial density fields to compare local structures produced by different FF's or between optimized FF's and reference based on the output data of the EVB simulation.

This input will be tested with neural networks until getting a smooth chart which to present the locations of main important peaks at different pivot solvent density fields. On the other hand the tool provides a special fitting function to deal with O^*'s z-position O_Z^* at different slab widths for evaluating the location and mobility of the proton species, based on computing oxygen pivot O_Z^* position in case of confinement at different slab widths, (between *d* = 3.1 and 0.7) nm, for a time interval of 50 ps.

To evaluate the location and mobility of the proton species based on the output data of EVB simulation we need to detect the oxygen pivot O_Z^* position at the required slab widths, for a specific time interval because the proton z-position is extremely important for monitoring the simulation, we need to make sure that the proton is there (inside the width of the determined slabs) and also, the proton must fulfill the condition: $-13.6 < Zp < 13.6$. Therefore the ANN tool allows extracting the related coordination data by a direct reading from the large output files of the EVB simulation. The tool will simply allow output data re-sampling for finding the required $Zp's$ to work as input file for the fitting function $\delta Z_P(t) = 16.5 - |Z_P|$.The output files will be t and $\delta zp(t)$ to draw the related chart pattern through the fitting process based on $\vec{r}_i = (x_p \hat{i} + y_p \hat{j} + z_p \hat{z})$ and

$\vec{r} = (x_0\hat{i} + y_0\hat{j} + z_0\hat{z})$ with $r = \sqrt{(x_p - x_0)^2 + (y_p - y_0)^2 + (z_p - z_0)^2}$ the tool will find $r_i - r$ list, then automatically, which means that the range for sorting data is restricted to the $(\mp)$ slap width as shown in the figure 3.5.

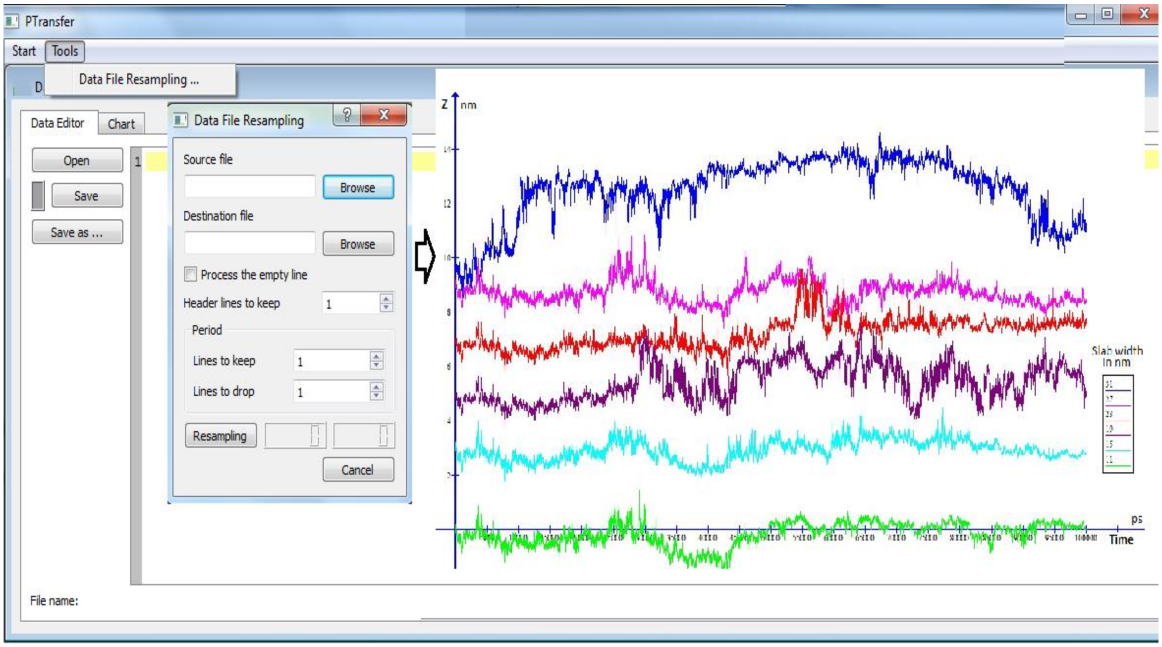

Header lines to keep: 1
Lines to keep: 1
Lines to drop: 1

Figure 3.5: Proton Z- position data, re-sampling and fitting ANN window.

3.3.3.2.2 Proton transfer dynamics: Population relaxations and proton transfer rate

This tool allows initial analyzing of the nature of the proton transfer dynamics in liquid water and ices by direct inspection of the time evolution of the pivot oxygen label during 50 ps time intervals based on extracting the related data for plotting the related charts of “time evolution of pivot-oxygen labeling in different aqueous environments”. But such charts will illustrate a rough picture of PT dynamics as described before in figure (3.1) which cannot provide a quantitative estimation of PT rates. However, this tool allows improving the calculations based on using time correlation functions. In order to do this, we need to ensure that PTs are sufficiently frequent to collect statistics. This happened in all cases for the full length of our simulations (250 ps).

This tool provides a good technique to enable plotting smooth charts patterns to study the nature of proton transfer dynamics in different aqueous environment, therefore, figure 3.1 could be significantly improved by performing an analysis based on time correlation functions following literature study [71,139]. The general form of equilibrium time correlation functions for the population relaxation of different reactant species is as follows

$$C(t) = \frac{\langle \delta h_i(t) \bullet \delta h_i(0) \rangle}{\langle (\delta h_i)^2 \rangle} \qquad (3.28)$$

where $\delta h(t) = h(t) - \langle h \rangle$ describes the instantaneous fluctuation of the population of i-th reactant away from its equilibrium value. The characteristic function is $h_i(t)=1$ if the tagged reactant species, i.e., "if the hydronium label at time t corresponding to the i-th water molecule" is present in the system at time t and $h_i(t)=0$ otherwise.

With such choice we can expect that C(t) defined in equation (3.16) will show at least three qualitatively different time domains: (1) a *resonant* time τ_{rsn} in the subpicosecond scale, associated to the rapid exchange of the pivot label, i.e., the excess proton, along a "special" bond, represented by spikes in the history of the pivot labels depicted in the charts of the EVB time evolution of pivot-oxygen labelling in different aqueous environments; (2) an *intermediate* time τ_{prs} characterizing the lifetime of the *resonance episodes* and (3) the *residence* time τ_{rsd} of the proton when attached to one particular pivot water. In case of confinement simulation this time should be equivalent to the integrated relaxation time defined in Ref [66] as well as other calculated quantities which is the most equivalent recent references. To mention some other related up to date references we have to mention the work of Wolf and Groenhof [140] which they have proposed new classical model with explicit proton transfer by providing a way to model PT in a very efficient computational procedure using classical force fields, but still capturing the key aspects of the phenomenon.

Herein population relaxations of the pivot label are the most natural functions to investigate our adoptive cases. As it is usual in EVB-MD simulations of PT in water, population relaxations of the pivot label are the most appropriate stochastic functions to compute, since the jump patterns of the excess proton are simply a sequence of PT episodes, in a large number of cases in this work we may deal with "*resonant*" episodes where the proton resonates between two valence bond states having large c_i coefficients of equation (3.12), the so-called "special" bond [75], including aborted transitions, represented by isolated spikes.

The power of chart pattern recognition will be appeared at the last smooth chart so that plotting this chart with respect to time will represent a fitting chart and smooth chart, thus it will simply allow calculating the slope as

$$k_{PT} = \lim_{t\to\infty}\left(-\frac{d\,lnC(t)}{dt} \right) \tag{3.29}$$

According to Onsager's regression hypothesis [138] the proton transfer rate τ^{-1} can be obtained as temporal decay of $c(t)$ at long time span [141]. The span will be changed on click from the tool GUI until finding a reasonable value of rate. Correspondingly, average mean residence time of the proton in pivot water could be estimated from the following equation

$$\tau_{rsd}=k_{PT}^{-1}\,. \tag{3.30}$$

3.3.3.2.3 Proton transfer dynamics: Diffusion coefficient of proton

The diffusion coefficient of aqueous protons at ambient conditions is known to be approximately fourfold that observed for neat water. So, the experimental value is of $0.93\,\overset{\circ}{\mathrm{A}}{}^2$/ps [142] for a proton diffusing in water at 298.15 K and at the density of $1\mathrm{gcm}^{-3}$, whereas the value of the diffusion coefficient of bulk liquid water is of $0.23\,\overset{\circ}{\mathrm{A}}{}^2$/ps [143]. The main reason for such an enhancement of the diffusion is well known and is based on the Grotthuss translocation mechanism [25], in addition to the usual hydrodynamic

Stokes mass diffusion. This scenario will be compared with our results based on the present output data of the MD+MS-EVB simulations, and our calculation of diffusion coefficients of aqueous protons D_p that obtained from long time slopes of mean square displacements of the proton coordinate r_p, following Einstein's relationship [137]:

$$D_p = \frac{1}{6} \ell im_{t \to \infty} \frac{d\left\langle \left| r_p(t) - r_p(0) \right|^2 \right\rangle}{dt} \tag{3.31}$$

Where the proton coordinate was defined as a weighted sum of the coordinates of the L pivot molecules r^i_{pvt}:

$$r_p = \sum_i^L c_i^2 r^i_{pvt} \tag{3.32}$$

The analyzing tool also provides a fitting function to allow automatically computing the diffusion coefficient of the proton .The user will simply compose the input file based on data set (Time, X_P, Y_P, Z_P), to calculate the mean square displacement and then test this file with neural network until getting a smooth chart to find the slope shown in the following function,

$$\frac{d\left\langle \left| r_p(t) - r_p(0) \right|^2 \right\rangle}{dt}, \tag{3.33}$$

and then related D_p pattern.

3.3.3.2.4 Proton transfer dynamics: Proton spectroscopy fitting function

As mentioned before, the widest employed experimental tools for the study of the microscopic vibrations of water are Raman and infrared spectroscopy. Infrared spectra report properties such as the absorption coefficient, α (ω), or, equivalently, the imaginary part of the dielectric constant, $\varepsilon''(\omega)$ [134], which are of quantum nature. Such properties can be computed in our MD-EVB framework with the aid of an absorption line-shape function $I\ (\omega)$, i.e., the Fourier transform of the time derivative of the dipole moment, $\mu(t)$ [144].However, these functions may include oscillations that eventually reduce the quality of the spectral densities obtained from MD. To cope with this issue our ANN tool provides a fitting function to allow computing an alternative observable, namely the velocity autocorrelation function of the lone proton

$$\mathrm{C_P(t)} = \langle \mathrm{V_P(0)} \cdot \mathrm{V_P(t)} \rangle \tag{3.34}$$

Where the proton velocity $vp(t)$ can be obtained directly from the time derivative of its position $\mathbf{r}_p$:

$$V_P(t) = \frac{dr_P(t)}{dt} \tag{3.35}$$

Based on equation (3.22) and by means of the usual Fourier transform, we can then obtain the vibrational density of states $S_p(\omega)$ [130] given by the following equation

$$\mathrm{S_p}(\omega) = \int_0^\infty \mathrm{dtC_P}(t)\,\mathrm{e}^{i\omega t} \tag{3.36}$$

Therefore this tool will simply allow computing the $S_p(\omega)$ for all slab widths considered along the present work based on extracting and fitting the related $V_P(t)$ data from the EVB simulation output files in order to create the required chart pattern.

3.4 Running the EVB pattern recognition tool

Our new ANN tool could be easily running via its flexible GUI to control running the EVB simulation including its add-on ANN tools. Fig 3.6 presented the main window of the tool. Screen monitor appeared while running the EVB simulation. After setting the input file, at any time user can stop simulation. During the simulation the tool will continue plotting patterns step by step, at the end user can start data file re sampling from “tool menu”, to find pattern on charts and plot smooth charts, as shown in figure 3.7.

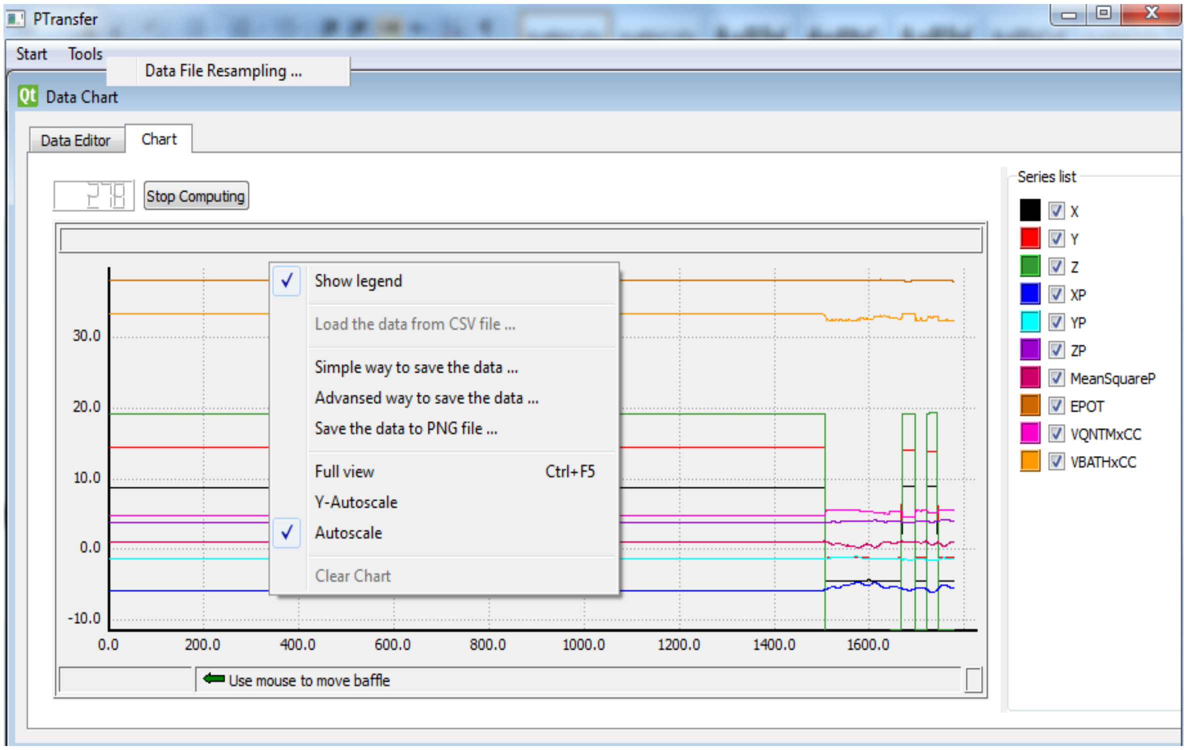

Figure 3.6: The main window of *Ptransfer*

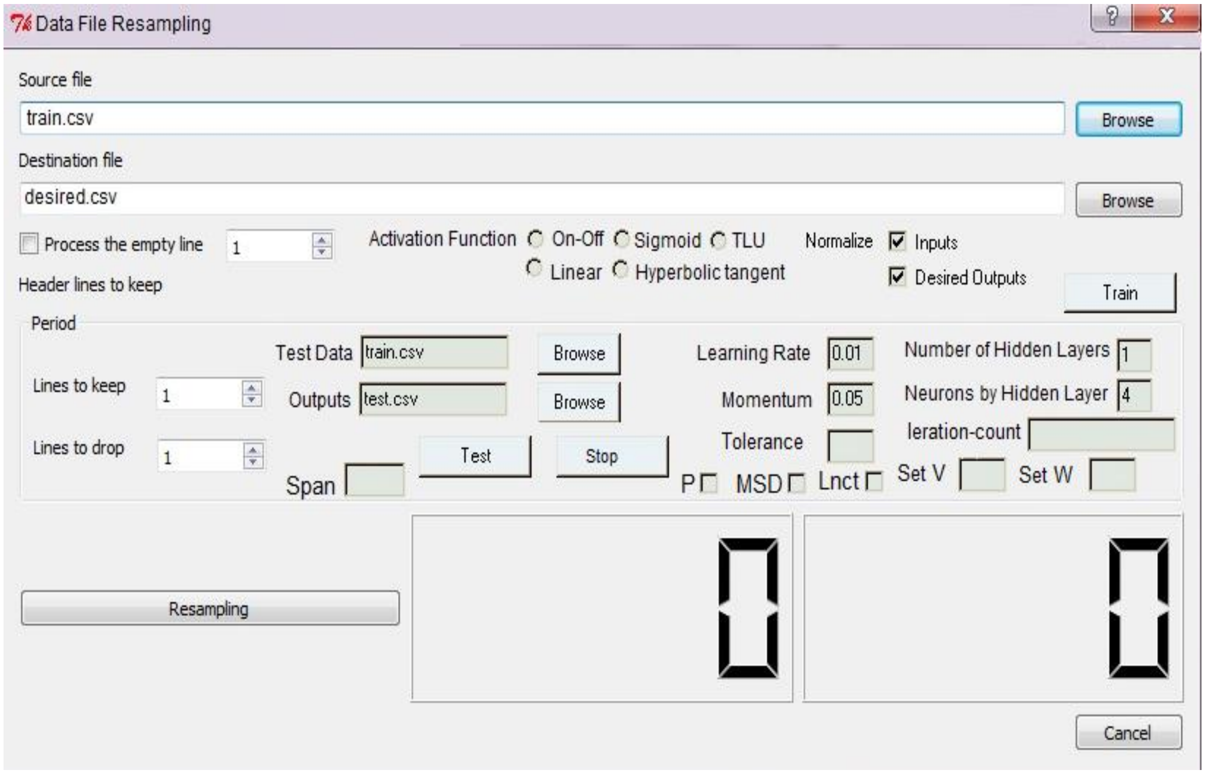
Source file: train.csv

Destination file: desired.csv

☐ Process the empty line: 1

Activation Function ○ On-Off ○ Sigmoid ○ TLU ○ Linear ○ Hyperbolic tangent

Normalize ☑ Inputs ☑ Desired Outputs

Test Data: train.csv

Outputs: test.csv

Learning Rate: 0.01

Momentum: 0.05

Number of Hidden Layers: 1

Neurons by Hidden Layer: 4

Lines to keep: 1

Lines to drop: 1

Figure 3.7: The main window of the ANN application, which is the add-on tool of EVB simulation (data filtering and re-sampling, data editor including and file manipulation).

From the GUI of the tool, the user could start training and testing the output data of the EVB code. Herein, ANN network had to be setup according to the user needs. Choosing the number of neurons as the number of possible classes in the data would be strongly recommended. User needs just to enter historical data as inputs and results (desired outputs) by browsing the saved output file from any computer directory (C, D, E…etc). If user wants a pattern recognizer, then he must use a column for each pattern in the desired outputs table as appeared in figure 3.8.

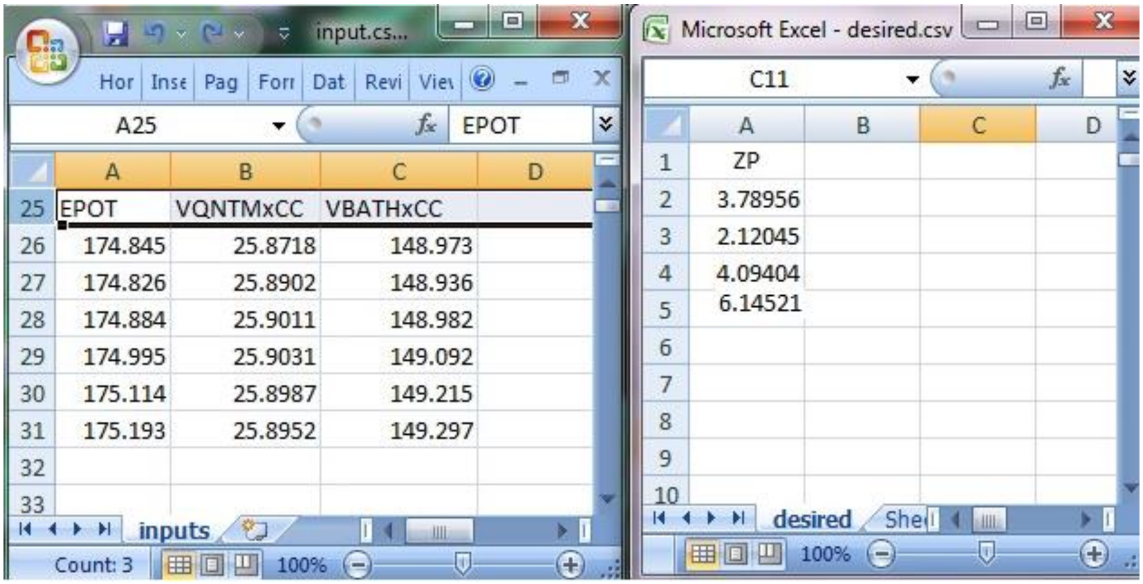

	A	B	C	D
25	EPOT	VQNTMxCC	VBATHxCC	
26	174.845	25.8718	148.973	
27	174.826	25.8902	148.936	
28	174.884	25.9011	148.982	
29	174.995	25.9031	149.092	
30	175.114	25.8987	149.215	
31	175.193	25.8952	149.297	
32				
33				

	A	B	C	D
1	ZP			
2	3.78956			
3	2.12045			
4	4.09404			
5	6.14521			
6				
7				
8				
9				
10				

Figure 3.8: Input data set, two files of training phase

The user should use the “browse” button in the main screen to enter the two required input files to be trained after pressing “train”: file1 (input.csv), file2 (output.csv). Data set consists of two inputs (I_1 and I_2) and one output (O). Here there are some re-sampled data from the computed results of EVB output. But user can set the values based on his case study just to learn the network. Once the neural network would be trained, user could use new sets of data (test) to predict their possible results (outputs) according to what was learned in the training, as presented in figure 3.9.

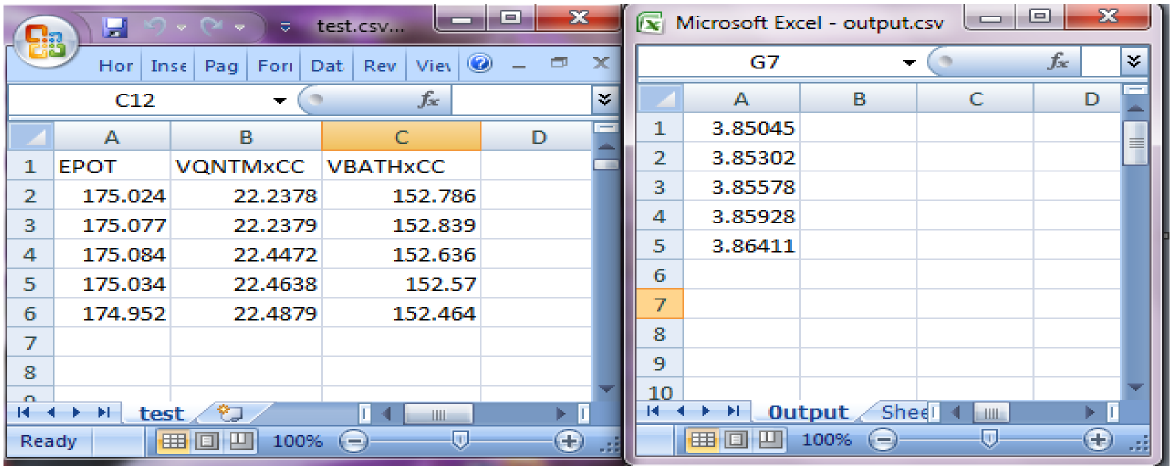

	A	B	C	D
1	EPOT	VQNTMxCC	VBATHxCC	
2	175.024	22.2378	152.786	
3	175.077	22.2379	152.839	
4	175.084	22.4472	152.636	
5	175.034	22.4638	152.57	
6	174.952	22.4879	152.464	
7				
8				

	A	B	C	D
1	3.85045			
2	3.85302			
3	3.85578			
4	3.85928			
5	3.86411			
6				
7				
8				
9				
10				

Figure 3.9: Inputs files for testing phase insert them then press test

On the other hand, as patterns and relationships between numbers are often easier to recognize when shown in a chart, this tool allows drawing charts simply by loading files from database with EVB output results to the main window of the tool on a right click, (see figure3.6). After re-sampling the required file of a large set of data, the user can set required fitting function ($v_p(t)$, $\ln C(t)$, MSD,..., density fields...etc) on click, directly a new window will be open with presenting the required chart pattern to start analyzing data, for more accuracy user can change the ANN fitting parameters constant until getting a satisfied result as would be explained in the case study. The tool could be used for analysing one or several separated simulations as well as predicting (to be used in modelling larger PT simulation in future work based on the current historical data).

3.5 Finding proton transfer chemical properties in aqueous environments based on the ANN method

This section presents the using of ANN tool for solving a real problem, in this situation this required expanding the example that appeared in figure 3.1 and taking into account the tool structure diagram of figure 3.3 to see how it logically works and how to get better output results.

3.5.1 Physical Case study

It is well known that confining environments, with characteristic lengths at the nanometer scale, are able to significantly change the equilibrium properties and dynamics associated with any reactive process in solution. In this regard, this case study will show how to provide the EVB simulation with clear chart patterns to analyze the structural properties and dynamics of solvation of an excess proton located in aqueous environments of pure water, in order to find the most important chemical propriety, the so called proton transfer rate. We assume that this example could be repeated using another environments for predicting, e.g., strong acids and ionic solutions confined in different geometries, varying from hydrophobic to hydrophilic nature.

3.5.1.1 Data statistics of model variables

Variables	Range
Input layer [A]	
Simulation Time [A1]	1 – 100000 fs
Temperatures [A2]	T=250, 273, 298 K
Correlation function of Pivot water[A3]	1-300; data modification to reduce the size of data set of simulation time from 100000 to 300 based on the number of tagged water molecular (i.e., 49, 64, 118…).
Density [A4]	0.0333 Å^{-3}
Number of water molecules [A5]	125 to 400
Output Layer	
Proton transfer rate	could be any known experimental value

Table 3.1: Model variables for computing proton transfer rate.

This example is to run an EVB simulation for a long simulation (10^5 fs) of time, for evaluating the proton transfer rate in a bulk of pure water with 125 water molecular at density 1 gcm^{-3} and three temperatures T=250, 273, 298 K based on using the new tool. User has to run the EVB for generating the output files for the three temperatures. These output files will be stored in the new tool data base to be used as an input of the ANN pattern recognitions tool, starting with composing the sample of input data with extracting and fitting the required data, simply on clicking the related icon from the main window of the tool, in this case $\ln C(t)$ will be the target.

As we pointed out above, this statistical function could be defined as regularities in the output data of EVB in order to create the required chart patterns of proton transfer. The computed value of proton transfer rate in this case study was training and testing several times by changing the number of neurons in hidden layer, thus for achieving more accuracy during learning process, this constant has been changed randomly from 1 neuron to 15 neurons using the main window after several runs. Then, another attempt could be done with using other constants. This allows training the modified data with different initial values of the hydronium label values in order to reach a suitable average data set. Figure 3.10 (a), presents three crowded chart patterns, figure 3.10. (b) presents results obtained for the dynamics of proton transfer and their conversion to a simple chart, by using new computational tools, comparing the two figures showed that smooth chart in figure 3.10 (b) are only a patterns of proton transferred “occurred”, which presents a clear behaviour with respect to time, that could be used to analyze proton transfer instead of using the unsophisticated chart of figure. 3.10(a). One additional feature is that the tool will allow drawing the three charts together with the experimental chart in single one chart, as shown in figure 3.10 (b).

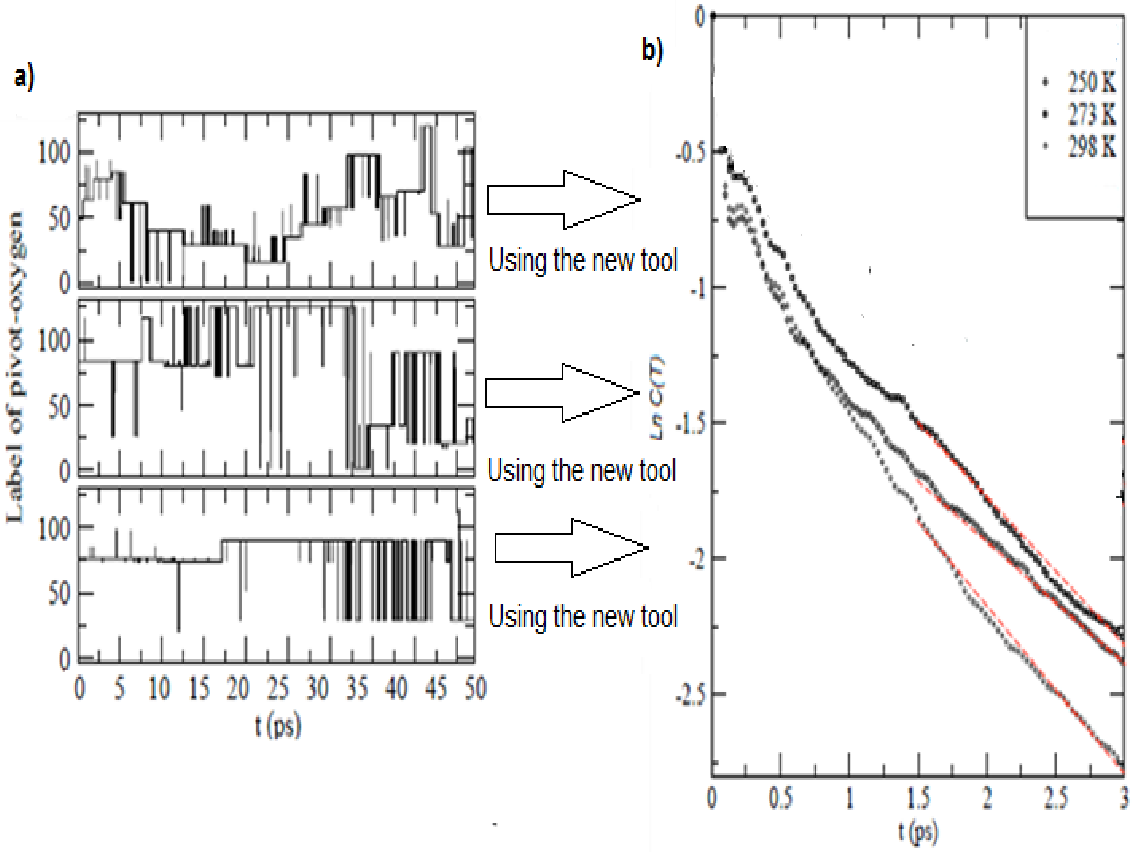

Figure 3.10: Logarithm of population relaxations of hydronium label (pivot) at different water states along T=250, 273, 300 K. ρ=1.0 gcm^{-3}; red dotted lines represented experimental tested data.

3.6 Results and discussion

Three layers ANN with a tangent sigmoid transfer function at hidden layer and one linear transfer function at output layer were used in the above case study to find the proton transfer rate. Eleven neurons were used in the hidden layer. Furthermore, this is not a fixed ANN structure and the tool will simply allow constructing any ANN structure from the main window following the variables of any other case study (e.g., 20 layers ANN with another activation function tansh…, etc).

3.6.1 Optimization of the ANN structure

The optimal architecture of the ANN pattern recognition model in addition to its parameter variation was determined based on the minimum value of the mean square error (MSE) of the training as well as prediction set. MSE was defined as $MSE = \frac{1}{N}\sum_{A=1}^{N} d_A^2 = \frac{1}{N}\sum_{A=1}^{N}(t_A - o_A)^2$. Where, MSE: mean square error; N: number of patterns; A: pattern index, t_A: Ath target value (experimental value), O_A: Ath output, d_A: different between t_A and O_A. Figure 3.11 illustrates the dependence between the neuron number at hidden layer and MSE for the MLP back propagation algorithm.

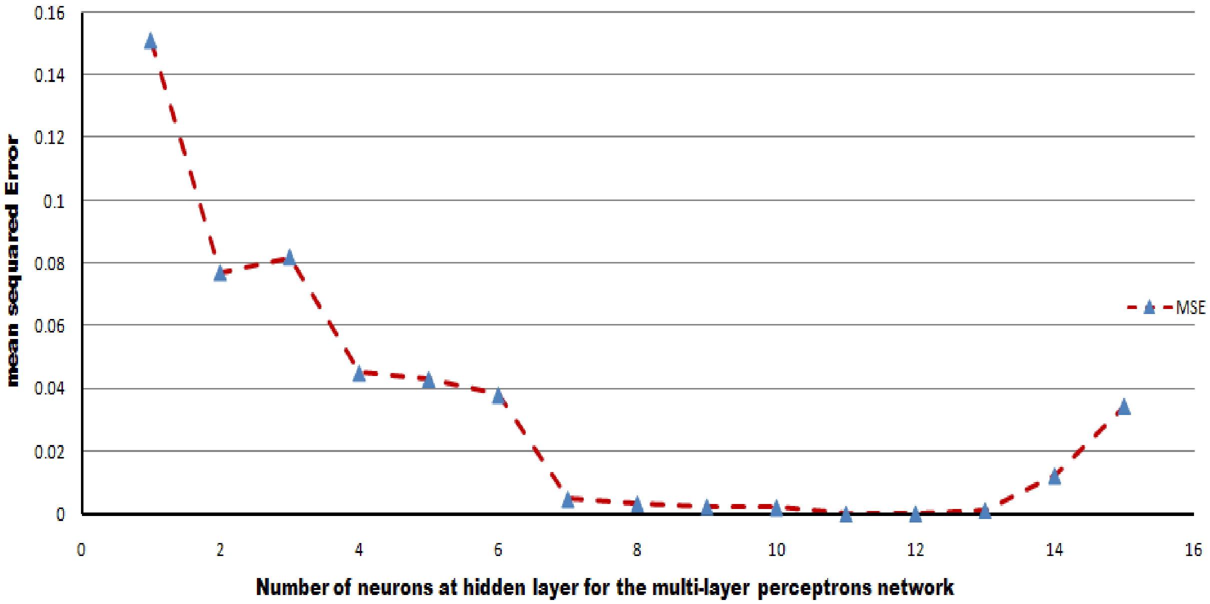

Figure 3.11: Dependence between MSE and number of neurons at hidden layer

As a result, with increasing the number of neurons, the network gave several local minimum values in addition to different MSE values that were obtained for the training set. One neuron was used as an initial guess in the hidden layer for optimizing the ANN network. The MSE of the network was much higher for the 1 (MSE 0.151) and 2 (MSE 0.077) hidden neurons than those with 3(MSE 0.082), 4 (MSE 0.045), 5 (MSE 0.043) and 6 (MSE0.038). With 7 hidden neurons, the MSE decreased significantly from 0.038 to 0.0048. With a further increasing in the number of neurons from 7 to 11a gradual decrease was observed in the MSE. The MSE reached its minimum value of (MSE 0.000117) with 11 hidden neurons. For this reason, the ANN network containing 11 hidden neurons (MSE 0.000117) was chosen as the best case. When the number of neurons exceeded 11, the MSE showed a slight increase from 0.000117 to 0.0012 at 13 neurons. A sharp increase in the MSE was resulted from a further increasing in the number of neurons from 13 to 15. This growth can be attributed to the characteristics of the MSE performance index and the input vector [A] used in this case study. Here, the initial weights had an important role on learning but unfortunately no one could estimate the proper initially weights set and each attempt were started the learning process again using different random initial weights. Finally when the differences between training error and validation error started to increase, training was stopped after iterations 1000 for the MLP network.

The flowchart of the MLP algorithm; together with this optimal 3 layers ANN network, were shown in figure 3.3 On the other hand a statistical analysis for estimating the relationships among input variables and network response between ANN graphical output of the network and the corresponding experimental data was performed as appeared in figure 3.10. The performance control of ANN graphical outputs was evaluated by estimating the correlation coefficient ($R2$) which was defined as: $R^2 = \frac{\sum_{A=1}^{N}(t_A - t_{mean})^2 - \sum_{A=1}^{N}(t_A - O_A)^{2}}{\sum_{A=1}^{N}(t_A - O_A)^2}$ where, R: correlation coefficient; N: number of patterns; A: index number of pattern; t_A: target value (experimental value); O_A: output of Ath pattern which proposed by ANN model. Therefore, test outputs showed a very small deviation in proton transfer rate values from the experimental data with an average value of about 0.12 (±0.19) where the proton transfer rates at three different temperatures was found to be 0.45, 0.47, 0.50 ps^{-1}, obtained from a window between 1000 and 2000 fs, for 250, 273 and 298 K respectively. Therefore it can be seen that the proposed ANN model shows a good performance on prediction of the experimental data based on R^2 values in table 3.2. These results showed a good agreement with previous studies [139].

3.6.2 Sensitivity analysis

In this work, a sensitivity analysis was conducted for determining the degree of effectiveness of a variable using the proposed ANN pattern recognition model. In this analysis, performance evaluations of various possible combinations of variables were investigated. Consequently, performance of the groups of (1, 2, 3, 4, 5) variables were tested here based on the optimal ANN structure by using the MLP with 11 hidden neurons. The groups of input vectors were defined in [A1, A 2, A3, A4, and A5] arrays, as shown in fig.3.3 and table.3.1. The groups were vary from groups of 1 to 5 variables with all expected combination probabilities , such as the one variables group (e.g., example, A1, A2, A3, A4, A5) ; groups of two variables, (e.g., A1+A2, A1+A3, A1+A4, A1+A5, A2+A3, A2+A4, A2+A5, A3+A4, A3+A5, A4+A5); group of three variables (e.g., A1+A2+A3, A1+A2+A4, A1+A2+A5, A1+A3+A4, A1+A4+A5,A2+A3+A4, A2+A3+A4, A2+A3+A4, A2+A3+A5, A2+A4+A5, A3+A4+A5), group of four variables (e.g., A1+A2+A3+A4, A1+A2+A3+A5, A1+A2+A4+A5, A1+A3+A4+A5, A2+A3+A4+A5), and finally the group of five variables(e.g., A1+A2+A3+A4+A5). Then best results of the performance evaluation of these 30 combinations are summarized in table .3.2

Combination	MSE	R^2	Iteration	Gradient	Best linear equation
A2	82.456	0.832	1000	2.923×10^{-9}	$Y = 0.69X + 23.6$
A2+A3	0.1174	0.858	800	3.122×10^{-14}	$Y = 0.79X + 9.3$
A1+A2+A3	0.05631	0.919	780	3.831×10^{-14}	$Y = 0.71X + 15.3$
A1+A2+A3+A5	0.02921	0.921	900	6.321×10^{-8}	$Y = 0.84X + 11.4$
A1+A2+A3+A4+A5	0.000011671	0.949	1000	0.398×10^{-10}	$Y = 0.97X + 7.8$

Table.3.2 Best group performance according to number of parameters: Gradient: is a formula used to update the search direction in internal parameter space. For more details see Ref. [145].

Performance evaluation of combinations of input variables showed a good agreement between ANN output and experimental data as a function of temperature [A2] when it comes to group of one variable that gives the lowest MSE. The temperature A2 and correlation function of pivot A3 was the best combination of two variables to affect the proton transfer rate computed value, it was very close to the experimental value with a minimum MSE in the group of two variables that was determined to be MSE=0.1174. As for the constant density it presented no effect in the results, in which predicting the proton transfer rate will not be possible based on water density a lone A4, but also it will have a clear effect in the group of 5 variables. The minimum MSE in the group of four variables (A1+A2+A3+A5) was determined to be 0.02921 with no effect of density A4. For 5 operating variables (A1+A2+A3+A4+A5) ,the proposed ANN pattern recognition model showed a precise and an effective prediction of the experimental data with a very satisfactory correlation coefficient of 0.949 with a very small MSR of 0.000011671. The sensitivity analysis showed that MSE values decreased as the number of variables used in the ANN model increased. The relative increases in the performance due to inclusions of A2 (temperature) were found to be larger than the contribution of others. For concluding, a simulation based on the ANN model can provide a further contribution to develop a better understanding of the dynamic behaviour of proton transfer process where still some phenomena cannot be explained in all detail but by some meaning the effect of these variables will explain the physical meaning of the phenomena. These results showed a good agreement with literature studies results such as [89,145]. Which confirm what already known about MLP networks behaviour, subsequently, this will confirm the fact that a pattern recognition problem of proton transfer could be well solved by using the feed-forward back-propagation neural network approach. In this regard, it is noteworthy to mention that this phenomenon had been the main topic of many previous studies based on developing such ANN applications [14,15,103], but each study has its particular objectives and it is targeting some specific chemical characteristics, usually others than those we have been adopted here (e.g., proton transfer rate) but all of these studies including the current study, agreed on the importance of the use the ANN neural network, in solving the problem of nonlinearity relationship between input variables and the required output. Therefore, the current proposed tool is expected to be used as a supplementary material in analyzing the proton transfer phenomena and would help researchers in making their decisions toward this phenomenon using the EVB simulation based on automatically charts fitting and drawing of the large output file in one workstation via a flexible GUI. Furthermore, any user can use this tool simply following its manual, without having to learn the theory or programming languages to start analyzing his data and reported the scientific findings.

3.7 Summary and Conclusions

An overview of theoretical background at the basis of the techniques we used to study the PT process in water has been given, with a detailed explanation of the state of art of the use of the ANN techniques in supporting the theoretical investigation of PT based on MD and Ms-EVB. The main structural, dynamical, and properties computed in this thesis from ensemble averages were also summarized. Herein we have adopted the evaluation of the use of AANs methodology in the classification of PT events and chart patterns, thus to facilitate the theoretical modeling process by using these simulation methods along with to overcoming their limitations and allowing statistical filtering of the data along with the predicting of the PT dynamics in aqueous environments and for finding PT chemical properties in aqueous environments. The second part of the chapter showed that how this study was successfully produced a flexible utility program to simplify the studying of proton transfer phenomena via using the EVB simulation based on ANN tool. The chapter presented the computational framework as a utility program consists of a flexible GUI in addition to a pattern recognition tool supported with easy to use data base system. The ANN tool could be run under several operating systems (Windows, UNIX, LINUX, MacIntosh) without the need if installing supplementary and computer configuration software’s. The tool can simplify plotting and re-sampling as well as data statistical fitting and mining based on the EVB output files and now it can be used as a supplementary tool for analyzing the proton transfer phenomenon in several aqueous environments and accessing to its deeper physical knowledge with predicting PT properties.

The new linked tool defined a chart pattern recognition tool as a deployed system for the classification of proton transfer data patterns as well as categorizing them into predefined set of classes based on the EVB generated output files to be trained and tested using the feed forward back propagation algorithm that would repeat the procedure of weight adjustments until the error would be reduced to the negligible amount to reach the error tolerance range. Therefore, using feedback information obtained from the difference between the actual and the desired result could increase the performance and the efficiency of the ANN network. This information would then be used for adjusting the interconnections between the neurons at the input layer for matching the actual result with the desired one. The ANN method substantially speeds up the MS-EVB PT structure calculations and has superior accuracy in mimicking the results of such calculations. Our ANN- EVB add on tool has simplify our PT analysis of the microscopic dynamics of liquid water and amorphous ices. Our analysis through the thesis were carried out by performing semi-classical molecular dynamics using the multistate empirical valence bond method, already largely applied to investigate PT process in water. The artificial neural network approach along with statistical methods is then employed for modelling as well as analyzing the PT properties we were interested in. So we can use it to present structural and dynamical properties of the solvated proton in confined and unconfined environment. This application has been tested for predicting chemical properties for future studies; in the meantime it could be used for data statistical fitting and pattern recognition based on separated simulations to facilitate analyzing the output data of the EVB simulation. Our results in turn proved to be fully compatible with previous proton transfer studies. We strongly recommend researchers in this field to make use of this simple and powerful ANN tool.

4 EVB-Molecular dynamics simulations

Despite being a ubiquitous element in the chemical physics of solutions, it was not until recently that the structure of aqueous protons was properly understood. This was largely the result of a series of computer simulation experiments that were able to reveal the structural characteristics of PT. Thus, there is a general consensus to describe the aqueous proton in terms of a “default” within the three-dimensional network of hydrogen bonds of water. Hence, dynamics of the proton is regulated by the control of the hydrogen-bond network. The temperature and, more specifically, the thermodynamical state of the system play a central role both on structure and location of the proton species and also on dynamics of the PT. Whereas plenty of information about PT in liquid water and in biomolecular systems at ambient conditions is available [146], its characteristics at low temperatures, such as in supercooled states, for the wide variety of ice classes and for high- and low-density amorphous ices is still largely unknown. Given the complexity of the phase diagram of water [147], studies of structure and dynamics of aqueous lone protons are usually reported for restricted regions of the diagram. For instance, proton arrangements in ice I were studied by means of dielectric relaxation and infrared spectroscopy and analyzed by Von Hippel [148].

Recently, a work based on multistate empirical valence bond calculations on PT in one-dimensional water chains confined in carbon nanotubes confirmed early results from Hummer et al. [149] and revealed that the rate of PT inside the tubes was one order of magnitude faster than in bulk [150]. On the other hand, *ab initio* molecular dynamics simulations of water inside nanotube channels [149, 151] have revealed different mobilities for hydroxide and hydronium ions inside the tubes, depending on the size of the tube and the degree of functionalization of the tube walls. A very recent work [152] reports proton transfer within graphene layers when surrounded by water. Protonated water clusters also provide very valuable information toward understanding proton and water properties at interfaces. First, characteristic signatures of Zundel and Eigen species have been revealed by photoevaporation of weakly bound argon in photofragmentation mass spectroscopy and compared to *ab initio* data at MP2 level [8, 9], with reasonably good agreement in most cases. Second, infrared spectroscopy of protonated benzene-water nanoclusters [153] indicated a local ordering of the first water shell around the proton induced by the interface. Very recently, Wang and Agmon [154] have analyzed the balance between dominant structures around the protonated water dimer in water-benzene mixtures, with a clear predominance of a so-called *crouching* Zundel isomer, symmetrically attached to a benzene ring.

The main purpose of this chapter is to report our results in comparison with those presented in the literature, based on analyzing the structure and dynamics of an excess proton in liquid water under two aqueous systems: (unconfined-bulk and confined-inside graphene slabs) following different geometries in the nanoscale along with wide range of temperatures ranging from ices to liquid water up to sub-critical high-temperature states analysis. Our results and discussions of PT will be reported in this chapter as summarized in table 4.1.

We employed MD simulations together with a multidimensional empirical valence bond procedure, in order to construct a suitable Hamiltonian for the semi-classical system; formed by a quantum particle (the lone proton) embedded in a sea of classical TIP3P waters. The artificial neural network approach along with statistical methods is then employed to work as supplementary computational tool to simplify modeling as well as analyzing the PT properties we are interested in. These PT properties will be shown in this chapter based on different chart patterns related to different physical cases with referring to the related fitting function as defined in Chapter 3.

Aqueous Systems	**Systems consists**	**Number**	**Proposed analyzing**	**Calculated quantities : Dynamical parameters for the aqueous protons**
Unconfined-Bulk 3D water	(1) a quantum particle (excess) proton)	1 H^+	Local structure of the excess proton and of solvating water molecules	The local pivot-water density profiles (3D). The oxygen pivot (O_z^*) z-position at different slab widths. $\rho_{O^*\alpha}(r)$; and C_i coefficients of equation (3.12).
Confined-inside graphene slabs-2D water	(2) a classical bath (liquid water or amorphous ice)	125 water molecules	Dynamics of proton transfer	**Proton Transition rate** τ^{-1} including *resonant* time τ_{rsn}, intermediate time τ_{prs} and *residence* time τ_{rsd}. **Proton diffusion** D_p. **Proton spectroscopy** $S_p(\omega)$ based on proton velocity $v_p(t)$.
Temperatures (K)	(100, 150, 200, 225, 250,273, 298, 400,500, 600).			
Graphene slabs width of (nm)	3.1, 2.7, 2.3, 1.9, 1.5, 1.1, 0.9, and 0.7.			
Simulation	In 3D: (1) constant density and volume, different T's; in 2D: (1) different slab widths at 300k, (2) different slab widths at different T's; in all cases simulation time is 100 ps. Hydrophobic walls: flat graphene slabs.			
Computing Tools	MD,MS-EVB,ANN			

Table 4.1: Summary of the results

In a first step, we will analyze the case of proton transfer in liquid water and low-density amorphous ices without confinement, to later move on to simulate the proton transfer in liquid water confined inside hydrophobic graphene slabs at the nanometric scale (with interplate distances between 3.1 and 0.7 nm wide). The analysis of the effects of confinement on proton solvation structure and on its dynamical properties has been considered for varying densities between 0.07 and 0.02 A^{-3}. The system is organized in one interfacial and a bulk-like region, both of variable size. A wide range of thermodynamic states, from low density amorphous ices (down to 100 K) to high temperature liquids under the critical point (up to 600 K) has been also considered. The chapter splits into two key sections. **Section (4.1)** reports the results of analyzing the local structure of the hydrated proton. On the other hand **section (4.2)** reports the results of analyzing proton transfer dynamics. Each section has its two main subsections based on the nature of the aqueous system followed by the chapter conclusion and remarks. Herein, our discussion in each section will start with the related investigations on unconfined water which is a first step into the study of PT in two-dimensional systems.

4.1 Local structure of the hydrated proton

4.1.1 Unconfined-Bulk water

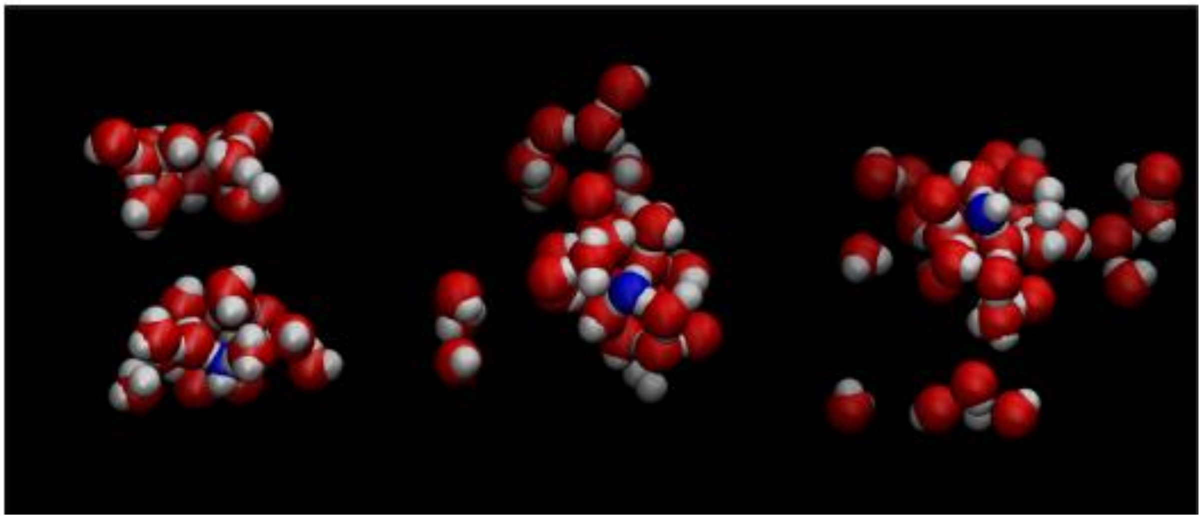

Figure 4.1: Snapshots of local configurations around the pivot water (oxygen in blue) at different thermodynamic states (left to right): T = 150, 225, and 298 K. Only water molecules having largest coefficients C_i (typically 20–30 molecules) are explicitly shown.

In order to initially understand the solvation structure of proton, we introduce snapshots of the local water structure at several different temperatures as shown above in figure 4.1.

There we have only included, for the sake of clarity, those molecules having the largest weighting coefficients C_i from equation (3.12) (of the order of 20 molecules), which usually are the water molecules of the first and second solvation shells of the instantaneous hydronium species. From this picture we can have a first direct indication of the fact that the local environment of the proton (first water shell) is essentially the same in all cases, namely a three coordinated Eigen cation, although the general structure of the local cluster may be quite different for the three temperatures considered. We observe, for instance, that as temperature decreases the local environment of the proton becomes more localized, with a closer first solvation shell. We will analyze microscopic details of solvation by considering the local pivot-water density fields $\rho_{O^*\alpha}(r)$. Spatial correlations of oxygen pivot-oxygen water sites are shown in top panel at left side of figure 4.2.

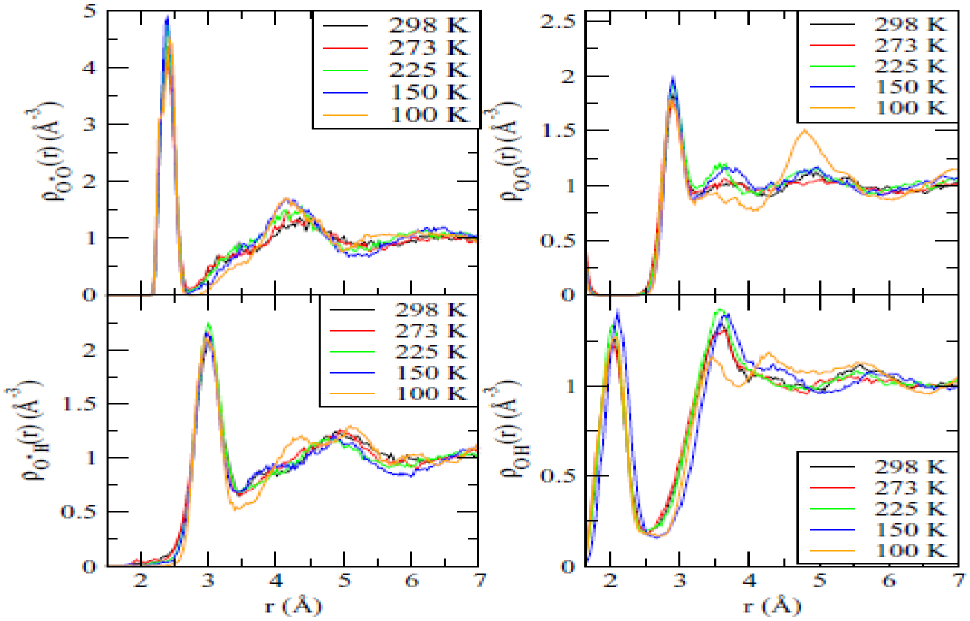

Figure 4.2: Oxygen pivot (O*)-oxygen solvent (O) site-site pair correlation functions at different thermodynamic states (top left). Oxygen pivot (O*)-hydrogen solvent (H) (bottom left). Oxygen-oxygen pair correlation functions (top right), oxygen hydrogen pair correlation functions (bottom right).

Interestingly, structures of the pivot-oxygen profiles are dominated by a first solvation shell located at $r = 2.5\overset{\circ}{\mathrm{A}}$, including three or four acceptor water molecules, being essentially the same at all temperatures. Those similar local structures reveal that the proton is able to promote a considerable extent of solvent clustering in its close vicinity at low temperatures in ice ambients in a close fashion to what is seen at ambient conditions.

Moreover, the presence of a second shell located at $\approx \mathrm{r} = 4.5\overset{\circ}{\mathrm{A}}$ is also clearly perceptible in all thermodynamic states investigated. These molecules correspond to the second solvation shell of the hydronium, and some of them may act as hydrogen bond acceptors or donors with respect to the inner ones. As temperature decreases, the position of such second shell waters tends to move at lower distances, from $\approx 4.6\overset{\circ}{\mathrm{A}}$ at 298 K to $\approx 4.2\overset{\circ}{\mathrm{A}}$ at 100 K. The local cluster tends to become smaller as temperature goes down. This promotes a larger extent of water localization in a similar fashion as it happens in cubic ice [80, 81], since packing and ordering is common for solid-like states, instead of the typical tendency to disorder of liquid-like states.

The analysis of the oxygen pivot-hydrogen water profiles is shown at the bottom panel at left side of figure 4.2 and it provides complementary information. Here, in all cases, we found main peaks located at $\mathrm{r} = 3.15\overset{\circ}{\mathrm{A}}$. At low temperatures, these peaks include exclusively the six hydrogen atoms corresponding to the water molecules belonging to the first solvation shell; as temperature increases the number of hydrogen atoms included in the first peak raises to ≈ 9. An analysis of the connectivity of these new hydrogen atoms reveals that, typically, two of them belong to molecules from the second shell acting as hydrogen bond donors to the inner ones. At 100 K, we observe how the structure of water hydrogens around the pivot oxygen enhances and reveals three maxima at $\approx 4.3, 5.2$, and $6\overset{\circ}{\mathrm{A}}$ suggesting a tendency of the system to evolve towards a more ordered solid-like configuration. We finally remark that, regardless the temperature investigated, we found no evidences of pivot acceptor hydrogen bonding of the type O–H· · · O. As we will discuss in the following sections, these observations concerning the hydrogen bond connectivity may have relevance in determining the mechanisms that drive the transfer of the proton.

At the right column of figure 4.2 we displayed the oxygen-oxygen $\rho_{O-O}(r)$ and oxygen-hydrogen $\rho_{O-H}(r)$ radial density fields. The locations of the main peaks are in overall good agreement with the findings of Botti *et al.* [155] (Figure 4.2) obtained from neutron diffraction experiments of HCl dissolved in water, which indicates that the local water ordering due to the presence of the lone proton is not qualitatively different of that produced by protons of strong acids like HCl, where Zundel and Eigen structures solvating a lone proton in water survive to the influence of large anions such as chlorine [156].Interestingly, up to three-four water layers can be observed in the O-O and O-H profiles for temperatures corresponding to LDA ices, which indicates that in such systems solid-like structures tend to appear.

4.1.2 Water Confined-inside graphene slabs

4.1.2.1 The effects of confinement on the local structure of the hydrated proton

We report snapshots of the local proton structure for three different widths of the slab (*d* = 3.1, 1.5, and 0.7 nm) in Fig. 4.3. As we did above we just included, for the sake of clarity, those molecules having the largest weighting coefficients C_i from Eq. (3.12) (22 molecules for *d* = 3.1 nm, 14 for *d* = 1.5 nm, and 8 for *d* = 0.7 nm), which are molecules belonging to the first and second solvation shells of the instantaneous hydronium ("pivot") species. Visual inspection gives a first direct indication on how the local environment of the proton is organized.

So, at large interplate distances the proton is found at the central part of the system, with the number of diabatic states being quite large, very similar to the case of the unconstrained solvated proton [2] as explained in section 4.1.1. As the graphene plates are placed closer, the number of diabatic states decreases and the number of water layers potentially involved in PT drops to two (*d* = 1.5 nm) and to roughly one (*d* = 0.7 nm). The lone proton shows a clear tendency to stay close to the interface, as we will point out with more detail below. In summary, the general structure of the local cluster is dramatically affected by the presence of the graphene plates, which force the system to become quasi-two-dimensional.

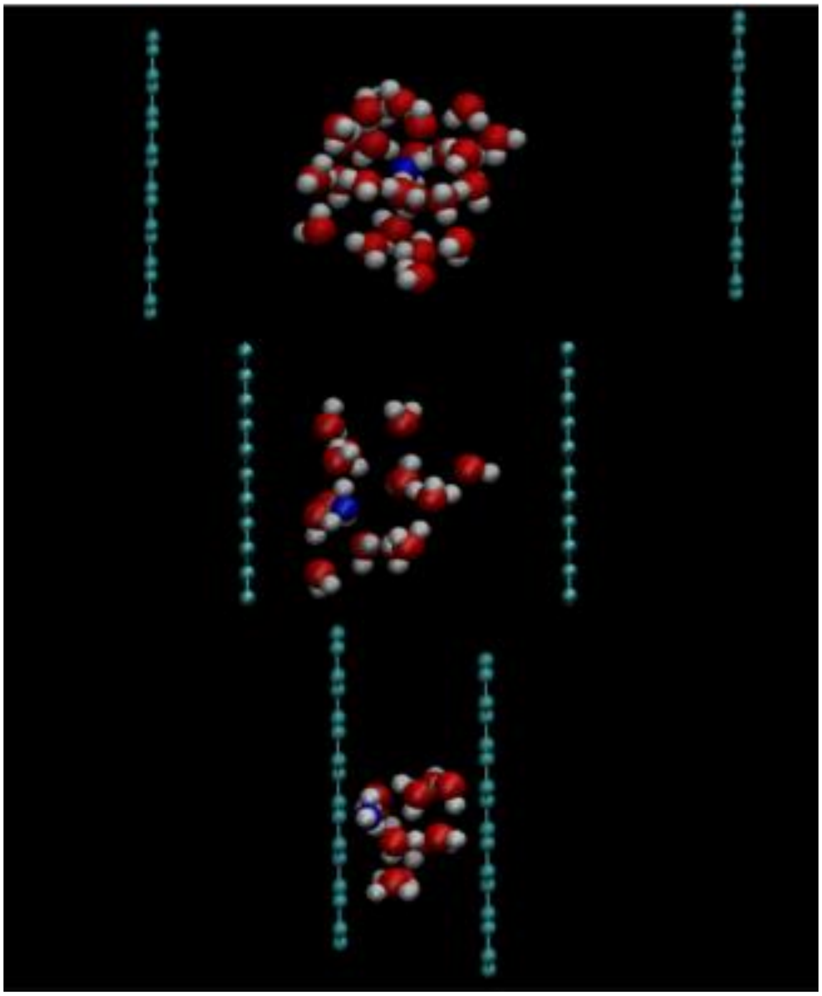

Figure 4.3: Snapshots of local configurations around the pivot water at different slab widths (top to bottom): *d* = 3.1, 1.5, and 0.7 nm. Only water molecules having largest coefficients *Ci* (typically 20–30 molecules) are explicitly shown. Carbon atoms (cyan), oxygens (red), hydrogens (white), oxygen (blue).

To evaluate the location and mobility of the proton species, we computed oxygen pivot (O*) *z* position at different slab widths, between *d* = 3.1 and 0.7 nm, for a time interval of 50 ps. The results are reported in figure 4.4.

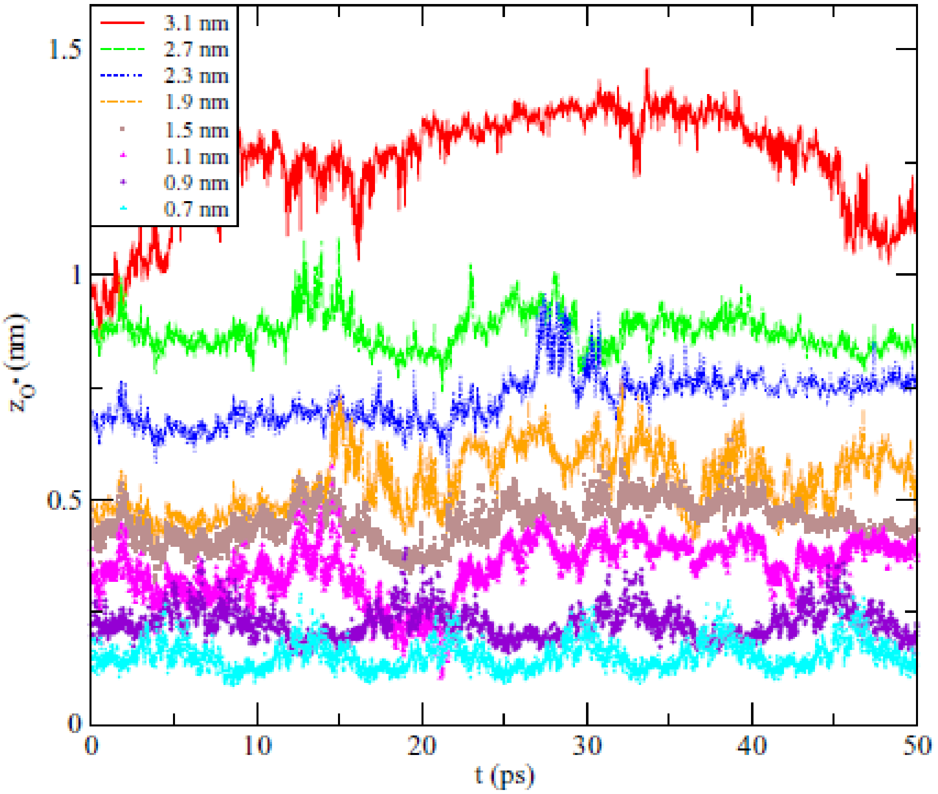

Figure 4.4: Oxygen pivot (O^*) z position at different slab widths, between d = 3.1 and 0.7 nm. Here $z_0^* = 0$ corresponds to the center of the slab. d =3.1 nm (full red line); d =2.7 nm (dashedgreen line); d = 2.3 nm (dotted blue line); d = 1.9 nm (dot-dashed orange line); d = 1.5 nm (brown squares); d = 1.1 nm (magenta triangles); d = 0.9 nm (violet diamonds); d = 0.7 nm (cyan stars).

There we observe that in the equilibrated system the lone proton shows a tendency to be transferred in a set of z values ranging from 0.85 to 1.5 nm for the widest slab (d = 3.1 nm) to values fluctuating around 0.2 nm for the narrowest case (d = 0.7 nm), where resonant episodes (see below) are hinted. This indicates the tendency of water to mainly diffuse along the *XY* plane, when constrained inside a narrow slab. This was already observed for pure water (with no presence of an excess proton) close to a graphene wall [157]. For systems including a lone proton close to hydrophobic interfaces, lateral diffusion of the proton has been observed in membranes made by *n*-decane molecules [158] together with the well-known high affinity of the proton for the membrane water interface and also high proton mobility.

Oxygen pivot-oxygen water density profiles are shown in the top-left panel in figure 4.5. In all cases, the first solvation shell of the proton is centered at $r = 2.4\,\mathring{A}$. This value was already found for unconstrained water at low temperatures in section (4.1.1) [2]. From this information we can observe that the solvent clustering promoted by the proton is strong enough to be barely affected by confinement. In other words, the dynamical equilibrium between Zundel dimer and Eigen cation structures will likely remain in confinement up to a large extent. However, for graphene-graphene distances $d \leq 1.1$ nm the height of the first maxima is reduced. About the second shell around the proton, its center is located at shorter distances as *d* decreases (about 4 $\mathring{A}$ instead of 4.5 $\mathring{A}$ for the unconstrained case). At shortest distances such as *d* = 0.9 and 0.7 nm marked oscillations of the second shell maxima are seen. This indicates that local clusters tend to become smaller as the two graphene plates become closer. This promotes a larger extent of proton localization in a similar fashion as when proton is at the air-water interface [159]. The analysis of the oxygen pivot-hydrogen water profiles is shown at the bottom panel at the left-hand side of figure 4.5 and it provides complementary information. Here we found main peaks located at $r = 3\,\mathring{A}$ (first) and $r = 5\,\mathring{A}$ (second) for the unconstrained system, which are reproduced when the interplate distances are over 1.1 nm. The values are in overall agreement with diffraction data obtained by Soper and coworkers [155] for a concentrated HCl aqueous solution. When *d* = 1.1 nm is reached, the position of the second maximum tends to shift backwards, up to be located around 4.75 $\mathring{A}$ for the case of *d* = 0.7 nm, favoring higher proton localization. At large slab widths these peaks include exclusively the six hydrogen atoms corresponding the water molecules belonging to the first solvation shell; as width decreases the number of hydrogen atoms included in the second shell tends to be significantly smaller as indicated by short second-shell peaks and, especially, by the clear tendency of the first minimum to disappear. This suggests the gradual destruction of the HB network connecting the first and second coordination shells of the lone proton as the interplate distance decreases. The density profiles of oxygen-oxygen $\rho_{O-O}(r)$ and oxygen-hydrogen $\rho_{O-H}(r)$ (right-hand side of figure 4.5) concern the HB connectivity and will have relevance on the mechanisms that drive the transfer of the proton. At the first sight, we can distinguish interfacial and bulk-like regions. The latter becomes highly fluctuating at low interplate separations (0.7 and 1.1 nm). The locations of the main peaks are in overall good agreement with the findings of Botti *et al.* [155] for the unconstrained case. As the interplate distance is reduced, maxima corresponding to the second peaks tend to mess up and move to intermediate values, suggesting that as the system is compressed along the *Z* axis it gradually becomes a quasi-two-dimensional water layer. As described in Ref. [160], the HB network is distorted and eventually broken, at least partially.

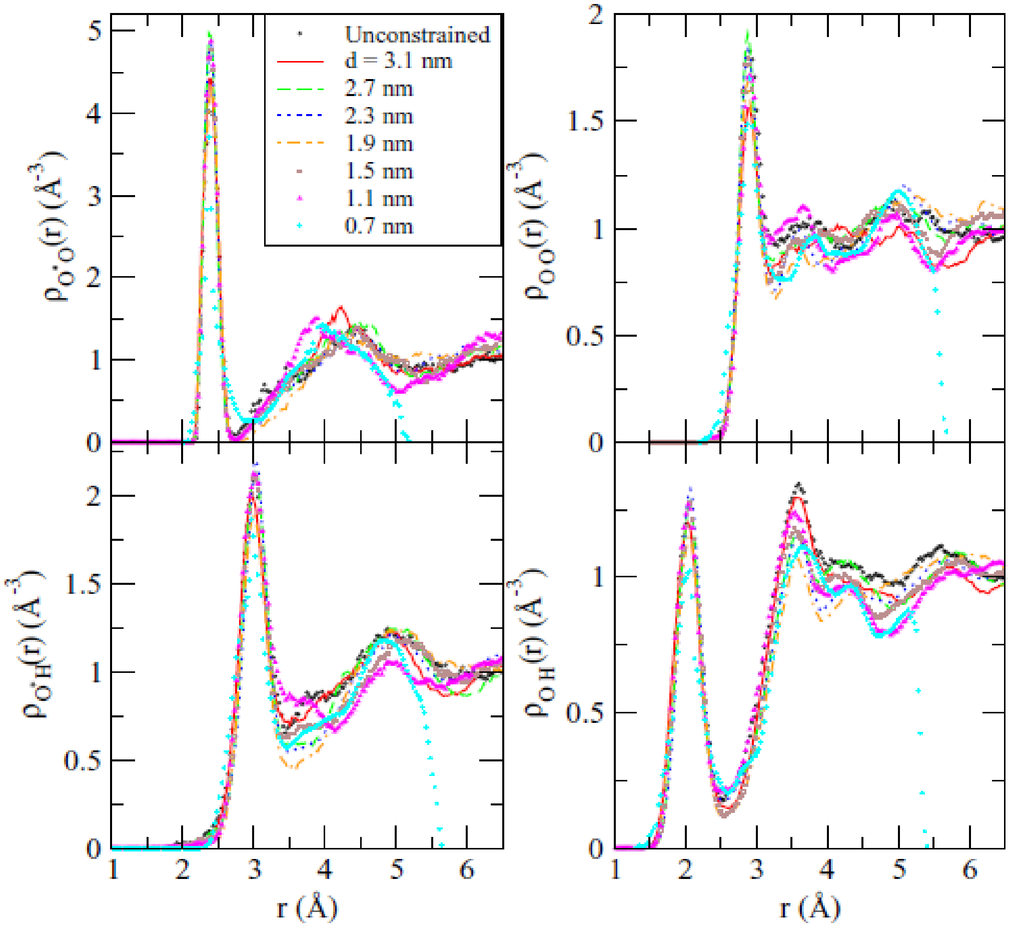

Figure 4.5: Oxygen pivot (O*)-oxygen solvent (O) site-site pair correlation functions at different states (top left). Oxygen pivot (O*)-hydrogen solvent (H) (bottom left). Oxygen-oxygen pair correlation functions (top right), Oxygen-hydrogen pair correlation functions (bottom right). Unconstrained water (black circles); *d* = 3.1 nm (full red line); *d* = 2.7 nm (dashed green line); *d* = 2.3 nm (dotted blue line); *d* = 1.9 nm (dot-dashed orange line); *d* = 1.5 nm (brown squares); *d* = 1.1 nm (magenta triangles); *d* = 0.7 nm (cyan stars).

4.1.2.2 The effects of temperature and confinement on the local structure of the hydrated proton

To provide a visual perspective of the local structure of the protonated water, we report selected snapshots of molecules around the lone proton as shown in figure 4.6 having the largest weighting coefficients C_i of equation (3.12) (of the order of 15-25 molecules) for the intermediate distance d = 1.5 nm at temperatures of 100, 300 and 500 K. From this picture we can observe that the proton together with its local environment (first water shell) mostly consist of a three coordinated Eigen cation, which keeps the proton separated from the graphene layers. We couldn't find any configuration where the hydronium was in direct contact with the surface. Conversely, for the closest d = 0.7 nm case, some configurations of the proton show it in direct interaction with the carbon walls, where as for the d = 3.1 nm case, the local structure is more populated and the proton tends to be around the central part of the system (see figure 4.3).

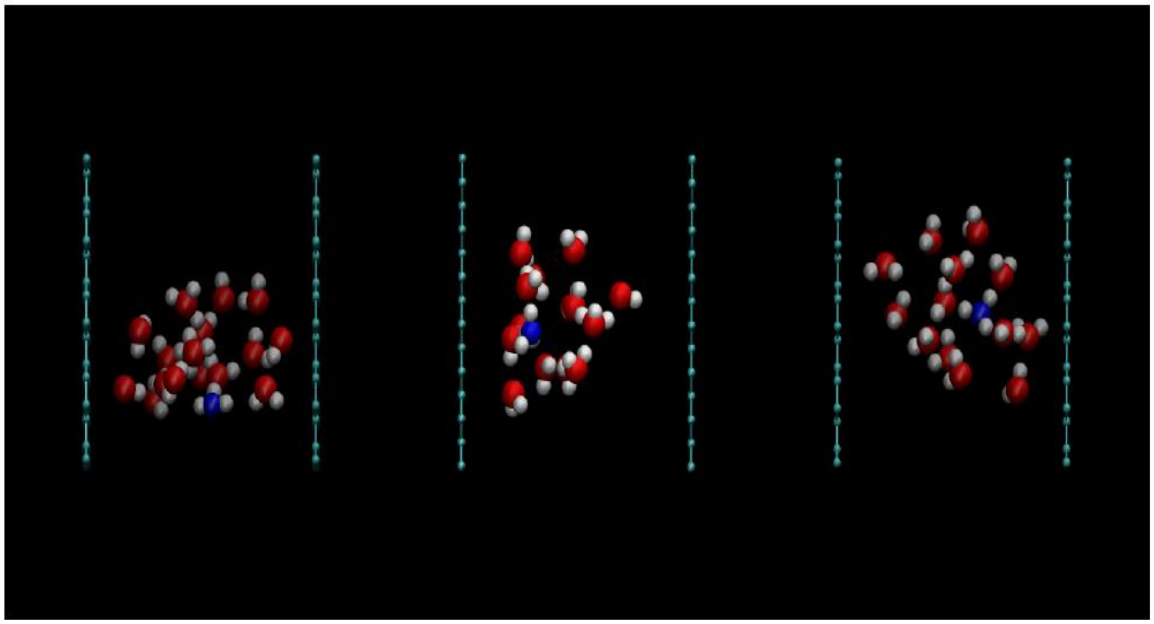

Figure 4.6: Snapshots of local configurations around the pivot water confined inside the graphene slab 1.5 nm wide at different thermodynamic states (left to right): T = 100, 300 and 500 K. Only water molecules having largest coefficients C_i (usually 15-25 molecules) have been shown.

On the other hand figure 4.7 presents the density profiles of oxygen-oxygen $\rho_{O*-O}(r)$ (in the left side panels) and pivot oxygen-hydrogen $\rho_{O*-H}(r)$ (the right side panels).

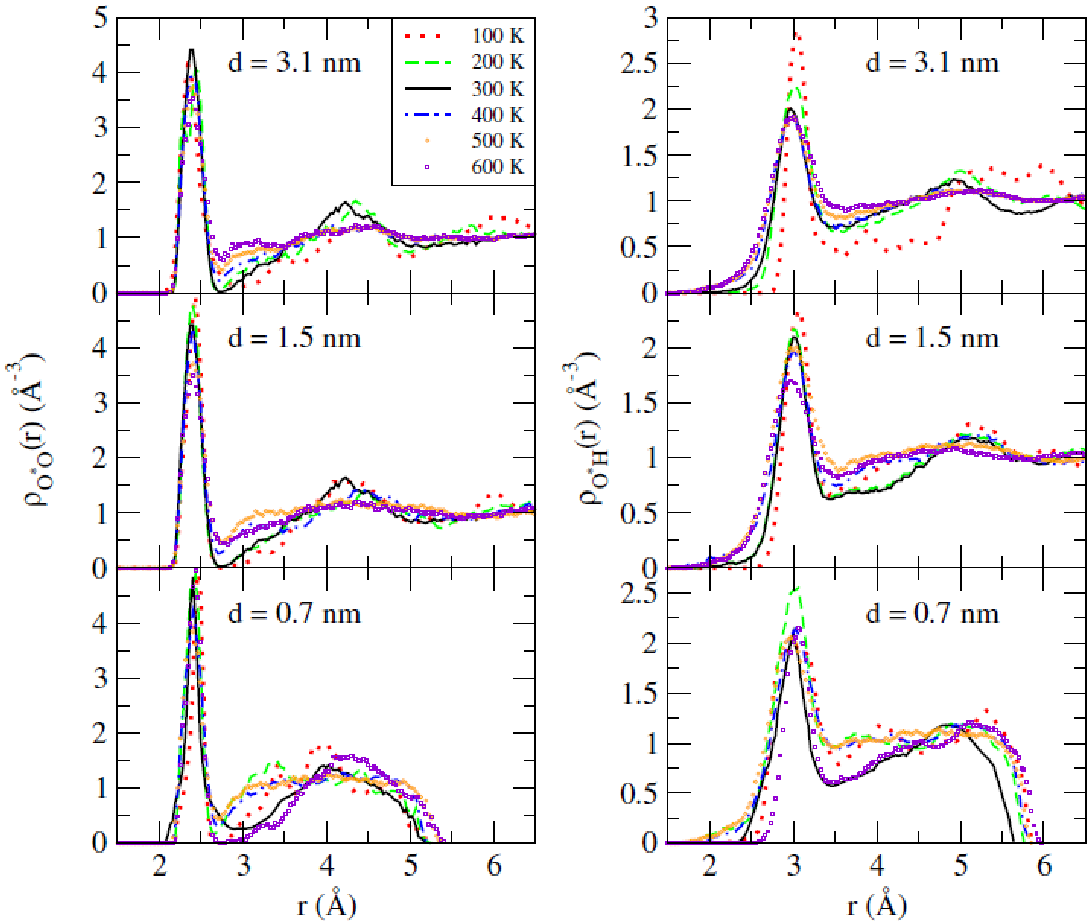

Figure 4.7: Pivot oxygen-solvent oxygen density felds (left side) and pivot oxygen-solvent hydrogen density fields (right side) at different thermodynamic states. Interplate separations: d = 3.1 nm (top figures); d = 1.5 nm (middle figures) and d = 0.7 nm (bottom figures).

From the former we can distinguish a marked first solvation shell centered around $r = 2.4$ Å for all interplate distances with a slight tendency to increase localization as d decreases. The location of this maximum is in good agreement with the findings of Bankura and Chandra [66]. This fact indicates that the proton is able to promote a remarkable extent of solvent clustering in its close vicinity, regardless of the temperature considered, from ice-like ambients to high sub-critical temperatures, in a close fashion to what is seen at ambient conditions for the unconstrained case (see section 4.1.1). A second solvation shell located at $\approx \mathrm{r} = 4.25\ \mathring{\mathrm{A}}$ at ambient conditions for the widest graphene channels (d = 3.1; 1.5 nm) can be also observed for the low temperatures but it quickly disappears above 300 K. This is consistent with the picture of the lone proton loosing most of its hydrogen-bond connections to waters potentially participating of a second coordination shell. In the particular case of d = 0.7 nm, the distance between the two plates is so short that there is only room available for two water layers, eventually distorted from planar configurations. Such strong confinement effect of the graphene plates produces some reduction in size of the water second coordination shell at all temperatures, eventually shifting towards lower distances, centered around $\approx \mathrm{r} = 3.8 - 4\ \mathring{\mathrm{A}}$. This indicates that the local cluster around hydronium tends to become smaller as confinement becomes more important. This larger extent of water localization is similar to the case of cubic ice and of unconstrained amorphous ice (section 4.1.1).

Analysis of the oxygen pivot-hydrogen water density profiles is based on $\rho_{O*H}(r)$ at the right side of figure 4.7. Here, in all cases; we found main peaks located around $\mathrm{r} = 3\ \mathring{\mathrm{A}}$, in a close fashion as it was recently reported from ab-initio and quantum-classical simulations [66]. As a general trend the height of this peak diminishes as temperature increases. At the lowest temperature such peak includes exclusively the six hydrogen atoms contained in the first solvation shell of the hydronium. As temperature increases the width of this band becomes larger (the first minimum shifts by $\mathrm{r} = 0.25\ \mathring{\mathrm{A}}$ and the averaged number of hydrogen atoms indicated by coordination numbers raises to $\approx 9-10$. At 100 K the structure of water hydrogens around the pivot oxygen enhances, suggesting a tendency of the system to evolve towards a solid-like configuration for all considered interplate distances. Finally, we didn't find any evidence of pivot acceptor hydrogen bonding of the type $\mathrm{O}-\mathrm{H}...\mathrm{O}$, formed by means of the lone sp3 orbital of the acceptor oxygen, in the usual way of most of studies of confined water.

4.2 Proton transfer dynamics

4.2.1 Unconfined-Bulk water

4.2.1.1 Population relaxations and proton transfer rate

We will start analyzing the nature of the proton transfer dynamics in liquid water and ices by direct inspection of the time evolution of the pivot oxygen label during 50 ps time intervals, as shown in figure 4.8. Seven representative temperatures (100, 125, 150, 225, 250, 273, and 298 K) are shown, but the effect of temperature on the frequency of proton transfer episodes is directly seen, by simply counting the number of transitions in the four plots: At T = 298 K (bottom panel), approximately $\approx 20 - 25$ water molecules retain the pivot label during time intervals of the order of 0.5 ps or longer, roughly delivering a transfer time of 0.4–0.5 ps^{-1}. That number is at least fivefold smaller as we move to ice-like temperatures, keeping the density constant. A few PT can be still seen at 150 K and even one of them has been captured at 100 K (given the short time interval considered here). We should point out that the predicted rate of transfer at ambient conditions is a factor ≈ 8 larger than the one inferred from results of NMR experiments [161–162], being that this a well-known deficiency of the semi-classical picture adopted here; moreover, the explicit incorporation of quantum fluctuations in the transferring proton yields a better agreement with the experiments, leading to rates at least twice as large as the semi-classical ones [74].The overall jump patterns look quite similar in all thermodynamic states and can be regarded as a sequence of episodes in which the proton resides in one water during a few ps, interrupted by intervals in which the proton resonates rapidly between two valence bond states, establishing what is usually called a “special” bond [75]. Some few isolated spikes reveal single attempts of aborted transitions in all cases. The crude picture provided above may be substantially improved using fitting functions from our ANN application. To do this, we will need that in all cases proton transfers were sufficiently frequent to collect statistics without employing special techniques designed to analyze rare events dynamics, such as transition path sampling or other importance sampling schemes [125]. Results for the population relaxation of the pivot label are shown in figure 4.9.

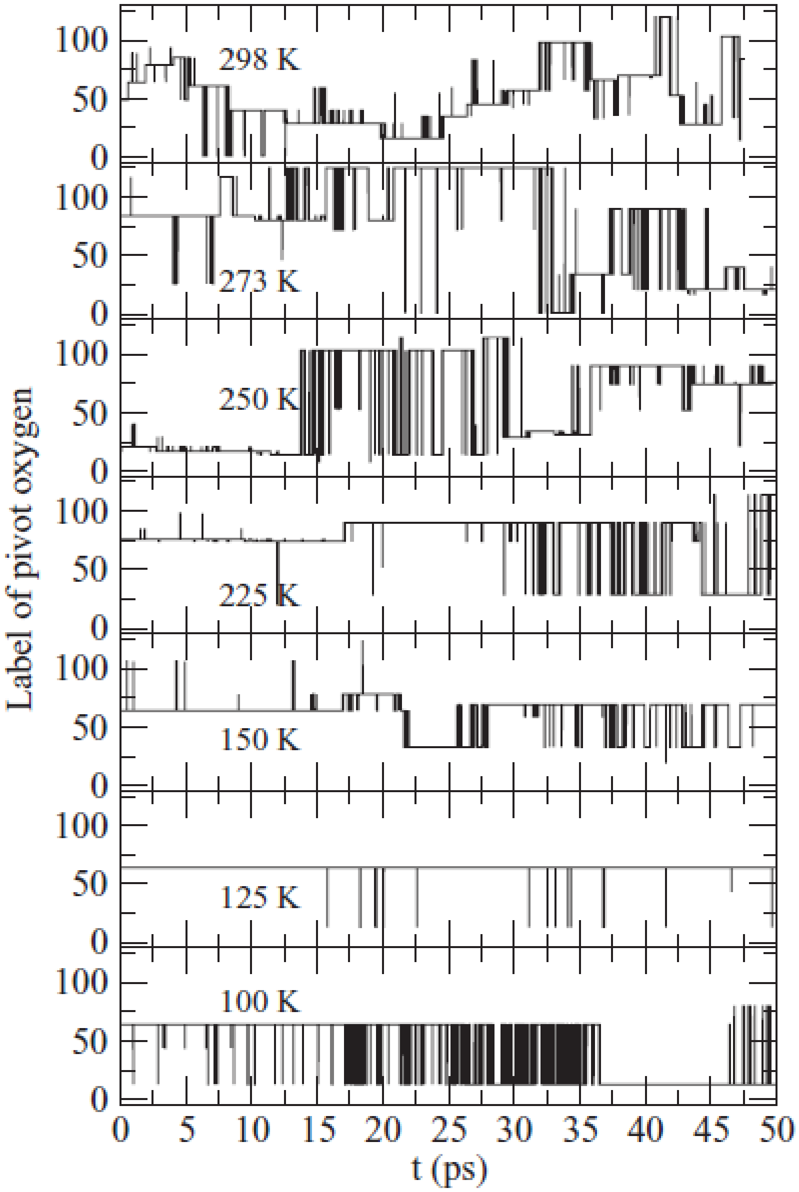

Figure 4.8: Time evolution of pivot-oxygen labeling in different aqueous environments; from liquid to LDA ice systems (top to bottom).

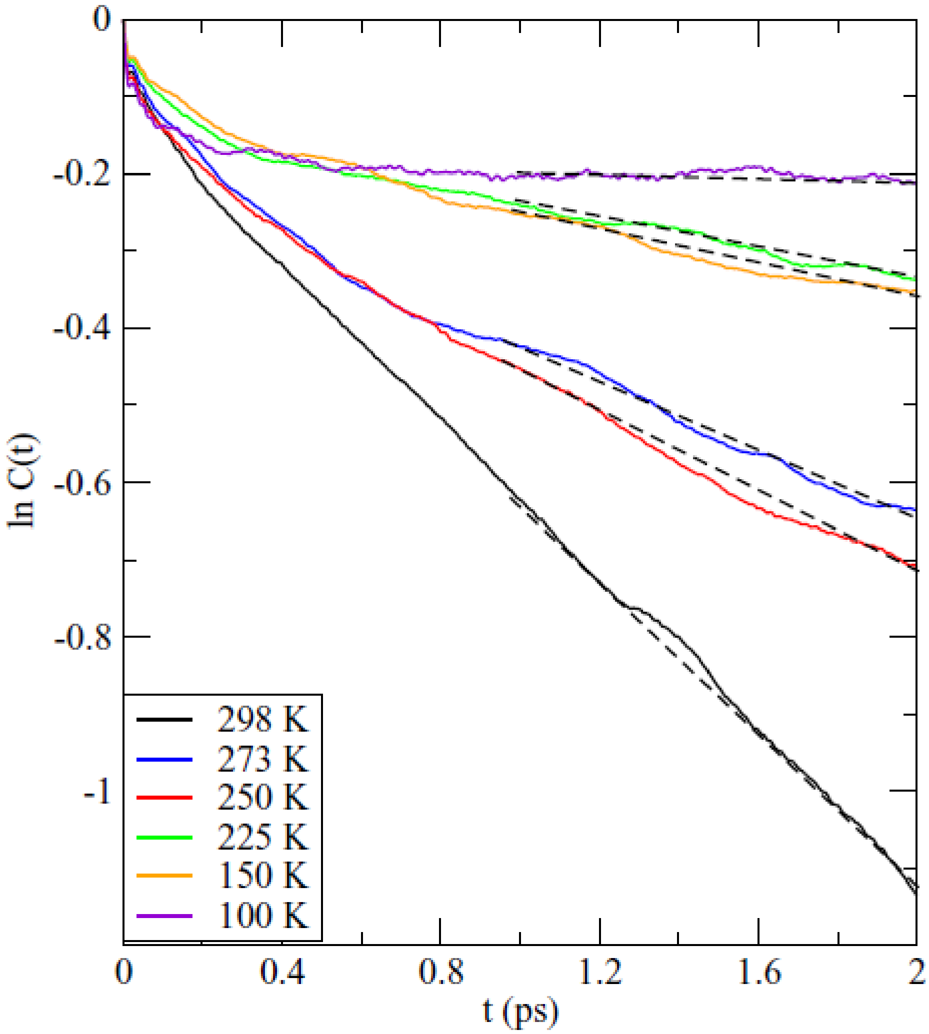

Figure 4.9: Logarithm of the population relaxations for the pivot-oxygen label at different thermo dynamical states. Linear fits between 1–2 ps are represented by dashed lines.

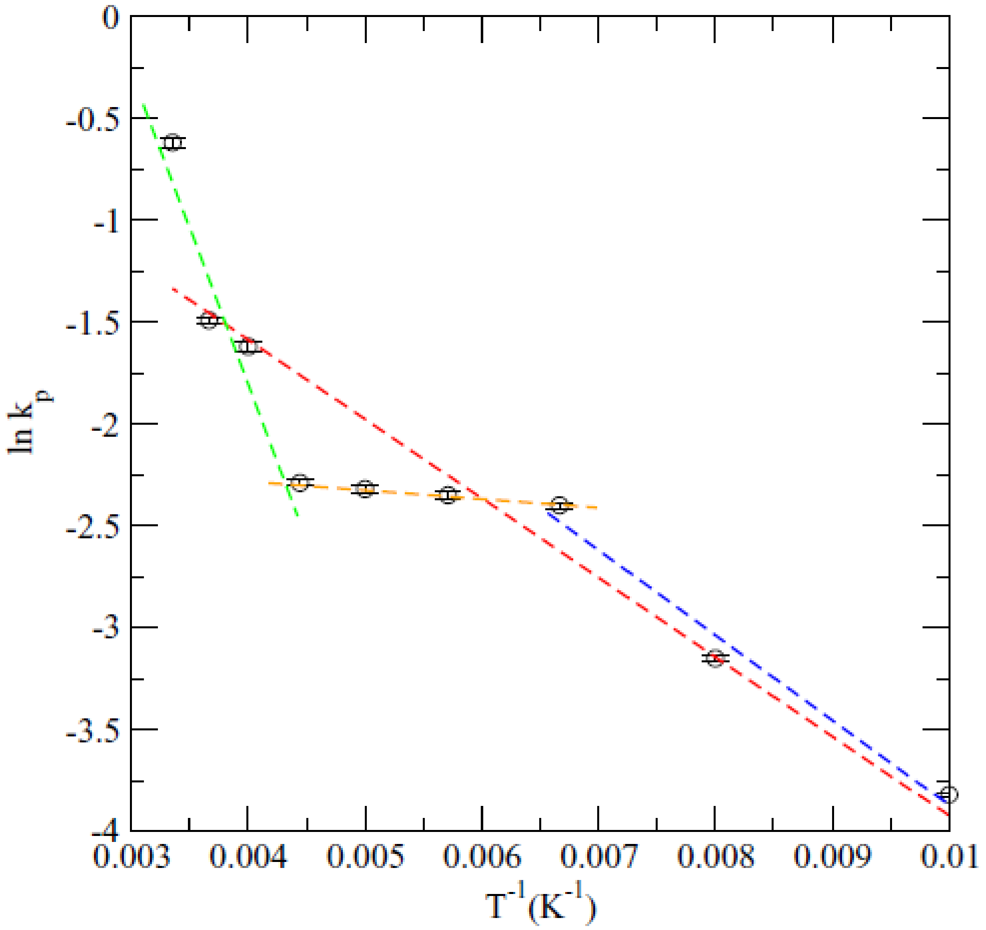

Figure 4.10: Logarithm of proton transfer rates *kp* as a function of inverse temperatures. Straight lines represent the best linear fits for different temperature ranges: overall (red line); between 298 and 225 K (green line); between 225 and 175 K (orange line); and between 175 and 100 K (blue line). The results for the thermo dynamical states considered in this case are reported in Table 4.2.

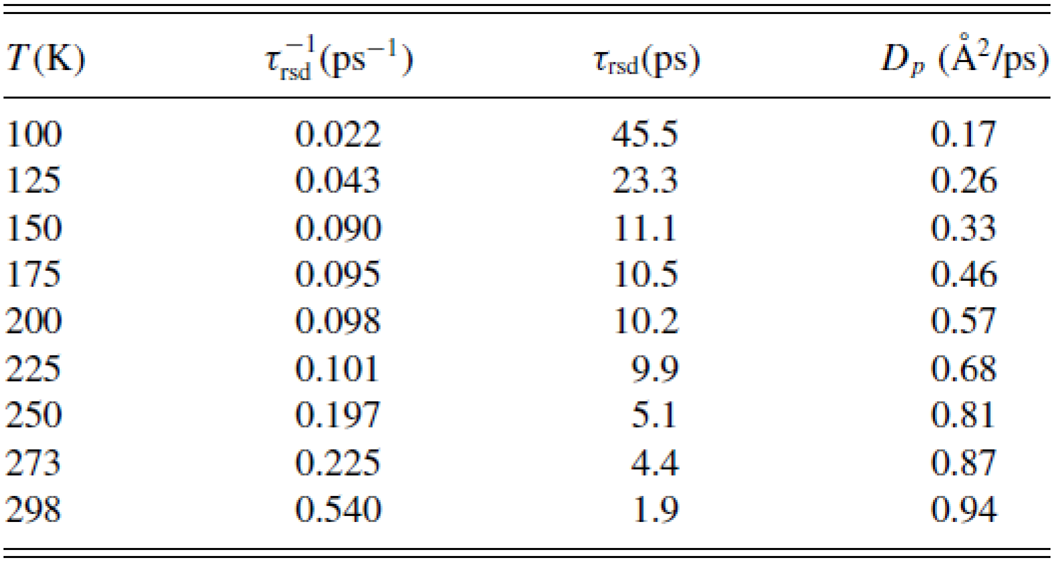

T(K)	τ_{rsd}^{-1}(ps^{-1})	τ_{rsd}(ps)	D_p (Å^2/ps)
100	0.022	45.5	0.17
125	0.043	23.3	0.26
150	0.090	11.1	0.33
175	0.095	10.5	0.46
200	0.098	10.2	0.57
225	0.101	9.9	0.68
250	0.197	5.1	0.81
273	0.225	4.4	0.87
298	0.540	1.9	0.94

Table 4.2: Dynamical parameters for the aqueous protons at different thermodynamic states: proton transfer rates τ_{rsd}^{-1}, residence time τ_{rsd}, and diffusion coefficient of the lone proton D_ρ.

The general trend is a systematic slowdown of proton dynamics when the system is cooled down to LDA ice states: proton transfer rates decrease and, equivalently, the estimated residence time's τ_{rsd} increase. The comparison to other simulation works reveals a good overall agreement with findings from Day *et al.* [67], who obtained a value for the proton transfer rate of 0.3 ps^{-1} at room temperature (300 K), for an EVB model different of the one used in the present work. In the case of cubic ice, it was observed [80, 81] that the ratio between PT rates of liquid and ice phases is about a factor 2. This fact was attributed to the larger extent of localization and alignment of the $O-O*$ pairs, which would be at the basis of the PT mechanism in ices. In our case, when cooling down the system PT rates tend to decrease, following a monotonic behavior and showing a tendency to satisfy an Arrhenius-like dependence (see figure 4.10) with some clear deviations. Hence, assuming the following dependence of the proton transfer rate with temperature:

$$k_p \approx Ae^{-\frac{E_k}{K_B T}} \tag{4.1}$$

Where A is a proportional factor and k_B is Boltzmann's constant, we can obtain an estimation of the PT activation energy E_k. Given the slope of the straight line shown in the Arrhenius plot of Fig. 4.10 (red line), we get a value of E_k = 3.2 kJ/mol for the overall linear fit to the whole set of values. This is in qualitative good agreement (order of magnitude) with the 10 kJ/mol obtained by Moon *et al.* [163,164] by means of a reactive ion scattering technique for the activation energy of PT at the surface of polycrystalline ice film, prepared at 135 K. Therefore, PT is an activated process at low temperatures and it requires surmounting an energy barrier of quite important magnitude. When the process of PT is mediated by hydroxide ions, the energy barrier has been measured at 9.6 kJ/mol [83]. It should be noted that at the different subintervals of temperatures (between 298 and 250 K, from 225 up to 175 K and from 175 to 100 K) different slopes can be obtained, revealing different behavior when the system is at liquid phase, which undergoes the phase transition from liquid to LDA ice and at the LDA ice phase (in all cases at temperature ranges different from experimental data, because of the present water model). A fine tuning of the slopes is also shown at each range. At the liquid phase (green line), we get an estimated activation energy of 12.8 kJ/mol, at the interval between 225 and 175 K the value is just of 0.6 kJ/mol and at the LDA ice phase, we get about 3.4 kJ/mol. We should note that Luz and Meiboom [165] obtained10 kJ/mol for the activation energy of PT in pure water between 288 and 348 K from proton magnetic relaxation measurements, in excellent agreement with the 12.8 kJ/mol reported here in the range of 250–298 K.

In conclusion, the largest energy barrier to surmount for the proton corresponds to the liquid phase and the lowest to the range 225 to 175 K. This suggests that the slowdown of PT at low temperatures is mainly due to the lack of thermal energy, since the energy barriers are lower than at high temperatures, probably due to the higher degree of localization of the proton, as we can note from figure 4.3, where LDA ice has a local structure richer than that of water at ambient conditions, with 2–3 water layers clearly distinguishable.

Some years ago [26], the existence of a direct relationship between the likeliness of PT and the distance between oxygens of solvating water molecules was suggested. At small distances, if the lone proton is equally shared by two waters (Zundel dimer) it corresponds to a minimum in the external potential of the proton along the O-O axis.

However, if the proton is closer to one of the waters, the potential shows a maximum. Nevertheless, it was indicated [26] that the correct picture should be given by a two dimensional potential depending on at least two variables: R_{O-O} and the proton displacement coordinate. Indeed the consideration of multidimensional reaction coordinates for water autoionization was already suggested by Geissler *et al.* [16]. In our case, the connection between O-O distances and activation energies for PT would be in agreement with the simple description pointed out above, since states with lowest activation energies (between 225 and 175 K) are those showing O-O distances smaller than the corresponding ones at liquid states (see figure 4.5, left side).

4.2.1.2 Diffusion coefficient of proton

Results for the diffusion coefficients are shown in figure 4.11 and numerically reported in table 4.2. Two important features should be discussed: (1) The general trend of the proton mobility is a neat reduction from $0.94\,\mathrm{A}^{\circ 2}$/ps at room temperature to lower values of about one order of magnitude smaller at 100 K. D_p at 298 K is in overall good agreement with previous works [137] and in excellent agreement with the experimental value $0.93\,\overset{\circ}{\mathrm{A}}{}^2$/ ps [143] (this may be fortuitous). (2) The simulation results also predict the qualitative changes observed experimentally in hexagonal ice networks [148], where the mobility of protons is due to collective effects, affecting the diffusive regime of the proton and turning it from a highly mobile solute at ambient conditions into a much slower particle at lower temperatures, with transport properties very much akin to those of a prototypical cation of small size, such as Li^+, whose diffusion coefficient is of the order of $0.1\ \overset{\circ}{\mathrm{A}}{}^2$/ps at 298 K [142]. Again proton diffusion can be regarded as an activated process (see linear fits in figure 4.11), but in this case the overall activation energy (red line, $E_D \approx 1.5$ kJ/mol) is very far from experimental findings reporting activation energies of water self-diffusion, between 14 and 70 kJ/mol for water at ice surfaces and in bulk, respectively [164]. The fits at the two phases reveal slightly higher activation energy at the liquid phase (blue line, about 2.9 kJ/mol vs. 1.5 kJ/mol for LDA ices, green line).

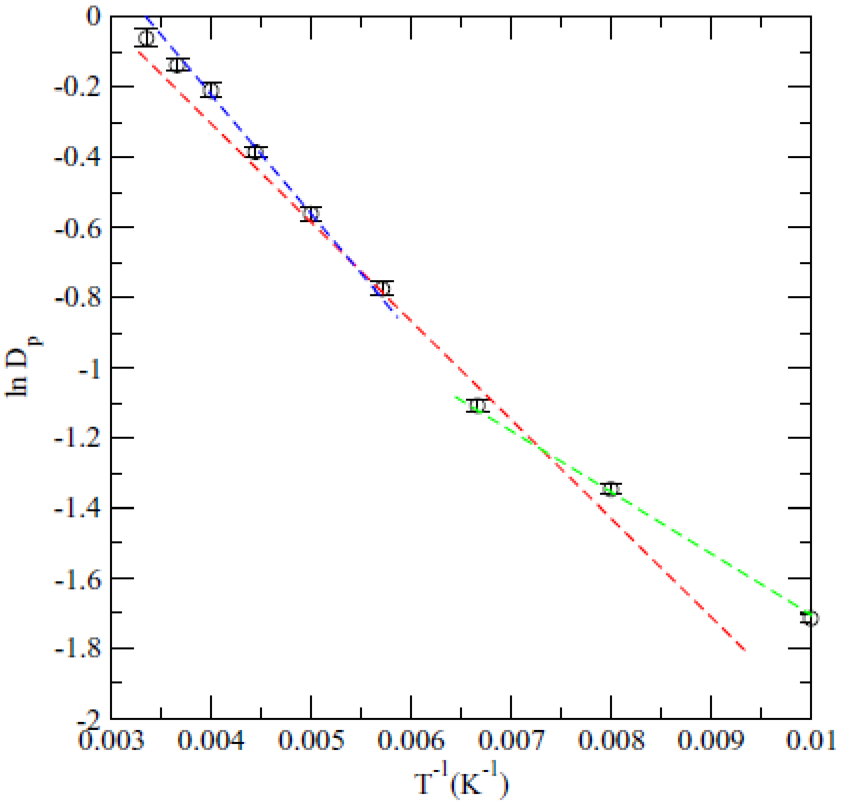

Figure 4.11: Logarithm of diffusion coefficient of proton D_p as a function of inverse temperatures. Straight lines represents the best linear fits, for liquid states (blue line), LDA ices (green line), and overall (red line).

The qualitative change in the results for the diffusion constants suggests that the role of the Grotthus mechanism as a key factor to determine the abnormal, high conductivity of the proton should become less important at low temperatures. A crude estimate of this contribution is normally obtained using simple random walk arguments: results from the proton transfer rates show that at ambient conditions the proton jumps a characteristic $O-O$ distance, say $d_{OO} \approx 3.5\,\mathring{A}$, every $\tau \approx 2$ ps. During this time interval, the center of mass of a water molecule travels typically $l \approx (6D_{\omega}\tau)^{1/2} \approx 2\,\mathring{A}$; so l is comparable to d_{O-O} and the proton transfer increases its mobility in a sizable fashion. A similar calculation performed at T = 250 K gives an average time for PT of approximately $\tau \approx 5$ps and water diffusion is significantly slower (about $0.02\,\mathring{A}^{2}$/ps [166]) yielding $l \approx 0{,}8\,\mathring{A}$ and showing that spatial displacements during the proton translocation are negligible compared to that of the center of mass of the water molecules operated by ordinary diffusion. Even though our model EVB Hamiltonian is likely to predict a lower rate of proton transfer and a subestimation of the actual diffusion, we do believe that the differences are sufficiently large to guarantee that the qualitative picture captured by our simulation experiments remains physically meaningful.

4.2.1.3 Proton spectroscopy

$S_P(\omega)$ Has been computed here based on the length of $C_P(t)$ that has been of 0.5 ps, which is long enough to capture all relevant proton vibrations, but also much shorter than the proton residence time (always larger than 2 ps, see table 4.2). As a matter of fact, we will be able to obtain relevant modes of vibration of the hydronium H_3O^+ complex.

The results are shown in figure 4.12, together with the corresponding $S_P(\omega)$ obtained from supplementary simulations of an isolated Zundel dimer $(H_5O_2)^+$ and of an Eigen complex $(H_9O_4)^+$, i.e., in the gas phase at 298 K, in order to help explaining the physical origin of the bands observed in $S_P(\omega)$. We have chosen to show the full frequency range, although the spectral domain where proton vibrations are located is between 1500 and 3600 wave numbers [144].

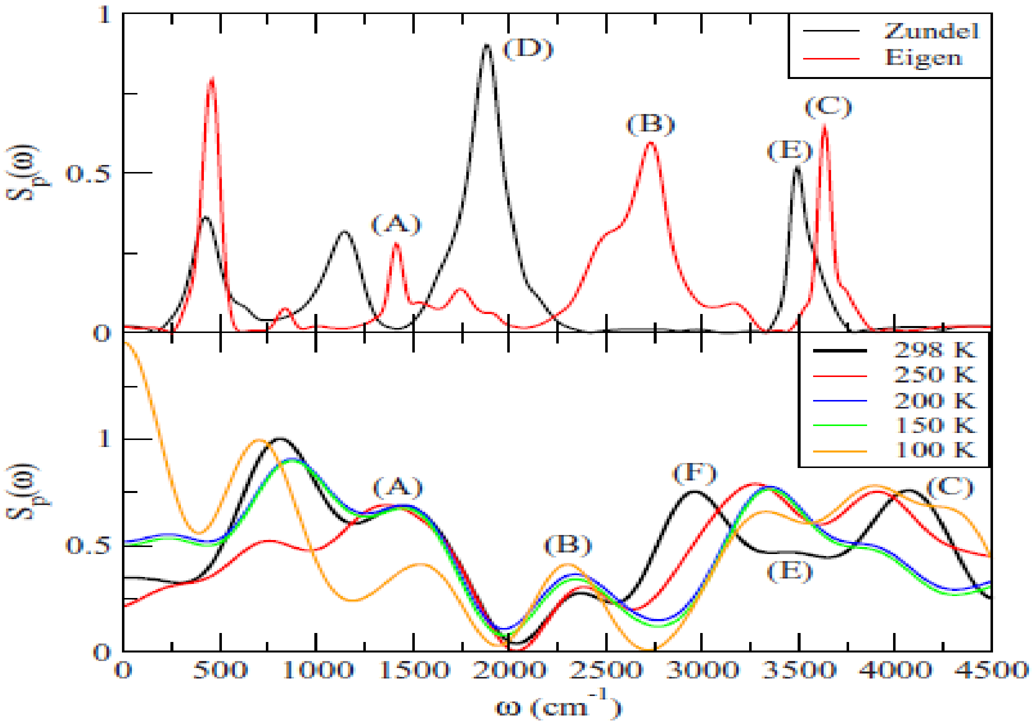

Figure 4.12: Vibrational densities of states of the lone proton $S_p(\omega)$ (in arbitrary units): (top) proton in isolated Zundel and Eigen complexes in gas phase at 298 K; (bottom) proton in water from liquid (298 K) to LDA ice states (100 K).

A common feature in the spectrum of the excess proton is found at all temperatures (bottom of figure 4.12): a series ofmaxima between 500 and 4500 cm^{-1} is observed, structured into two groups of vibrations, the first one between 500 and 1900 wave numbers and a second one between 1900 and 4500 wave numbers. Since these are frequencies of proton vibrations, they will describe both regular molecular water motions and vibrations due to the particular characteristics of the lone proton/hydronium complex. It has to be pointed out that in the present case the OH stretch of the proton will be coupled to other vibrational degrees of freedom, i.e., the microscopic motion associated with such a wide vibrational band should be regarded as a combination of collective vibrations involving the proton and water molecules nearby. Leaving apart the band with maxima around 700 cm^{-1}, typical of librational modes in water [167, 168], we observe maxima centered around 1500, 2300, 3000, and 3900 cm^{-1}. The locations of the maxima associated to proton vibrations are in good qualitative agreement with experimental data available. So, FTIR measures of HCl and NaCl aqueous solutions at different concentrations at room temperature [144], where relevant maxima associated with hydrated protons were found around 1200, 1800, and 2900 cm^{-1}. Headrick *et al.* [9] reported proton vibrations at 3160 cm^{-1} for a Zundel dimer from photoevaporation of argon in photofragmentation mass spectroscopy [9], which is also in good qualitative agreement with the features reported in the present work. Finally, Kobayashi *et al.* [81] found a value for the stretching of the proton in cubic ice around 2600 cm^{-1}. This value, about 13% larger than our findings, may be attributed to the fact that the proton structure in cubic ice shows an important extent of directionality towards its surrounding oxygens (O − H+ − O*) that would favor fast vibrational motions, instead of the less ordered LDA structures considered here.

In order to enlighten further the meaning of the spectral densities of states reported, we can establish a relationship with the data displayed at the top of figure 4.11. There we can observe that in gas phase ambients the vibrational bands associated with the Zundel dimer and the Eigen complex are centered around different frequencies. In particular, if we focus on the relevant range for proton vibrations (between 1500 and 3500 wave numbers in this case) proton vibrational modes at the Zundel dimer occur at different frequencies (about 1880 and 3500 cm^{-1}) than those inside the Eigen complex (around 1400, 2750, and 3650 cm^{-1}). First of all, these values should be compared with experimental data. So, on the one hand, Schwartz [169] reported the finding of a frequency maximum about 2660 cm^{-1} for a $H_9O_4^+$ cluster (Eigen complex) from infrared absorption spectra of several water clusters in the gas phase. Such frequency has been attributed [170] to an H-bonded H3O+ stretch.

On the other hand, a maximum at about 1740 cm^{-1} was reported from experimental measurements of the gas-phase infrared spectrum of the protonated water dimer [171] ($H_5O_2^+$). In summary, there is an overall reasonable agreement of our findings with experimental data. The reported results from computed vibrational density of states by Schmitt and Voth [130] for a different potential model were of 1550 and 2860 cm^{-1} for the two complexes, what indicates again a good agreement with our results. The relationship of the proton vibrations for the excess proton in bulk at different temperatures (bottom of figure 4.12) with the corresponding findings for the proton located at Zundel and Eigen complexes *in vacuo* (top of figure 4.12) can be explained as follows:

(1) The signatures of the Eigen-like bands are found, for our model, about 1400 (A), 2750 (B) and 3650 cm^{-1} (C) (top of figure 4.12). Bands located at corresponding maxima in bulk (bottom of Fig.4.12) are observed in all thermodynamical states considered, although the maxima are centered at the values of 1400 (A), 2370 (B), and 4050 cm^{-1} (C) at 298 K. The first of them remains essentially unchanged with temperature, whereas the band at 2370 wave numbers is red-shifted by 70 cm^{-1} at 100 K. Finally, the highest frequency feature is also red-shifted by 150 cm^{-1} at 100 K. The values around 4000 cm^{-1} (more than the corresponding 3650 cm^{-1} obtained in vacuo) should be attributed to shortcomings of the potential model, since hydrogen vibrations in water are always restricted to smaller values [172].

(2) Concerning Zundel-like bands, the lowest frequency one located at 1880 cm^{-1} (D) is absent in the liquid and LDA ice spectra, whereas the band at higher frequency around 3500 cm^{-1} (E) appears to be of low intensity at ambient conditions and located at 3400 cm^{-1}. At lowest temperatures, this mode would red-shift by some 100 cm^{-1}.

(3) A band around 2960 cm^{-1} (F) at 298 K and absent for LDA ice stat should be, at thelight of our results, unassigned with respect of the Zundel or Eigen structures. Together with this description, we can compare our results with those of Vuilleumier and Borgis [75] for a flexible SPC/E model, where the stretching modes of the hydronium complex were found at 2000 and 2650 cm^{-1} and with those obtained by Voth and coworkers [144], who assigned the modes around 1680–1880 and 3250–3400 cm^{-1} to pure Zundel-like vibrations, the modes around 1580–1640 and 2700–2950 to pure Eigen-like vibrations and the bands centered between 3400–3600 and 3650–3720 cm^{-1} to a linear combination of Zundel and

Eigen modes. From their interpretations, we can assign the mode (F) to pure Eigen-like vibrations which disappear as the system is cooled down. Finally, the mode (C) should be related with combinations of Zundel-like and Eigen-like vibrations. As a general trend, we observe a tendency of LDA ices to the slowdown of vibrational modes associated to the proton, given the red-shifts obtained for bands (B), (C), and (E) as well as the absence of mode (F) at low temperatures. These facts are probably due to the enhancement of the water structure for low temperature liquid and LDA ices, together with the important reduction of proton delocalization, as observed by the reduction of PT rates and proton diffusion.

4.2.2 Water confined-inside graphene slabs

4.2.2.1 The effects of confinement on the Proton transfer dynamics

4.2.2.1.1 Population relaxations and proton transfer rate

As in our above preliminary discussion of PT in unconfined water 3D, in this section we will start analyzing the nature of the proton transfer dynamics in the constrained water at 300 K by direct inspection of the time evolution of the pivot oxygen label during 50 ps time intervals. The results are reported in figure 4.13. Representative slab widths (3.1, 2.7, 2.3, 1.9, 1.5, 1.1, 0.9, and 0.7 nm) are shown and the effect of confinement on the frequency of proton transfer episodes can be directly observed by simply counting the number of transitions in the figures satisfying that the proton remained attached to a different water molecule for at least 0.5 ps: at d = 3.1 nm (top panel), ≈ 4 different water molecules host the proton 0.5 ps or more, roughly delivering a transfer time of the order of 0.1 ps^{-1}. That number is about ten times smaller as we move to more compressed water samples. A few PT can be still seen at d = 1.1 nm and even one of them has been captured at 0.7 nm. We should point out that the predicted rate of transfer at ambient conditions in the bulk, unconstrained system is a factor ≈ 8 larger than the one inferred from results of NMR experiments [161,162,173], being this a well-known deficiency of the semiclassical picture adopted here; moreover, the explicit incorporation of quantum fluctuations in the transferring proton yields a better agreement with the experiments, leading to rates at least twice as large as the semiclassical ones [74].

In order to improve the crude picture provided in figure 4.13 we need to use time correlation functions based on ANN aaplication. Results for the population relaxation of the pivot label are shown in figure 4.14. The presence of more than one relaxation time is clear from the absence of a single clear linear regime in the time interval analyzed. On the other hand the results for the thermodynamical states considered in this section are reported in table 4.3.

The general trend is a dramatic slowdown of PT rates when the system is gradually compressed in between the hydrophobic plates, together with the corresponding increase of the estimated residence times , the first time interval (that of lifetime of resonant episodes) shows a much faster decay for the unconfined case; whereas the influence of hydrophobic plates is very strong and τ_{rsd} leads to slowdown of the PT. When comparing to other works, we observe a good overall agreement with findings from Day *et al.* [67], who obtained a value for the proton transfer rate of 0.3 ps^{-1} at room temperature (300 K) in the unconstrained case, for an EVB model slightly different from the one used in the present work. In a variety of confined systems, it was observed the preference of the proton to stay at interfaces, where free energy minima have been found [151, 158]. This would favor the gradual reduction of PT rates that, in the present case must be influenced by the fact that the pressure has considerably grown due to the increase of the density at short interplate distances. Probably because of this fact proton transfer rates obtained in the present work are significantly smaller than those obtained from *ab initio* simulations by Bankura and Chandra [66].

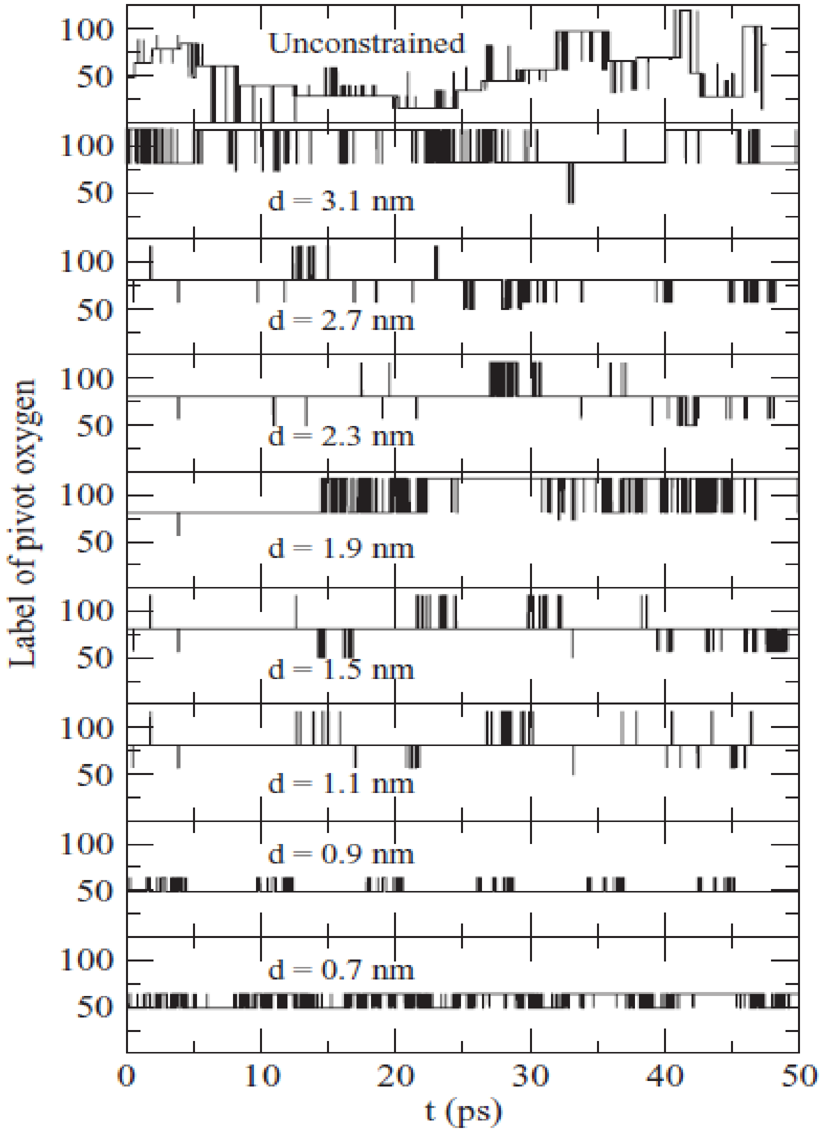

Figure 4.13: Time evolution of pivot-oxygen labeling in different aqueous environments, from quasi-3D (*d* = 3.1 nm) to quasi-2D water states (*d* = 0.7 nm) (top to bottom).

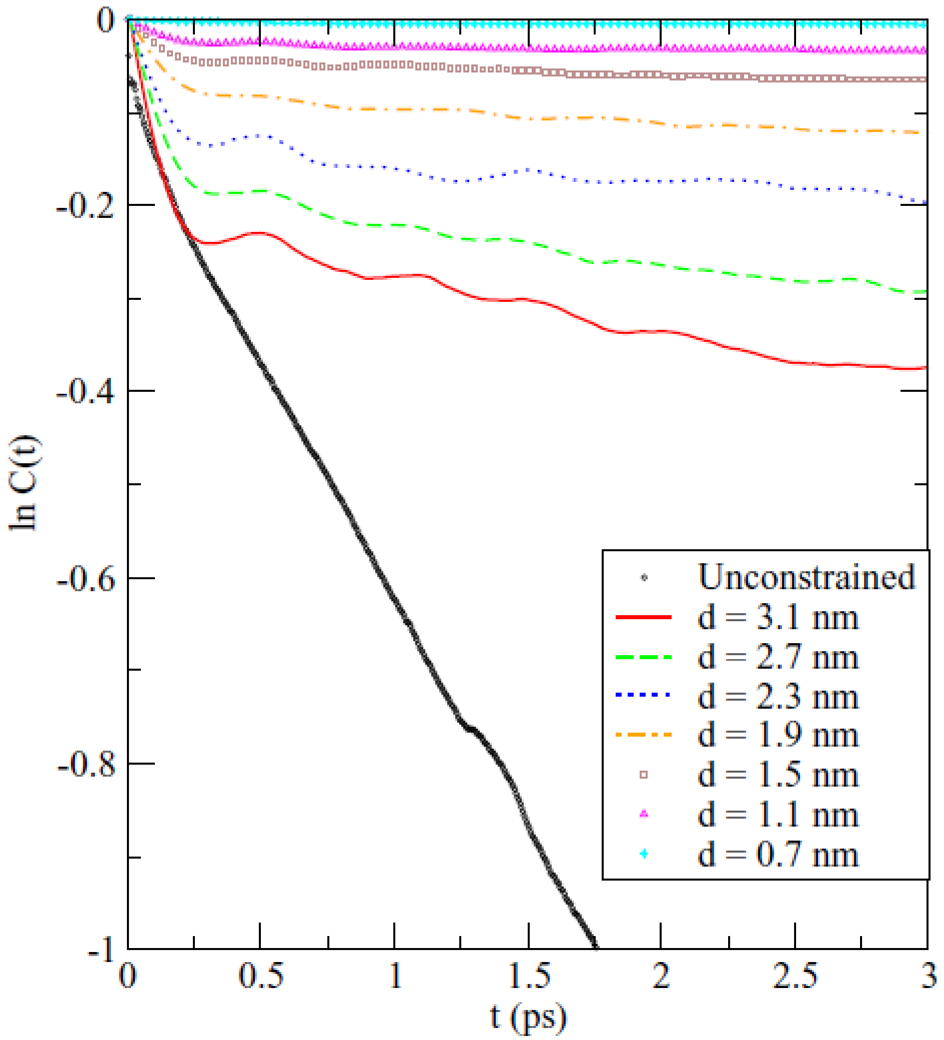

Figure 4.14: Logarithm of the population relaxations $C(t)$ for the pivot-oxygen label at different states. Unconstrained water (black circles); *d* = 3.1 nm (full red line); *d* = 2.7 nm (dashed green line); *d* = 2.3 nm (dotted blue line); *d* = 1.9 nm (dot-dashed orange line); *d* = 1.5 nm (brown squares); *d* = 1.1 nm (magenta triangles); *d* = 0.7 nm (cyan stars).

d (nm)	$\tau_{\mathrm{rsd}}^{-1}(\mathrm{ps}^{-1})$	$\tau_{\mathrm{rsd}}(\mathrm{ps})$	D_p (Å^2/ps)
3.1	0.071	14.1	0.67
2.7	0.053	18.9	0.57
2.3	0.028	35.7	0.52
1.9	0.021	47.6	0.38
1.5	0.011	90.9	0.33
1.1	0.0045	222.2	0.23
0.9	0.0028	357.1	0.20
0.7	0.0011	909.1	0.18
Unconstrained	0.54	1.85	0.94

Table 4.3: Dynamical parameters for the aqueous protons at different slab widths: proton transfer rates τ_{rsd}^{-1}, residence time τ_{rsd}, and diffusion coefficient of the lone proton D_p. Data for the unconstrained system at ambient conditions were obtained from section (4.2.1) Ref. [2]

4.2.2.1.2 Diffusion coefficient of proton

In simulations of excess protons inside quasi-one-dimensional environments, such as carbon nanotubes, it has been observed that proton diffusion is strongly affected by the tube radius and it can be either faster than in bulk water or slower [174]. The threshold is around radii of 7–8 Å. At interfaces, such as in the case of water near *n*-decane [158], lateral diffusion of the proton has been observed together with a delay of the exchange of protons between the bulk region and the interfacial region.

The calculation of diffusion coefficients of aqueous protons D_p in the constrained system considered in the present work reveals interesting changes in the previous scenarios, as it happens at interfaces or at high temperature and in supercritical states [137]. Results for the diffusion coefficients are shown in figure 4.15 and numerically reported in Table 4.3. Two important features should be discussed: (1) The general trend of the proton mobility is a neat reduction from 0.94 $\overset{\circ}{\mathrm{A}}^2$/ps at the unconstrained state to lower values up to one order of magnitude smaller inside the graphene slab (case *d* = 0.7 nm). As we pointed before, D_p at 298 K is in overall good agreement with previous works [137] and in excellent agreement with the experimental value 0.93 $\overset{\circ}{\mathrm{A}}^2$/ps [142] (this may be fortuitous). (2) The simulation results also indicate that the reduction of D_p for decreasing interplate distances *d* is roughly linear. Here we should keep in mind that we set up our simulations in such a way that density is bigger at low *d*, so that an important part of the HB network has survived. Since the Grotthuss shuttling operates via HB, the mechanism can work in all cases, even at the quasi-two-dimensional slab at *d* = 0.7 nm. To compare with a similar system, Bankura and Chandra [66] obtained values around 0.1 $\overset{\circ}{\mathrm{A}}^2$/ps for a grapheme slab 1.2 nm wide, which is quite well matched by the value of 0.23 $\overset{\circ}{\mathrm{A}}^2$/ps reported in this work for the interplate distance of 1.1 nm. The factor two between these works should be due to a density effect, within the relative accuracies and reliabilities of the different methodologies employed.

As it was observed previously in section (4.2.1), the structural characteristics of the local proton environment have significant influence on proton diffusion: at bulk water ambients the proton jumps a characteristic O-O distance, say $d_{oo} \approx 3.5A^{\circ}$, every $\tau \approx 2$ ps. In this interval, the center of mass of a water molecule travels typically $l \approx (6D_{\omega}\tau)^{1/2} \approx 2\overset{\circ}{\mathrm{A}}$; so *l* is comparable to d_{oo} and PT operates safely through Grotthuss mechanism. A similar calculation performed at *d* = 3.1 nm gives an average time for PT of approximately $\tau \approx 14$ ps, whereas water diffusion is slower ($0.67\,\overset{\circ}{\mathrm{A}}^2$/ps, see table 4.3), yielding $l \approx 7.5A^{\circ}$ and showing that spatial displacements during the proton translocation are significantly bigger than those of $d_{O*O} \approx 2.5\overset{\circ}{\mathrm{A}}$ (see figure 4.5), which makes the transfer of the proton more difficult. Even though our model EVB Hamiltonian is likely to predict a lower rate of proton transfer and a subestimation of the actual diffusion, we do believe that the differences are sufficiently large to guarantee that the qualitative picture captured by our simulations remains physically meaningful.

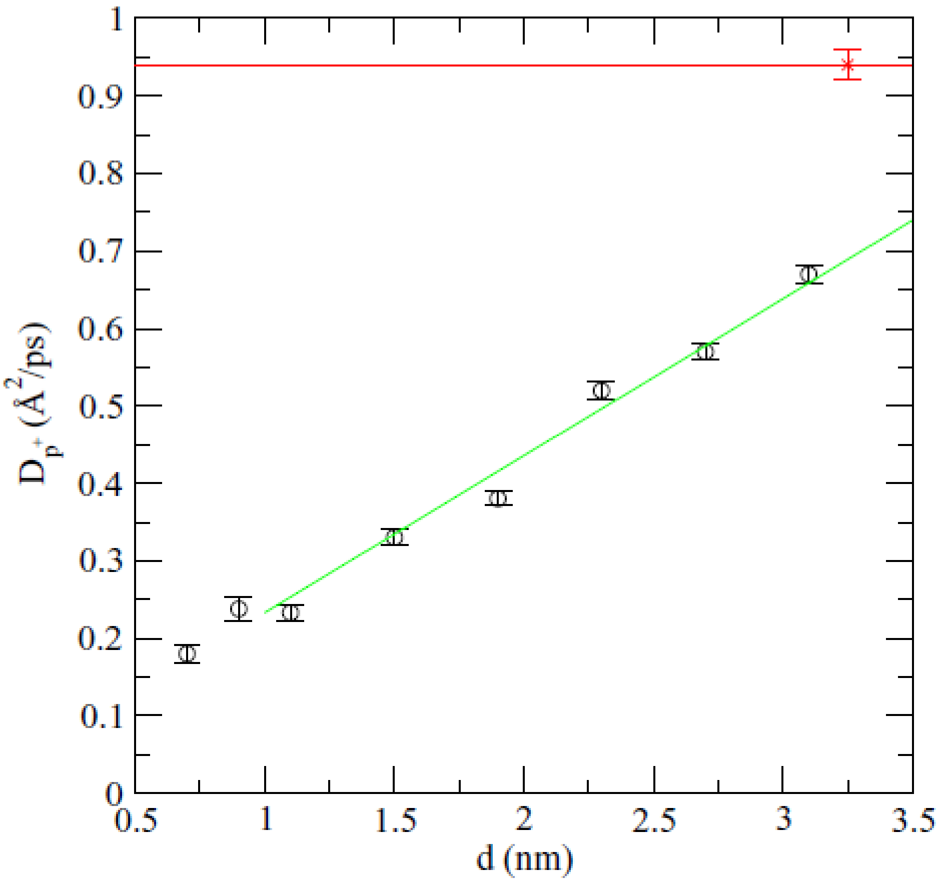

Figure 4.15: Diffusion coefficients of lone proton (circles) as a function of slab width *d*. Linear fit (green line) is indicated as an aid to the eye. The red star indicates the corresponding value for the unconstrained system.

4.2.2.1.3 Proton spectroscopy

We have computed $S_P(\omega)$ for all slab widths. The length of $C_P(t)$ has been of 0.5 ps, which was long enough to capture all relevant proton vibrations, but also much shorter than the proton residence time (always larger than 10 ps; see table 4.3). However, as a matter of fact, we will be able to obtain relevant modes of vibration of the hydronium H_3O^+ complex. We have chosen to show roughly the full frequency range, since although specific spectral signatures of proton vibrations are located between 1400 and

3000 wave numbers [75,144], some authors like Hammer *et al.* [8] include the range between 850 and 1400 as relevant for shared proton motions.Within the specific region of proton vibrations, three common features in the spectrum $S_P(\omega)$ for the unconstrained case (bottom plot, figure 4.16, black line) are clearly observed, represented by maxima at: (1) 1445 cm^{-1}, labeled as (A); (2) 2370 cm^{-1}, labeled as (C-D); and (3) 2960 cm^{-1}, labeled as (E). Further, a broad band between 600 and 1000 cm^{-1} (F) might be also related to low-frequency proton vibrations. In all computed spectra, the uncertainty in the frequency location of maxima is of the order of 10 cm^{-1}, as it has been obtained from a series of independent simulations. When spectra from the confined proton are considered, some spectral shifts $\Delta\omega$ have been found. So, the band (A) is red-shifted by 50–100 wave numbers at the widest slab widths (d = 3.1 to 1.5 nm), where as it shows a blue shift of around 75 wave numbers for the narrowest slab separations, namely 0.7 and 0.9 nm. In the case of band (C-D), all shifts are toward blue, but while for the separations between 3.1 and 1.5 nm the absolute value is $\Delta\omega$ = 30–40 cm^{-1}, at narrow separations it becomes much bigger (around 200 cm^{-1}). Finally, the band (E) reveals a neat blue shift of the order of 200 cm^{-1} for all cases. The band maxima associated with proton vibrations are in an overall good qualitative agreement with experimental data available.

Fourier transform infrared spectra (FTIR) measurements of HCl and NaCl aqueous solutions at different concentrations at room temperature [144] revealed maxima associated with hydrated protons at 1200, 1800, and 2900 cm^{-1}, whereas Headrick *et al.* [9] considered protonated water clusters in argon and reported proton vibrations in a hydronium ion at 2665 and water vibrations inside a Zundel dimer at 3160 cm^{-1}, from photo evaporation of argon in photofragmentation mass spectroscopy. For the same system, Hammer *et al.* [8] reported bands around 1000–1150 cm^{-1} that were assigned to shared proton (Zundel dimer) vibrations. In summary, these values are in reasonably good qualitative agreement with the frequencies around 900, 1445, and 2960 cm^{-1} reported in the present work. In addition, the band (C-D) centered around 2370 cm^{-1} can be considered in close agreement with the maxima at 2420 cm^{-1} reported in Ref. [9] associated to a hydronium symmetric stretch mode.

As a benchmark for the force field considered in this work, we computed the vibrational bands associated with the isolated Zundel dimer and Eigen complex, equivalent to gas phase [2] (see figure 4.16). In particular, proton vibrational modes for the Zundel dimer occur at different frequencies, about 1150, label (F) and 1880 cm^{-1}, label (G) than those of the Eigen complex, around 1400 (A), 1750 (B), 2500 (C), 2750 (D), and 3650 cm^{-1} (E). The agreement of these values with corresponding ones from experimental data is quite satisfactory. On the one hand, Schwartz [169] reported a frequency maximum about 2660 cm^{-1} for a $H_9O_4^+$ cluster (Eigen complex) from infrared absorption spectra of several water clusters in gas phase, attributed by Okumura *et al.* [170] to a hydronium (H_3O^+) ion stretch. On the other hand, a maximum at about 1740 cm^{-1} was reported from experimental measurements of the gas-phase infrared spectrum of the protonated water dimer [171] ($H_5O_2^+$).

The reported results from computed vibrational density of states by Schmitt and Voth [130] for a similar potential model were of 1550 and 2860 cm^{-1} for the two complexes, which indicates again a good agreement with our results. Further, the agreement is reasonably good with results from Vuilleumier and Borgis [75] for a flexible SPC/E model, who reported stretching modes of the hydronium complex at 2000 and 2650 cm^{-1} along with those obtained by Voth and coworkers [144]: these authors assigned the modes around 1680–1880 and 3250–3400 cm^{-1} to pure Zundel-like vibrations, and the modes around 1580–1640 and 2700–2950 to pure Eigen-like vibrations.

Comparing the reference maxima for Zundel and Eigen moieties (top of figure 4.16) with the spectral profiles obtained for the condensed liquid system (bottom of figure 4.16), we can draw some additional clues: (1) the bands centered at 1445 and 2960 cm^{-1} in the spectrum of proton in confined water inside the graphene slab match well the maximum (A) for the isolated Eigen complex; (2) the band maximum at 2370 cm^{-1} can be related to the maxima (C) and (D) of the isolated Eigen; and (3) the broad band centered around 750–1000 cm^{-1} in the spectral densities at the bottom of Fig.4.16 have no clear counterpart at the top of the same figure, although the closest band maxima is a peak at 1100 cm^{-1} of the Zundel power spectrum. In summary, the dynamical exchange between the two species seems to remain in confinement, even in the case of quasitwo-dimensional structures formed by a few water layers. As an additional fact, we should note that a vibrational frequency around 2400–2600 cm^{-1} was reported by Headrick *et al.* [9] and assigned to the asymmetric stretch motions of hydronium. Following this, the band labeled (C-D) in the aqueous proton spectrum might indicate the presence of a lone hydronium ion in the states of higher compression (0.7, 0.9 nm) as indicated by the blue shift of this (C-D) band as *d* decreases. This fact that hydronium species may replace Zundel cations (and/or Eigen complexes) was already observed by Habenicht *et al.* [175] in their study of the effects of hydrophobic confinement on protons from acidic systems.

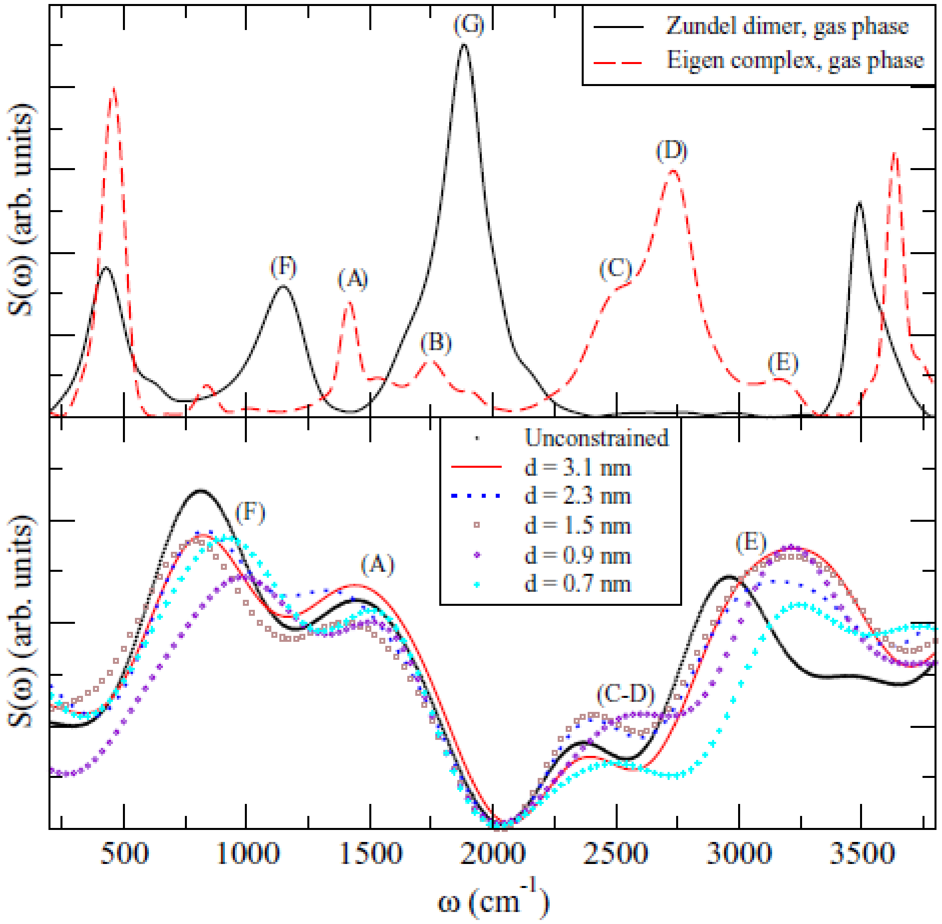

Figure 4.16: Vibrational densities of states *Sp* (*ω*) (in arbitrary units): proton in Zundel (black full line) and Eigen (red dashed line) complexes in gas phase at 298 K (top); confined states, from 3D water (*d* = 3.1 nm) to 2D water states (*d* = 0.7 nm) (bottom). Unconstrained water (black circles); *d* = 3.1 nm (full red line); *d* = 2.3 nm (dotted blue line); *d* = 1.5 nm (brown squares); *d* = 0.9 nm (violet diamonds); *d* = 0.7 nm (cyan stars).

4.2.2.2 The effects of temperature and confinement on the proton transfer dynamics

4.2.2.2.1 Population relaxations and proton transfer rate

Using the same fashion as before, again the most direct way to analyze dynamics' of proton transfer is by direct inspection of how the label of the pivot oxygen changes in time. We monitored pivot oxygen's label during 50 ps time intervals, as shown in figure 4.17.

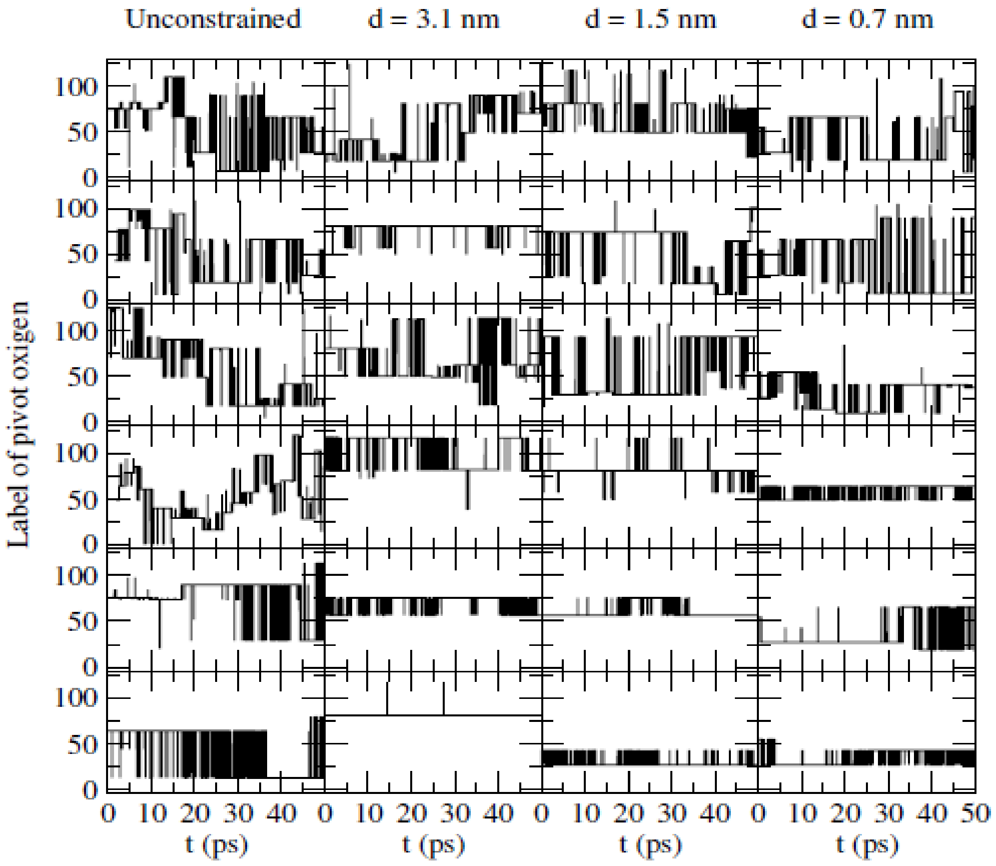

Figure 4.17: Time evolution of pivot-oxygen labelling in different aqueous environments, from 100 to 600 K and for all interplate separations.

There we compared the six temperatures considered in the present study for the three interplate distances of 3.1, 1.5 and 0.7 nm together with corresponding results for the bulk, unconstrained systems 3D. The proton hopping patterns can be regarded as a sequence of episodes in which the proton is attached to one particular water during short to long time intervals, combined with other intervals in which the proton resonates between two given valence bond states. The latter is usually called proton rattling, with a “special" (resonant) bond [75]. Isolated single spikes reveal attempts of aborted transitions. From figure 4.17 the frequency of proton transfer episodes is directly seen, by simply counting the number of transitions recorded: At T = 300 K (panels at the first column from the left), about ≈ 20 water molecules retain the pivot label during time intervals of ≈ 0.5ps or longer, which roughly corresponds to a transfer time of 0.4 ps^{-1}, this is similar to the values that we can extract at higher temperatures. However, at lower temperatures the number of transitions decreases dramatically and only (≈ 5) are seen at 200 K and 2 at 100 K. When the system is placed inside the graphene slab, the number of PTs clearly diminishes and is virtually zero for constrained states at T < 300. At room temperature, PT in all cases is seen at frequencies much lower than for the unconstrained counterparts. So, for instance, the number of transitions for d = 3.1 nm at 600 K is around 7 but at the d = 0.7 nm case it is only of 4-5. Here it should be pointed out that the predicted rate of PT at ambient conditions (order of 0.5 ps^{-1}) is a factor ≈ 8 larger than values reported from NMR experiments [161,162, 173]. This is a known deficiency of the semi-classical model adopted here, although explicit incorporation of quantum fluctuations in the model of transferring proton produces a better agreement with experiments [74].

As we pointed before, the rough picture of PT dynamics described from figure 4.17 cannot provide a quantitative estimation of PT rates. However, again we may improve the calculations in this section using time correlation functions. Our results for the population relaxation of the pivot label are shown in figure 4.18.

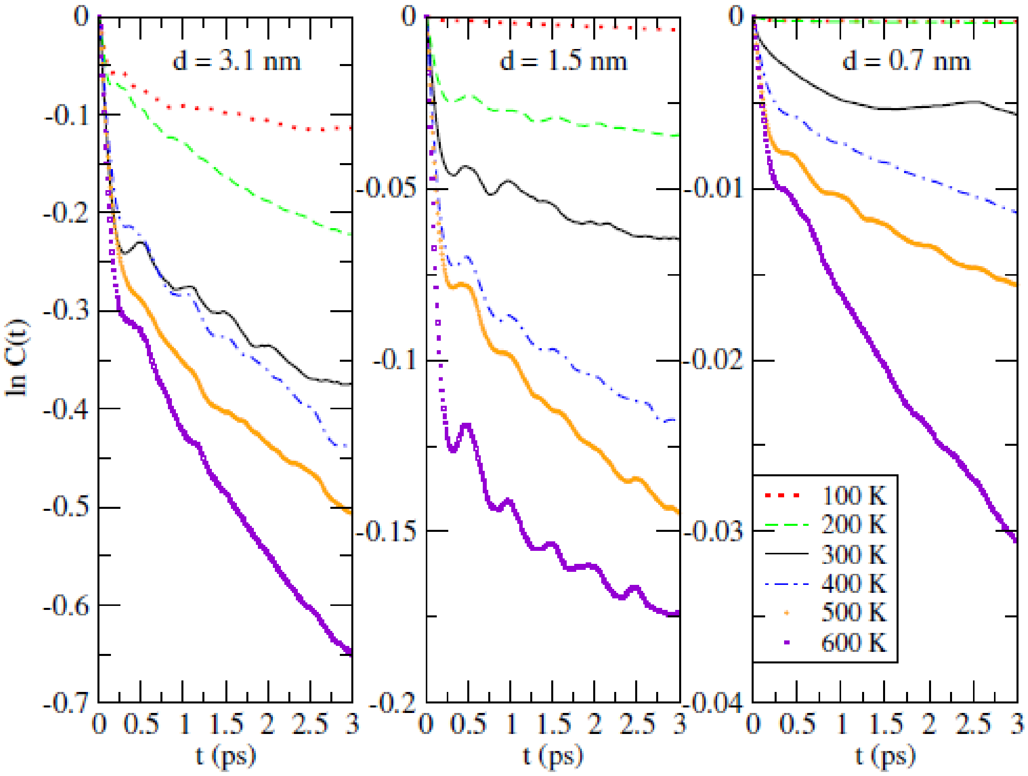

Figure 4.18: Logarithm of the population relaxations at different thermodynamical states and interplate separations.

The presence of several relaxation times is clear from the shapes of the correlation functions, showing that at least one fast decay at short times (up to 0.5 ps) and a slow decay starting around 1.5 ps. On the other hand, the full results for all the thermodynamical states considered in this case are reported in Table 4.4. We observe a general trend for all cases: relaxation times of $C(t)$ are systematically reduced when the system is heated up from LDA ice states (100 and 200 K) to sub-critical high temperature states (500 and 600 K). This means that proton transfer rates increase and, equivalently residence times τ_{rsd} decrease.

The comparison between the three interplate separations reported in this present case indicates a clear trend of PT slowdown when the distance becomes smaller. Further, the numerical values obtained for the widest distance of 3.1 nm are quite similar to those found for the unconstrained systems (see table 4.2) and close to the values reported by

Bankura and Chandra [66] for a single H^+ in a water monolayer. However, when separations are smaller (1.5 and, especially, 0.7 nm) PT rates decrease dramatically. When considering other simulation works, our data are in good overall agreement with findings from Day et al.[71], who obtained a value for the proton transfer rate of 0.3 ps^{-1} at room temperature (300 K), for an EVB model slightly different of the one used in the present work.

For cubic ice, it was reported [80,81] that the ratio between PT rates of liquid and ice phases is around 2, fact essentially attributed to the larger extent of localization of $(O-O^*)$ pairs, which could be at the basis of the PT mechanism in ices. In order to further investigate the temperature dependence of PT rates, we represented log k_p versus T^{-1} in Fig.4.19 and explored the tendency to Arrhenius-like dependence and obtain the eventual activation energies E_k for PT.

Hence, the dependence of the proton transfer rate with temperature is based on the same assumptions of equation (4.1). Then from the calculation of the slopes of the straight lines shown in the Arrhenius plots of Fig.4.19 we get the series of values of E_k reported in table 4.5. A fit to the full set has been considered (continuous lines) and, since PT rates at 100 K seem to show a different trend, a fit to temperatures between 200 and 600 K (dashed lines) has also been taken. In the latter case, regression coefficients indicate a larger extent of Arrhenius-like behavior. Available experiments by Moon et al, [163,164], by Kim et al.[83] and by Luz and Meiboom [165] obtained values of the order of 10 kJ/mol for the activation energy of PT at the surface of polycrystalline ice films (135 K), when the PT is mediated by hydroxyl ions and for PT in pure water, respectively, using methods such as reactive ion scattering and proton magnetic relaxation measurements. In our case, the values reported in table 4.5 are between (2 and 12 kJ/mol). When fitting the full set of data, activation energies are around (4 kJ/mol) for unconstrained water and between (2 and 5 kJ/mol) for the confined setups, with the highest activation energy corresponding to the strongest confinement, i.e. when the separation between graphene plates is the shortest. If the fit is considered only for temperatures between 200 and 600 K, values of activation energies rise but showing the same trend described above.

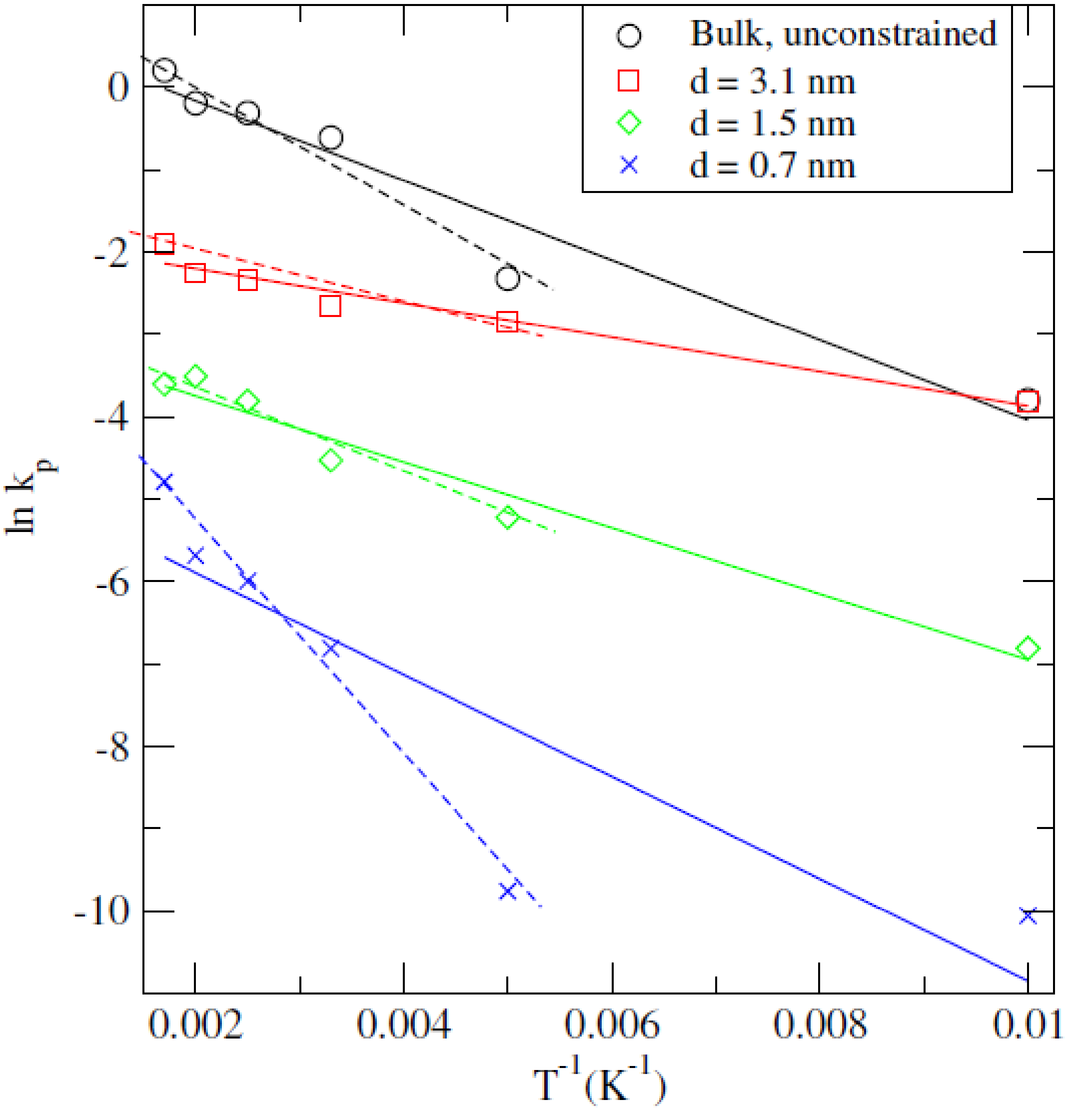

Figure 4.19: Proton transfer rates as a function of temperature and interplate separation. The straight lines represent the best overall linear fits: bulk unconstrained systems (black line); d = 3.1 nm (red line); d = 1.5 nm (green line) and d = 0.7 nm (blue line). Dashed lines are best linear fits for temperatures between 200 and 600 K.

In summary, confinement does not alter significantly the energy barrier for activation of PT calculated for the free unconstrained liquid, with the exception of d = 0.7 nm, where PT becomes a process requiring energy much bigger than at interplate distances of 3.1 and 1.5 nm. This suggests that the slowdown of PT at low temperatures and severe confinement is mainly due to the lack of thermal energy and to the high degree of localization of the proton. In this way, the relationship between the likeliness of PT and the oxygen-oxygen distances of solvating water molecules was proposed some time ago by Marx [26]. The main idea was that at short distances, say for the Zundel dimer, there is a minimum in the external potential of the proton when located along the O-O axis at equal distances of the two oxygens. Conversely, when the proton is closer to one of them the potential shows a maximum. However, Marx suggested that the correct picture should consider a two dimensional proton external potential depending of two variables: R_{O-O} and the proton displacements coordinate r_p .

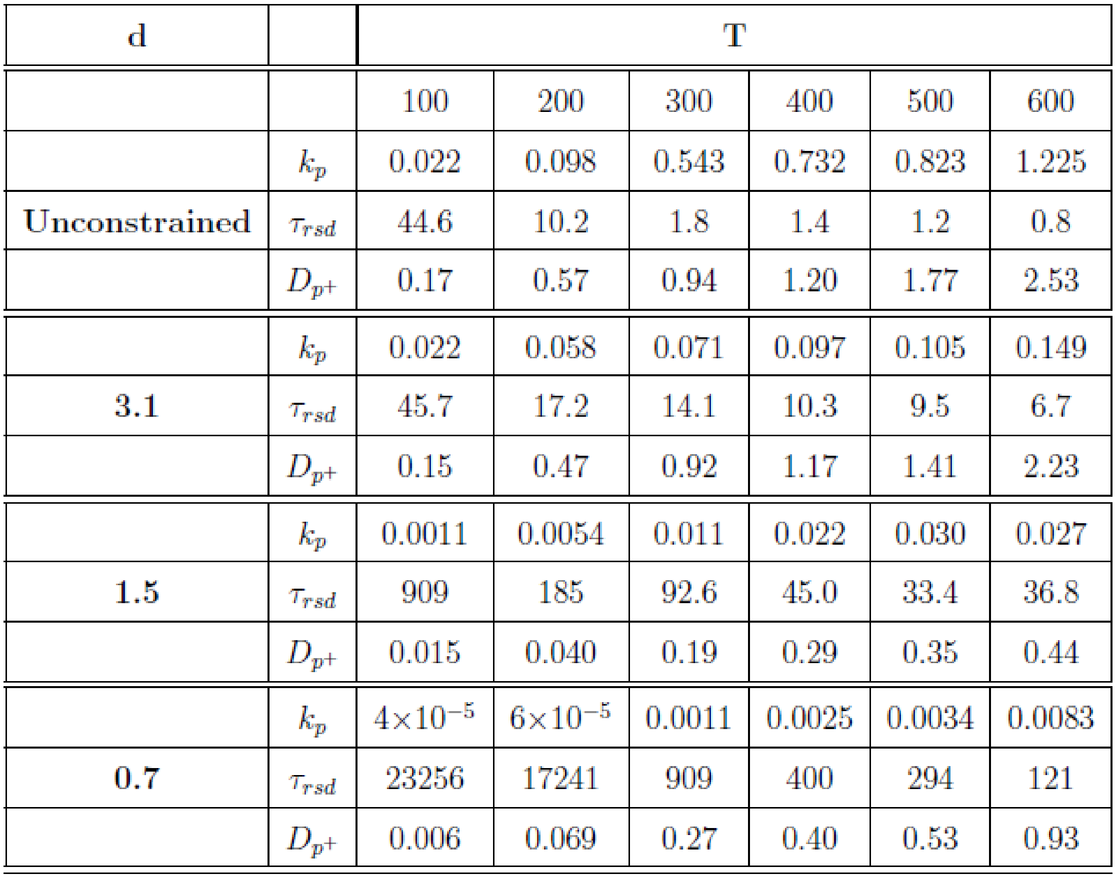

d		T					
		100	200	300	400	500	600
	k_p	0.022	0.098	0.543	0.732	0.823	1.225
Unconstrained	τ_{rsd}	44.6	10.2	1.8	1.4	1.2	0.8
	D_{p+}	0.17	0.57	0.94	1.20	1.77	2.53
	k_p	0.022	0.058	0.071	0.097	0.105	0.149
3.1	τ_{rsd}	45.7	17.2	14.1	10.3	9.5	6.7
	D_{p+}	0.15	0.47	0.92	1.17	1.41	2.23
	k_p	0.0011	0.0054	0.011	0.022	0.030	0.027
1.5	τ_{rsd}	909	185	92.6	45.0	33.4	36.8
	D_{p+}	0.015	0.040	0.19	0.29	0.35	0.44
	k_p	4×10^{-5}	6×10^{-5}	0.0011	0.0025	0.0034	0.0083
0.7	τ_{rsd}	23256	17241	909	400	294	121
	D_{p+}	0.006	0.069	0.27	0.40	0.53	0.93

Table 4.4: Dynamical parameters for the aqueous H^+ at different thermodynamic states: proton transfer rates k_p in ps^{-1}, residence time of proton τ_{rsd} in ps and diffusion coefficient of the lone proton D_{p+} in $\mathring{A}^2$/ps. d is the interplate distance in nm and T is the temperature in K. The estimated errors in all values are within the precision of the last significant figure.

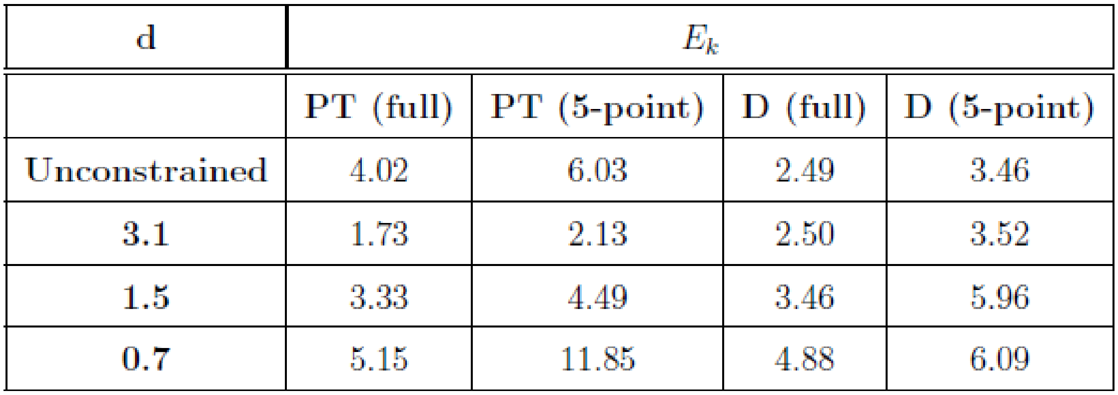

d	E_k			
	PT (full)	PT (5-point)	D (full)	D (5-point)
Unconstrained	4.02	6.03	2.49	3.46
3.1	1.73	2.13	2.50	3.52
1.5	3.33	4.49	3.46	5.96
0.7	5.15	11.85	4.88	6.09

Table 4.5: Activation energies (E_k, in kJ/mol) for the aqueous H^+ at different interpolate separations d (in nm): PT stands for proton transfer activation energy and D for proton diffusion activation energy. "Full" corresponds to the fit of all inverse temperatures in figures 4.19 and 4.21 (continuous lines) whereas "5-point" stands for the fit for inverse temperatures between 0.0017 and 0.005 in figures 4.19 and 4.21 (dashed lines).The estimated errors in all values are within the precision of the last significant figure.

4.2.2.2.2 Diffusion coefficient of proton

In the present case, as it was considered in section (4.2.2.1) the systems under study allow some mobility of the proton species along the Z-direction so that we kept the factor $\frac{1}{6}$ in the formulas of equation (3.19) instead of the factor $\frac{1}{4}$ considered in pure 2D simulations. Therefore, the mean square displacements of the proton are shown in figure 4.20 and the corresponding diffusion coefficients are reported in table 4.4. In general, the values of D_p reported here are of the same order of magnitude as those from Ref [66] for a single water layer inside graphene plates. From mean square displacements two general trends are observed: (1) at the widest graphene-graphene separation of d = 3.1 nm, proton diffusion is significantly larger than at the shortest d (note that the same scale has been adopted for all cases); (2) within each d diffusion decreases monotonically with temperature. So the general fact is that proton mobility is limited by confinement and enhanced by temperature. When numbers are considered, our first observation concerns the reliability of the model and methods considered here: we get a value of D_p = $0.94\,\overset{\circ}{A}{}^2$/ps for the reference setup of room temperature for the unconstrained system, in excellent agreement with the experimental value reported above.This value remains unaltered for d = 3.1 nm but decreases roughly by a factor 4 in the cases of d = 1.5 and 0.7 nm. When we cool down the system and reach the range of LDA states (100 and 200 K), obviously D_p decreases drastically down, up to values of one (d = 1.5 nm) to two (d = 0.7 nm) orders of magnitude smaller. Here we deal with qualitative changes already observed experimentally in hexagonal ice networks [148], where the proton turns down from a highly mobile solute at ambient conditions into a much slower particle at lower temperatures.

As it has been pointed out, transport properties of the proton are similar to those of a small cation such as Li^+, whose diffusion coefficient is about $0.1\,\overset{\circ}{A}{}^2$/ps at 298 K [137]. In the range of high temperatures (400 to 600 K), the behavior tends to remain more stable, with changes up to a factor 3 in the most extremal case (again for d = 0.7 nm) where diffusion rises from 0.27 at 300 K to $0.93\ \overset{\circ}{A}{}^2$/ps at 600 K. So we obtain a more important influence of temperature over confinement in the proton diffusion.

In the same fashion as for PT rates, we can consider proton diffusion as an activated process (see figure 4.21) and evaluate linear fits of $\ln D_p^+$ as a function of T^{-1}, including or excluding the case of 100 K, which turns out again to be the most controversial (see table 4.5). In this case the overall fits (continuous lines) render activation energies slightly smaller than those from fits up to 200 K (dashed lines). However, the values are always in the range 2.5 to 6 kJ/mol. These values are in general very far from experimental findings reporting activation energies of water self-diffusion, between 14 and 70 kJ/mol for water at ice surfaces and in bulk, respectively [164] we observed that the Arrhenius-like behavior is more marked for the cases excluding the 100 K set.

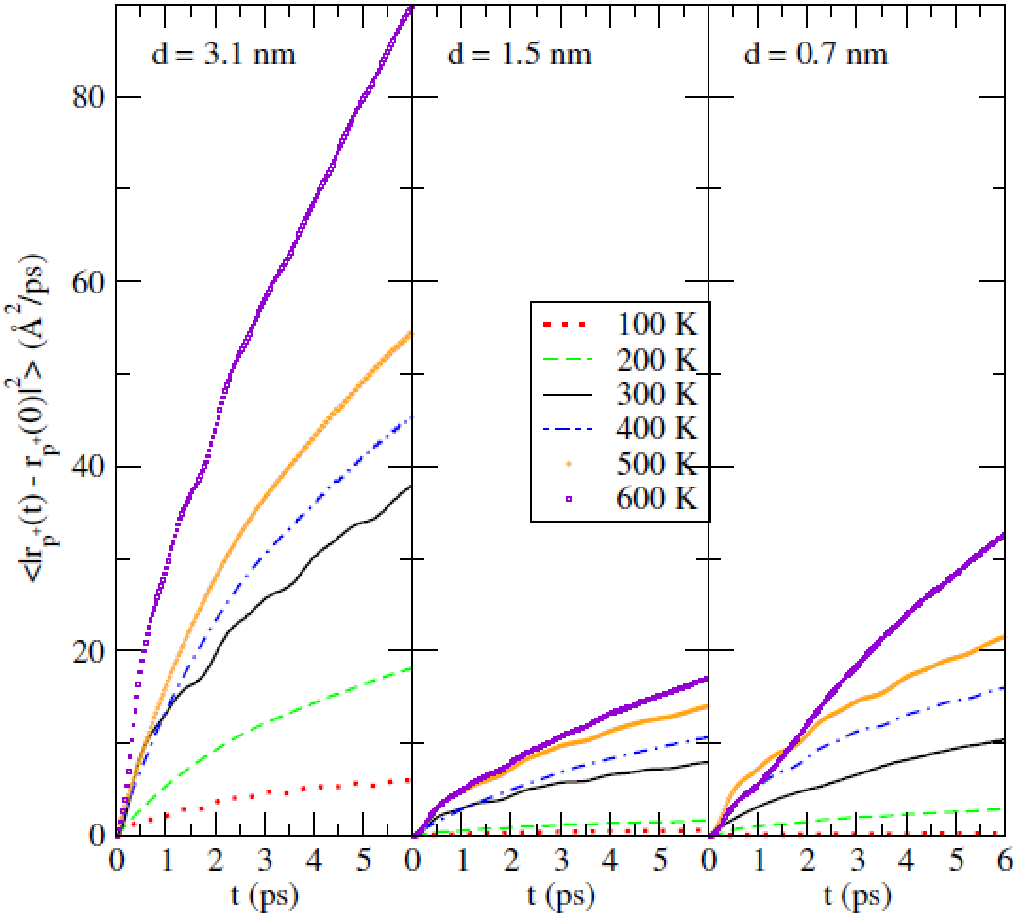

Figure 4.20: Mean square displacements of proton species at different interplate separations (left to right): d = 3.1; 1.5 and 0.7 nm as a function of temperature.

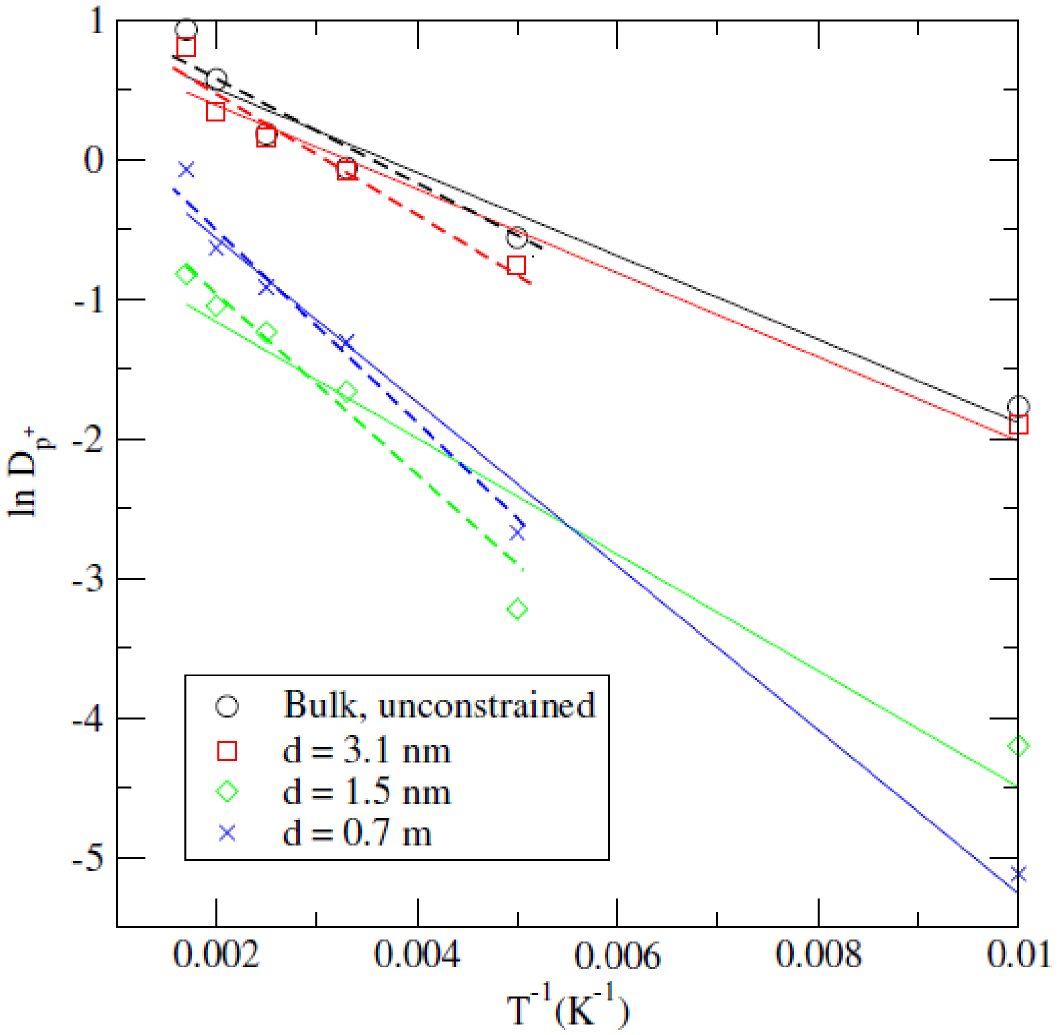

Figure 4.21: Diffusion coefficients of the excess proton as a function of inverse temperature for variable interplate distances. Straight lines represent the best overall linear fits, whereas dashed lines account for fits between 200 and 600 K.

4.2.2.2.3 Proton spectroscopy

We have computed $S_P(\omega)$ for a variety of thermodynamic states considered along the present case. For the sake of clarity, not all states have been included in figure 4.22, only those showing significant features. All $C_P(t)$ have been computed up to 0.5 ps, time long enough to capture all relevant proton vibrations and safely shorter than the proton residence time (see table 4.4), in order to make sure that the proton is attached to a given pivot oxygen during the whole period of calculation of $C_p(t)$. As the general fact, we will report the relevant modes of vibration of the proton inside a hydronium H_3O^+ complex, either being part of a Zunder or an Eigen species. As usual, we included in our results a comparison to the corresponding $S_p(\omega)$ obtained from supplementary simulations from the sections above [2] of an isolated Zundel dimer $(H_5O_2)^+$ and of an Eigen complex $(H_9O_4)^+$ i.e. in the gas phase at 298 K. These reference spectra are very helpful to interpretate the existence of those distinctive species at the different states.

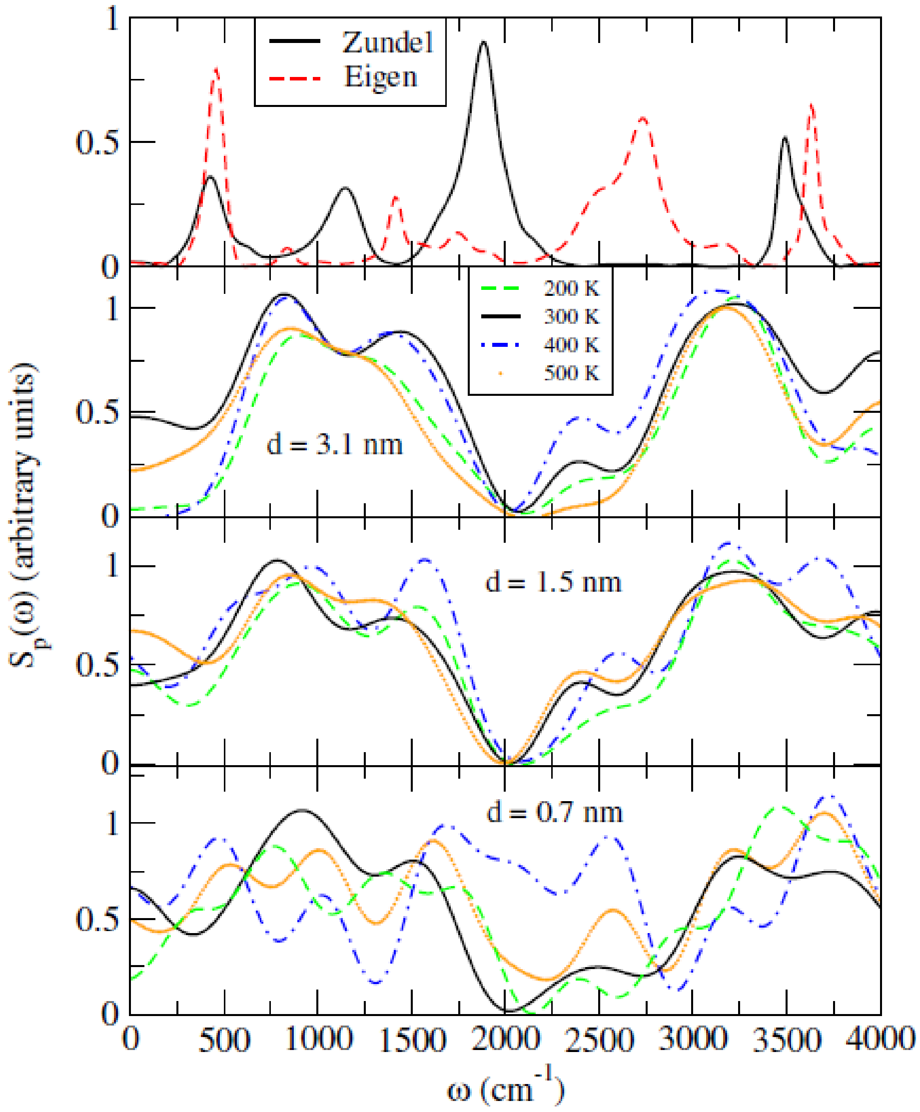

Figure 4.22: Vibrational densities of states $S_p(\omega)$ (in arbitrary units): d = 3.1; 1.5 and 0.7 nm. Proton spectra of Zundel and Eigen complexes in gas phase at 298 K have been also included.

A general common feature observed in the spectra of the excess proton in all cases is the series of maxima between 300 and 4000 cm^{-1}. These maxima are structured into two separated ranges: one between 500 and 2000 wave numbers and another between 2000 and 4000 wave numbers. Since the proton is attached to one, two or three water groups, the frequency band and maxima will account for individual (proton) and collective vibrational modes, associated to hydronium, Zundel-like or Eigen-like vibrations. As the interpolate distance becomes smaller, the number of relevant maxima tend to increase. In the case of d = 0.7 nm the number of maxima is significantly larger than at lower d and this might indicate that size effects due to the reduced space along Z-axis have been somehow captured.

Assuming that the bands located below 1000 cm^{-1} are typical of librational modes in water [167,168] and not characteristic of proton vibrations, we will focus our analysis on the maxima located (for the gas phase) around (see top of figure 4.22): (1) 1200, 1900 and 3500 cm^{-1} (Zundel dimer); (2) 1450, 2750 and 3600 cm^{-1} (Eigen complex). First of all we should point out that our method is able to locate band maxima but it cannot reproduce heights and widths of such bands. To do so we would need to rely on a full quantum simulation. As a general fact, locations of maxima associated to proton vibrations are in overall good qualitative agreement with experimental data. Firstly, Kobayashi et al. [81] measured the frequency of the proton stretch in cubic ice around 2600 cm^{-1}. The value reported in the present work is of about 2400 cm^{-1} (clearly seen at 200 K for the case of d = 0.7 nm) i.e. only 8% smaller. This may be attributed to the fact that the proton structure in cubic ice presents a larger degree of directionality than in the LDA states considered here.

This would favor faster vibrational modes. Secondly, FTIR measurements of HCl and NaCl aqueous solutions at 300 K [144] reported relevant maxima associated with hydrated protons around 1200, 1800 and 2900 cm^{-1}. Further, Headrick et al.[9] reported proton vibrations at 3160 cm^{-1} for a Zundel dimer from photoevaporation of argon in photofragmentation mass spectroscopy, which is also in reasonable good qualitative agreement with the maxima reported here. Schwartz [169] also reported the finding of a frequency maximum about 2660 cm^{-1} for a H_9O^{+4} cluster (Eigen complex) from infrared absorption spectra of several water clusters in gas phase. Such frequency has been attributed[170] to an H-bonded H_3O^+ stretch.

The comparison of our findings with those from other simulation works indicates again a good overall agreement. We obtained maxima centered at 1500, 2400 and 3200 cm^{-1} and the results from Vuilleumier and Borgis [75] (also for a exible SPC/E model) reported stretching modes of the hydronium complex at 2000 and 2650 cm^{-1}, whereas Voth and coworkers [144] assigned modes around 1680-1880 and 3250-3400 cm^{-1} to vibrations of Zundel dimers and modes around 1580-1640 and 2700-2950 to vibrations of the Eigen complex. Finally, bands around 3400-3600 and 3650-3720 cm^{-1} were associated to a linear combination of Zundel and Eigen modes. The reported results from computed vibrational density of states by Schmitt and Voth [130] for a different potential model were of 1550 and 2860 cm^{-1} for the two complexes.

A simple way to interpretate the spectral densities of states in figure 4.22 is by means of the help of the signatures obtained from the simulation of a Zundel dimer and an Eigen complex in gas-like ambients. The agreement of the maxima with available experimental data has been previously established (see section (4.2.1.3**)** and references therein). In the present case, the interpretation of proton vibrations through the influence of both confinement and temperature and the relationship with the existence of Zundel and Eigen complexes can be summarized as follows:

1. At the reference state of 300 K, the main bands of the spectra are located around 1500 (A), 2400 (B) and 3250 cm^{-1} (C). No significant changes are observed as the interplate distance d moves from 3.1 to 0.7 nm. From experimental measurements of spectral signatures of water clusters [8] it is known that the band centered at 1600 wave numbers may be attributed to the existence of the solvated Zundel complex; the band at 2600 cm^{-1} is clearly due to the Eigen cation, whereas the maximum around 3200-3300 cm^{-1} is the signature of the OH stretch for the proton when shared by two waters (Zundel structure). At condensed phases as those analyzed here, we can expect that all frequencies suffer a red shift towards lower values, in the same fashion as it happens to hydrogen vibrations in neat non-protonated water (see for instance Ref. [146]. The effect of confinement becomes

important only when the interplate distance is of (or below) 1.5 nm. In such cases, changes in the spectral bands are observed, with a tendency of bands (A) and (B) to blue-shift by some 100-200 wave numbers and to red-shift by 100 wave numbers by band (C).

2. The effect of the temperature seems to be not important at the widest interpolate separation (d = 3.1 nm) but it has some influence at d = 1.5 nm and it definitely affects the spectral bands when d = 0.7 nm. In such a case, LDA ice (200 K) shows a red shift of the signature band at 2400 cm^{-1}, whereas at temperatures of 400 and 500 K, the tendency is reversed and the shift tends to be towards higher values.
3. About Zundel-like bands, the lowest frequency one located at 1880 cm^{-1} in gas phase is absent in the liquid and LDA ice spectra, whereas the band at higher frequency around 3500 cm^{-1} appears at low frequencies in all cases. It shows a tendency to split, very marked for d = 0.7 nm, indicating the existence of Zundel dimers or, equivalently, the breaking of Eigen groups at the strongest confinement.

4.3 Summary and Conclusions

In the present chapter a thorough analysis of the structure and dynamics of an excess proton in liquid water and LDA ices has been reported based in two aqueous systems of water: (unconstrained and confined inside graphene slabs). We started with the investigations related to unconstrained water, which is a first step into the study of PT in two-dimensional systems. The system was set by tuning the water layers from full three-dimensional states to states at short interplate distances (0.7 nm wide) where water structure can be regarded as quasi-two-dimensional. The chapter reported the analyses of microscopic characteristics of an aqueous PT by employing the MD simulations together with a multidimensional empirical valence bond procedure, in order to construct a suitable Hamiltonian for the semi-classical system; formed by a quantum particle (the lone proton) embedded in a sea of classical flexible TIP3P waters. The artificial neural network approach along with statistical methods is then successfully employed to work as supplementary computational tool to simplify modeling as well as analyzing the PT properties we are interested in. PT properties were shown in this chapter based on different chart patterns extracted by our new developed and tested ANN application as it has been fully defined in chapter 3. Afterwards, the proposed tool has simply enable the technical analysis of several important chemical properties, by means of the EVB simulation output graphical data, having the aim of enhancing the performance and efficiency for systems of large amounts of molecules. These properties are: the proton transfer rate, the hydronium-water local density field and the diffusion coefficient of proton, in addition to the spectra of proton vibration, directly related with the existence Zundel and Eigen complex.

The analysis of the local structure of the hydrated proton revealed the enhancement of the local structure of the proton in LDA ices. At the lowest temperature considered in the present study (100 K), the environment of the proton typical of ambient conditions, consisting of a mixture of Zundel and Eigen-like structures has evolved to a network of water clusters mainly formed by Zundel and Eigen-like complexes whit enhanced directionality, as it can be inferred from our spectroscopical data. However, such extent of alignment between the proton and its surrounding oxygens would be less important that in the case of cubic ice Ic [80, 81]. The proton in ice-like environments remains trapped to an hydronium complex for long time intervals, given an averaged transfer time of about 50 ps, whereas at 298 K, the mean time for a proton transfer is of the order of 2 ps. However, as it has been indicated in some recent experimental findings [82, 83] PTs still occur. The activation energy for PT has been estimated to be 3.2 kJ/mol in reasonable overall agreement with experiments [163,164], which reported a value of 10 kJ/mol for proton transfer in surface ices. Diffusion of the proton tends to decrease when the system is cooled down, changing from 0.94 $\mathring{A}^2$/ps at 298 K up to a factor 6 smaller than at 100 K. Being diffusion also an activated process, we found that activation energy barriers for diffusion are lower than those of PT roughly by a factor 2.

On the other hand, in terms of our results of the investigation of the effects of confinement on the local structure and dynamics of the hydrated proton confined inside graphene slabs, our findings have revealed the enhancement of the local structure of the proton in the narrowest pores. At the quasi two-dimensional water states represented by slab's widths of d = 0.7 and 0.9 nm, the environment of the proton typical of ambient conditions, consisting of a mixture of Zundel and Eigen-like structures has evolved to a network of quasi 2D water molecules, still including Zundel and Eigen complexes but allowing the breaking of these structures in favor of a lighter species, the hydronium ion, as revealed by the existence of suitable frequency shifts toward higher values, as it can be inferred from available spectroscopical data. So, the proton in 2D water would remain trapped to an hydronium complex for quite long time intervals, given the averaged transfer time of more than 200 ps, whereas at unconstrained conditions the mean time for a proton transfer is of the order of 1–2 ps. This indicates that PT still occur, but at much shorter rates of the order of 10^{-3} ps^{-1}. Diffusion of the proton tends to decrease moderately when the system is compressed, changing from 0.94 $°\mathrm{A}^2/\mathrm{ps}$ in unconstrained bulk water up to a factor 4.5 times smaller at quasi-two-dimensional water, i.e., for d = 0.7 and 0.9 nm. Our results for diffusion coefficients agree well with those of Bankura and Chandra [66], although proton transfer rates reported in this work are significantly smaller than those from the same authors, probably due to the higher water density considered here.

Conversely, when the system is heated up, diffusion increases about a factor 3 (at 600 K). In constrained geometries, diffusion is strongly reduced at low temperatures, becoming one order of magnitude smaller than for the bulk counterparts. When we move to high temperature environments, diffusion increases in a smaller scale reaching values comparable to those of the corresponding unconstrained states. This would suggest that confinement and temperature are factors both affecting transport properties of the proton, but playing opposite roles. We have pointed out that the role of the Grotthuss mechanism should become less important at low temperatures. This was easily estimated using random walk arguments.

4.4 Future studies

As shown in this thesis confining environments with characteristic lengths at the nanometer scale were able to significantly change the equilibrium properties and dynamics associated with any reactive process in solution when studying the PT in water. In this regard, based on our results of investigating PT in pure water it will be interesting to analyze the structural properties and dynamics of solvation of an excess proton located in a nother aqueous environment, such as strong acids and ionic solutions confined in different geometries (varying from hydrophobic to hydrophilic nature). Among these a natural extension of this then would be to consider a basic model of non-hydrophobic silica plates kept at variable distances. Another extension would be to perform the selective functionalization of the walls by means of hydrophilic OH groups and study their possible effects on the solvation of protons. The future projects will essentially deal with the comparison of performance of semi-classical molecular dynamics and Car-Parrinello simulations, which incorporate an explicit treatment of quantum fluctuations. The ANN application could be used also to facilitate the work and to enable predicting and to overcome the obstacles of theoretical simulations.

Functionalization with other groups (type trimethylsilyl O-Si(CH_3)$_3$) possibly will incorporate interesting modifications in the topological disorder through modulated proton solvation. More specifically, we refer here to the related introduction of new characteristic lengths of a magnitude comparable to the size of the functional group (about 0.5 to 0.7 nm). In this regard, we expect important retarding effects on the dynamics of water in intimate contact with the groups in question. An important aspect in this context will elucidate whether protons remain in the aqueous phase or migrate to the vicinity of these groups. Given the latter possibility, certainly it would exist non-trivial modifications in the structure and dynamics of proton solvation and it would open the door to the confirmation of the existence of pH gradients in nanometer-scale cavities.

The addition of ionic species will let us gain valuable information about the influence of salts on the structure, rates and dynamics of proton transfer, allowing us to analyze the interplay between electrolyte specific effects and the effects due to confinement. Needless to say those aqueous electrolyte systems in constrained geometries play a role of central importance in a variety of processes such as corrosion, catalysis of metals or solar energy conversion, among others.

As regarding to simulation of acid dissociation in water at interfaces it will be most challenging, due to the characteristics of such processes, involving breaking of chemical bonds. For instance, when dissociation at aqueous surfaces of sulfuric and nitric acids is given, proton transfer reactions are important in various atmospheric chemistry contexts. Two of many examples of their atmospheric relevance are sulfate aerosol surfaces acting as heterogeneous reaction sites for reactions related to ozone depletion in the mid-latitude stratosphere, and the uptake of gas phase nitric acid by ice aerosols in the upper troposphere, again related to ozone depletion. Despite the fact that these acids are usually regarded as strong and readily dissociate in the more familiar room temperature, it is found that particularly nitric acid can remain molecular at an aqueous surface under a wide range of atmospherically relevant conditions [176].

About Car-Parrinello simulations, we can mention: (1) the accuracy of the functionals of density which lie at the core of the method is limited, since such functionals include a series of approximations being far from exact and (2) the computational cost is extremely high. We believe that using the two methodologies in a complementary way we can get profit from the advantages of both methods and minimize the shortcomings.

The reason of suggesting the use of Car-Parrinello technique in future studies is because of the need of achieving a high degree of accuracy in the treatment of hydrogens which the particle is showing a higher degree of quantum nature. So, at the most primary level, it will have lots of shared characteristics with those of the proton. For that reason, both the proton and hydrogens in water have to be described with high accuracy at the quantum level.

5 References

1. Tahat, A., Marti, J., Khwaldeh, A., Tahat, K. (2014). Pattern recognition and data mining software based on artificial neural networks applied to proton transfer in aqueous environments. *Chinese Physics B*, *23*(4), 046101.
2. Tahat, A., Martí, J. (2014). Dynamical aspects of intermolecular proton transfer in liquid water and low-density amorphous ices. *Physical Review E, 89*(5), 052130.
3. Tahat, A., Martí, J. (2015). Proton transfer in liquid water confined inside graphene slabs. *Physical Review E, 92*(3), 032402.
4. Tahat, A., Martí, J. (2016). Multi-state Empirical Valence Bond study of temperature and confinement effects on proton transfer in water inside hydrophobic nanochannels. Submitted to the Journal of Computational Chemistry.
5. Trylska, J., Grochowski, P., McCammon, J. A. (2004). The role of hydrogen bonding in the enzymatic reaction catalyzed by HIV-1 protease. *Protein science*, *13*(2), 513-528.
6. Gaigeot, M. P., Cimas, A., Seydou, M., Kim, J. Y., Lee, S., Schermann, J. P. (2010). Proton Transfer from the Inactive Gas-Phase Nicotine Structure to the Bioactive Aqueous-Phase Structure. *Journal of the American Chemical Society*, *132*(51), 18067-18077.
7. Müller, A., Ratajczak, H., Junge, W., Diemann, E. (1992). *Electron and proton transfer in chemistry and biology*. Elsevier Science Publishers, Amsterdam.
8. Hammer, N. I., Diken, E. G., Roscioli, J. R., Johnson, M. A., Myshakin, E. M., Jordan, K. D., Carter, S. (2005). The vibrational predissociation spectra of the H5O2+ RGn (RG= Ar, Ne) clusters: correlation of the solvent perturbations in the

free OH and shared proton transitions of the Zundel ion. *The Journal of Chemical Physics*, *122*(24), 244301-244301.

9. Headrick, J. M., Diken, E. G., Walters, R. S., Hammer, N. I., Christie, R. A., Cui, J., Jordan, K. D. (2005). Spectral signatures of hydrated proton vibrations in water clusters. *Science, 308*(5729), 1765-1769.
10. Wu, Y., Voth, G. A. (2003). A computer simulation study of the hydrated proton in a synthetic proton channel. *Biophysical Journal*, *85*(2), 864-875.
11. Elliott, J. A., Paddison, S. J. (2007). Modelling of morphology and proton transport in PFSA membranes. *Physical Chemistry Chemical Physics*, *9*(21), 2602-2618.
12. Trylska, J., Grochowski, P., McCammon, J. A. (2004). The role of hydrogen bonding in the enzymatic reaction catalyzed by HIV-1 protease. *Protein Science*, *13*(2), 513-528.
13. Dayhoff, J. E., DeLeo, J. M. (2001). Artificial neural networks. *Cancer*, *91*(S8), 1615-1635.
14. Andreas, S., Jörg, B., Christoph D. (2015). Proton Transfer Reactions in Liquid Water by Artificial Neural Network proceeding of "From trajectories to reaction coordinates: making sense of molecular simulation data. CECAM-AT, Erwin Schrödinger Institute, University of Vienna, Austria.
15. Natarajan, S. K., Morawietz, T., Behler, J. (2015). Representing the potential-energy surface of protonated water clusters by high-dimensional neural network potentials. *Physical Chemistry Chemical Physics*, *17*(13), 8356-8371.
16. Geissler, P. L., Dellago, C., Chandler, D., Hutter, J., Parrinello, M. (2001). Autoionization in liquid water. *Science*, *291*(5511), 2121-2124.
17. Hollis, J. M., Churchwell, E. B., Herbst, E., De Lucia, F. C. (1986). An interstellar line coincident with the P (2, 1) transition of hydronium (H3O+). *Nature*, *322*(6079), 524-526.
18. Wang, C., Waje, M., Wang, X., Tang, J. M., Haddon, R. C., Yan, Y. (2004). Proton exchange membrane fuel cells with carbon nanotube based electrodes. *Nano letters*, *4*(2), 345-348.

19. Spry, D. B., Goun, A., Glusac, K., Moilanen, D. E., Fayer, M. D. (2007). Proton transport and the water environment in nafion fuel cell membranes and aot reverse micelles. *Journal of the American Chemical Society*, *129*(26), 8122-8130.
20. Bianco, R., Hynes, J. T. (2004). A theoretical study of the $H_2SO_4^+$ $H_2O\rightarrow$ HSO_4^-+ H_3O^+ reaction at the surface of aqueous aerosols. *Theoretical Chemistry Accounts*, *111*(2-6), 182-187.
21. Smondyrev, A. M., Voth, G. A. (2002). Molecular dynamics simulation of proton transport near the surface of a phospholipid membrane. *Biophysical journal*, *82*(3), 1460-1468.
22. Dellago, C., Naor, M. M., Hummer, G. (2003). Proton transport through water-filled carbon nanotubes. *Physical Review Letters*, *90*(10), 105902.
23. G. Hummer. (2007) “Water, proton, and ion transport: from nanotubes to proteins,” *Mol. Phys.*, vol. 105, p. 201.
24. Kreuer, K. D., Paddison, S. J., Spohr, E., Schuster, M. (2004). Transport in proton conductors for fuel-cell applications: simulations, elementary reactions, and phenomenology. *Chemical Reviews, 104*(10), 4637-4678.
25. De Grotthuss*, C.J.T.* (1806). *"Sur la décomposition de l'eau et des corps qu'elle tient en dissolution à l'aide de l'électricité galvanique". Ann. Chim. (Paris) 58: 54–73*
26. Marx, D. (2006). Proton transfer 200 years after von Grotthuss: Insights from ab initio simulations. *ChemPhysChem*, *7*(9), 1848-1870.
27. Agmon, N. (1995). The grotthuss mechanism. *Chemical Physics Letters*, *244*(5), 456-462.
28. Maurice L. Huggins. (1931). The role of hydrogen bonds in conduction by hydrogen and hydroxyl ions. *J. Am. Chem. Soc.*, 53:3190–3191.
29. B. Conway, J. Bockris, and H. Linton. (1956) “Proton conductance and the existence of the H_3O+ ion,” *J. Chem. Phys.*, vol. 24, p. 834.
30. J. Bernal and R. Fowler. (1933) “A theory of water and ionic solution, with particular reference to hydrogen and hydroxil ions,” *J. Chem. Phys.*, vol. 1, p. 515.

31. Huggins, M. L. (1936). Hydrogen bridges in ice and liquid water. *The Journal of Physical Chemistry*, *40*(6), 723-731.
32. G Zundel and H Metzger. (1968). Energy bands of excess tunneling protons in fluid acids. ir spectroscopy of h5o+2 groups. *Z. Phys. Chem. (N. F. Frankfurt)*, 58:225 245.
33. M. Eigen. (1964) "Proton transfer, acid-base catalysis, and enzymatic hydrolysis. Part I: elementary processes," *Angew. Chem. Int. Edn.*, vol. 3, p. 1.
34. Eigen, M., De Maeyer, L. (1958). Self-dissociation and protonic charge transport in water and ice. *Proceedings of the Royal Society of London. Series A, Mathematical and Physical Sciences*, 505-533.
35. Wu, Y., Chen, H., Wang, F., Paesani, F., Voth, G. A. (2008). An improved multistate empirical valence bond model for aqueous proton solvation and transport. *The Journal of Physical Chemistry B*, *112*(2), 467-482.
36. Wu, Y., Tepper, H. L., Voth, G. A. (2006). Flexible simple point-charge water model with improved liquid-state properties. *The Journal of Chemical Physics*, *124*(2), 024503.
37. Markovitch, O., Chen, H., Izvekov, S., Paesani, F., Voth, G. A., Agmon, N. (2008). Special pair dance and partner selection: Elementary steps in proton transport in liquid water. *The Journal of Physical Chemistry B*, *112*(31), 9456-9466.
38. Knight, C., Voth, G. A. (2011). The curious case of the hydrated proton. *Accounts of Chemical Research*, *45*(1), 101-109.
39. Tuckerman, M., Laasonen, K., Sprik, M., Parrinello, M. (1995). Abinitio molecular dynamics simulation of the solvation and transport of hydronium and hydroxyl ions in water. *The Journal of Chemical Physics*, ***103*****(1),** 150-161.
40. Tuckerman, M., Laasonen, K., Sprik, M., Parrinello, M. (1995). Ab initio molecular dynamics simulation of the solvation and transport of H_3O^+ and OH^- ions in water. *The Journal of Physical Chemistry*, ***99*****(16),** 5749-5752.
41. Lum, K., Chandler, D., Weeks, J. D. (1999). Hydrophobicity at small and large length scales. *The Journal of Physical Chemistry B*, *103*(22), 4570-4577.

42. Lin, M. Y., Sinha, S. K., Drake, J. M., Wu, X. L., Thiyagarajan, P., Stanley, H. B. (1994). Study of phase separation of a binary fluid mixture in confined geometry. *Physical Review Letters*, *72*(14), 2207.
43. Martí, J., Gordillo, M. C. (2001). Effects of confinement on the vibrational spectra of liquid water adsorbed in carbon nanotubes. *Physical Review B*, *63*(16), 165430.
44. Videla, P. E., Sala, J., Martí, J., Guàrdia, E., Laria, D. (2011). Aqueous electrolytes confined within functionalized silica nanopores. *The Journal of Chemical Physics*, *135*(10), 104503.
45. Liu, C., Fan, Y. Y., Liu, M., Cong, H. T., Cheng, H. M., Dresselhaus, M. S. (1999). Hydrogen storage in single-walled carbon nanotubes at room temperature. *Science*, *286*(5442), 1127-1129.
46. Singh, R., Pantarotto, D., Lacerda, L., Pastorin, G., Klumpp, C., Prato, M., Kostarelos, K. (2006). Tissue biodistribution and blood clearance rates of intravenously administered carbon nanotube radiotracers. *Proceedings of the National Academy of Sciences of the United States of America*, *103*(9), 3357-3362.
47. Pizzitutti, F., Marchi, M., Sterpone, F., Rossky, P. J. (2007). How protein surfaces induce anomalous dynamics of hydration water. *The Journal of Physical Chemistry B*, *111*(26), 7584-7590.
48. Pal, S. K., Zhao, L., Zewail, A. H. (2003). Water at DNA surfaces: ultrafast dynamics in minor groove recognition. *Proceedings of the National Academy of Sciences*, *100*(14), 8113-8118.
49. Giovambattista, N., Lopez, C. F., Rossky, P. J., Debenedetti, P. G. (2008). Hydrophobicity of protein surfaces: Separating geometry from chemistry. *Proceedings of the National Academy of Sciences*, *105*(7), 2274-2279.
50. Rodriguez, J., Martí, J., Guàrdia, E., Laria, D. (2007). Protons in non-ionic aqueous reverse micelles. *The Journal of Physical Chemistry B*, *111*(17), 4432-4439.
51. Le Caër, S., Palmer, D. J., Lima, M., Renault, J. P., Vigneron, G., Righini, R., Pommeret, S. (2007). Time-resolved studies of water dynamics and proton

transfer at the alumina-air interface. *Journal of the American Chemical Society*, *129*(38), 11720-11729.

52. Spry, D. B., Goun, A., Glusac, K., Moilanen, D. E., Fayer, M. D. (2007). Proton transport and the water environment in nafion fuel cell membranes and aot reverse micelles. *Journal of the American Chemical Society*, *129*(26), 8122-8130.
53. Thämer, M., De Marco, L., Ramasesha, K., Mandal, A., Tokmakoff, A. (2015). Ultrafast 2D IR spectroscopy of the excess proton in liquid water. *Science*, *350*(6256), 78-82.
54. Chaplin, M. F. (2010). Structuring and behaviour of water in nanochannels and confined spaces. In *Adsorption and phase behaviour in nanochannels and nanotubes* (pp. 241-255). Springer Netherlands.
55. Fouzri, A., Dorbez-Sridi, R., Nasr, S., Oumezzine, M. (2002). Water–silica gel interactions, X-ray diffraction study at room and low temperature. *Biomolecular Engineering*, *19*(2), 207-210.
56. Nair, R. R., Wu, H. A., Jayaram, P. N., Grigorieva, I. V., Geim, A. K. (2012). Unimpeded permeation of water through helium-leak–tight graphene-based membranes. *Science*, *335*(6067), 442-444.
57. Novoselov, K. S., Geim, A. K., Morozov, S. V., Jiang, D., Zhang, Y., Dubonos, S. A., Firsov, A. A. (2004). Electric field effect in atomically thin carbon films. *Science*, *306*(5696), 666-669.
58. Yamada, Y., Yasuda, H., Murota, K., Nakamura, M., Sodesawa, T., Sato, S. (2013). Analysis of heat-treated graphite oxide by X-ray photoelectron spectroscopy. *Journal of Materials Science*, *48*(23), 8171-8198.
59. Yamada, Y., Kim, J., Matsuo, S., Sato, S. (2014). Nitrogen-containing graphene analyzed by X-ray photoelectron spectroscopy. *Carbon*, *70*, 59-74.
60. Wallace, P. R. (1947). The band theory of graphite. *Physical Review*, *71*(9), 622.
61. Boehm, H. P., Clauss, A., Fischer, G. O., Hofmann, U. (1962). Das adsorptionsverhalten sehr dünner kohlenstoff-folien. *Zeitschrift für Anorganische und Allgemeine Chemie*, *316*(3-4), 119-127.
62. Geim, A. K., Novoselov, K. S. (2007). The rise of graphene. *Nature Materials*, *6*(3), 183-191.

63. Diankov, G., Neumann, M., Goldhaber-Gordon, D. (2013). Extreme monolayer-selectivity of hydrogen-plasma reactions with graphene. *ACS Nano*, *7*(2), 1324-1332.
64. Chen, H., Müller, M. B., Gilmore, K. J., Wallace, G. G., Li, D. (2008). Mechanically strong, electrically conductive, and biocompatible graphene paper. *Advanced Materials*, *20*(18), 3557-3561.
65. Balandin, A. A., Ghosh, S., Bao, W., Calizo, I., Teweldebrhan, D., Miao, F., Lau, C. N. (2008). Superior thermal conductivity of single-layer graphene. *Nano letters*, *8*(3), 902-907.
66. Bankura, A., Chandra, A. (2015). Proton transfer through hydrogen bonds in two-dimensional water layers: A theoretical study based on ab initio and quantum-classical simulations. *The Journal of Chemical Physics*, *142*(4), 044701.
67. Day, T. J., Schmitt, U. W., Voth, G. A. (2000). The mechanism of hydrated proton transport in water. *Journal of the American Chemical Society*, *122*(48), 12027-12028.
68. Walbran, S., Kornyshev, A. A. (2001). Proton transport in polarizable water. *The Journal of Chemical Physics*, *114*(22), 10039-10048.
69. Kornyshev, A. A., Kuznetsov, A. M., Spohr, E., Ulstrup, J. (2003). Kinetics of proton transport in water. *The Journal of Physical Chemistry B*, *107*(15), 3351-3366.
70. A. Warshel. (1991). Computer Modeling of Chemical Reactions in Enzymes and Solutions, J. Wiley and Sons, Inc., New York.
71. Day, T. J., Soudackov, A. V., Čuma, M., Schmitt, U. W., Voth, G. A. (2002). A second generation multistate empirical valence bond model for proton transport in aqueous systems. *The Journal of Chemical Physics*, *117*(12), 5839-5849.
72. Wang, F., Voth, G. A. (2005). A linear-scaling self-consistent generalization of the multistate empirical valence bond method for multiple excess protons in aqueous systems. *The Journal of Chemical Physics*, *122*(14), 144105.
73. Warshel, A., Weiss, R. M. (1980). An empirical valence bond approach for comparing reactions in solutions and in enzymes. *Journal of the American Chemical Society*, *102*(20), 6218-6226.

74. Lobaugh, J., Voth, G. A. (1996). The quantum dynamics of an excess proton in water. *The Journal of Chemical Physics*, *104*(5), 2056-2069.
75. Vuilleumier, R., Borgis, D. (1999). Transport and spectroscopy of the hydrated proton: a molecular dynamics study. *The Journal of Chemical Physics*, *111*(9), 4251-4266.
76. Vendrell, O., Gatti, F., Meyer, H. D. (2007). Dynamics and infrared spectroscopy of the protonated water dimer. *Angewandte Chemie International Edition*, *46*(36), 6918-6921.
77. Roscioli, J. R., McCunn, L. R., Johnson, M. A. (2007). Quantum structure of the intermolecular proton bond. *Science*, *316*(5822), 249-254.
78. Collier, W. B., Ritzhaupt, G., Devlin, J. P. (1984). Spectroscopically evaluated rates and energies for proton transfer and Bjerrum defect migration in cubic ice. *The Journal of Physical Chemistry*, *88*(3), 363-368.
79. Devlin, J. P., Uras, N., Sadlej, J., Buch, V. (2002). Discrete stages in the solvation and ionization of hydrogen chloride adsorbed on ice particles. *Nature*, *417*(6886), 269-271.
80. Kobayashi, C., Saito, S., Ohmine, I. (2000). Mechanism of fast proton transfer in ice: Potential energy surface and reaction coordinate analyses. *The Journal of Chemical Physics*, *113*(20), 9090-9100.
81. Kobayashi, C., Saito, S., Ohmine, I. (2001). Mechanism of proton transfer in ice. II. Hydration, modes, and transport. *The Journal of Chemical Physics*, *115*(10), 4742-4749.
82. Lee, C. W., Lee, P. R., Kim, Y. K., Kang, H. (2007). Mechanistic study of proton transfer and H/D exchange in ice films at low temperatures (100-140K). *Journal of Chemical Physics*, *127*(8), 84701-84701.
83. Kim, J. H., Kim, Y. K., Kang, H. (2009). Proton transfer and H/D isotopic exchange of water molecules mediated by hydroxide ions on ice film surfaces. *The Journal of Chemical Physics*, *131*(4), 044705.
84. Moon, E. S., Kim, Y., Shin, S., Kang, H. (2012). Asymmetric transport efficiencies of positive and negative ion defects in amorphous ice. *Physical Review Letters*, *108*(22), 226103.

85. Natarajan, S. K., Morawietz, T., Behler, J. (2015). Representing the potential-energy surface of protonated water clusters by high-dimensional neural network potentials. *Physical Chemistry Chemical Physics, 17*(13), 8356-8371.
86. Jain, A. K., Duin, R. P., Mao, J. (2000). Statistical pattern recognition: A review. *Pattern Analysis and Machine Intelligence, IEEE Transactions on, 22*(1), 4-37.
87. Neĭmark, I. I., Neimark, J. I. (2003). *Mathematical Models in Natural Science and Engineering: An Example-Based Approach*. Springer Science & Business Media.
88. Robert, C. (1999). *The Essence of Neural Networks*. Pearson Education India.
89. Ripley, B. D. (2007). *Pattern recognition and neural networks*. Cambridge university press. New York.
90. Denby, B. (1999). Neural networks in high energy physics: A ten year perspective. *Computer Physics Communications, 119*(2), 219-231.
91. Rajagopalan, B., Krovi, R. (2002). Data Mining Algorithms. *Data Warehousing and Web Engineering*, 77.
92. Abachi, S., Abbott, B., Abolins, M., Acharya, B. S., Adam, I., Adams, D. L., Alvarez, G. (1995). Observation of the top quark. *Physical Review Letters*, *74*(14), 2632.
93. Abbott, B., Abolins, M., Acharya, B. S., Adam, I., Adams, D. L., Adams, M., Amos, N. (1997). Search for scalar leptoquark pairs decaying to electrons and jets in p̄ p collisions. *Physical Review Letters*, *79*(22), 4321.
94. Meng-Hua, Z., Liang-Gang, L., Ao-Ao, X., Tao, M. (2008). Automatic estimation of peak regions in gamma-ray spectra measured by NaI detector. *Chinese Physics Letters, 25*(11), 3942.
95. Naresh, R., Sharma, J. (2000). Hydro system scheduling using ANN approach. *Power Systems, IEEE Transactions on, 15*(1), 388-395.
96. Reed, R. D., Marks, R. J. (1998). *Neural smithing: supervised learning in feedforward artificial neural networks*. Mit Press, Cambridge, MA.
97. Patterson, D. W. (1998). *Artificial neural networks: theory and applications*. Prentice Hall PTR. Upper Saddle River, NJ, USA.
98. McCulloch, W. S., Pitts, W. (1943). A logical calculus of the ideas immanent in nervous activity. *The Bulletin of Mathematical Biophysics*, *5*(4), 115-133.

99. Abreu, P. (1999). DELPHI Collaboration: Measurement of A^ b^ b~ F~ B in hadronic Z decays using a jet charge technique. *European Physical Journal C* particles and fields, 9, 367-382.
100. Ze-Bing, Z., Shi-Fang, W.,Jun, L. (2005). Time-Domain Smoothing Processing for Equivalence-Principle Test Using Free-Fall Method. *Chinese Physics Letters*, *22* (7), 1614.
101. Amato, F., López, A., Peña-Méndez, E. M., Vaňhara, P., Hampl, A.,Havel, J. (2013). Artificial neural networks in medical diagnosis. *Journal of Applied Biomedicine*, *11*(2), 47-58.
102. Hynes, J. T., Klinman, J. P., Limbach, H. H.,Schowen, R. L. (2007). Hydrogen-transfer reactions. Wiley-VCH; Weinheim.
103. Hinchliffe, A. (2008). *Chemical modelling: applications and theory* (Vol. 5). Royal Society of Chemistry. Wiley-Blackwell. Oxford.
104. Bishop, C. M. (1995). *Neural networks for pattern recognition*. Oxford university press. New York.
105. Duda, R. O., Hart, P. E.,Stork, D. G. (2012). *Pattern classification*. John Wiley and Sons. New York.
106. Handley, C. M.,Popelier, P. L. (2010). Potential energy surfaces fitted by artificial neural networks. *The Journal of Physical Chemistry A*, *114*(10), 3371-3383.
107. Lorenz, S., Scheffler, M.,Gross, A. (2006). Descriptions of surface chemical reactions using a neural network representation of the potential-energy surface. *Physical Review B*, *73*(11), 115431.
108. Behler, J. (2011). Neural network potential-energy surfaces in chemistry: a tool for large-scale simulations. *Physical Chemistry Chemical Physics*, *13*(40), 17930-17955.
109. Behler, J. (2010). Neural network potential-energy surfaces for atomistic simulations. *Chemical Modelling: Applications and Theory*, *7*, 1.
110. Benedict, M.,Maguire, J. F. (2004). Molecular dynamics simulation of nanomaterials using an artificial neural net. *Physical Review B*, *70*(17), 174112.

111. Handley, C. M.,Popelier, P. L. (2009). Dynamically polarizable water potential based on multipole moments trained by machine learning. *Journal of Chemical Theory and Computation*, *5*(6), 1474-1489.
112. Allen, M. P. (2004). Introduction to molecular dynamics simulation. *Computational Soft Matter: From Synthetic Polymers to Proteins*, *23*, 1-28.
113. Ciccotti, G., Ferrario, M.,Ryckaert, J. P. (1982). Molecular dynamics of rigid systems in cartesian coordinates A general formulation. *Molecular Physics*, *47*(6), 1253-1264.
114. Haile, J. M. (1992). *Molecular dynamics simulation* (Vol. 18). Wiley, New York.
115. Rapaport, D. C. (2004). *The art of molecular dynamics simulation*. Cambridge university press. New York, NY, USA.
116. Van Gunsteren, W. F.,Berendsen, H. J. (1990). Computer simulation of molecular dynamics: Methodology, applications, and perspectives in chemistry. *Angewandte Chemie International Edition in English*, *29*(9), 992-1023.
117. Heermann, D. W. (1990). *Computer-Simulation Methods* (pp. 8-12). Springer Berlin Heidelberg.
118. Gallavotti, G. (Ed.). (2007). *The Fermi-Pasta-Ulam problem: a status report* (Vol. 728). Springer. Berlin Heidelberg.
119. Rahman, A. (1964). Correlations in the motion of atoms in liquid argon. *Physical Review*, *136*(2A), A405.
120. Verlet, L. (1967). Computer" experiments" on classical fluids. Thermodynamical properties of Lennard-Jones molecules. *Physical Review*, *159*(1), 98.
121. Berendsen, H. J., Postma, J. V., van Gunsteren, W. F., DiNola, A. R. H. J., Haak, J. R. (1984). Molecular dynamics with coupling to an external bath. *The Journal of Chemical Physics*, *81*(8), 3684-3690.
122. Hünenberger, P. H. (2005). Thermostat algorithms for molecular dynamics simulations. In *Advanced computer simulation* (pp. 105-149). Springer Berlin Heidelberg.
123. MacKerell Jr, A. D. (2007). Empirical Force Fields. In *Computational Methods for Protein Structure Prediction and Modeling* (pp. 45-69). Springer. New York.

124. Dang, L. X., Pettitt, B. M. (1987). Simple intramolecular model potentials for water. *Journal of Physical Chemistry*, *91*(12), 3349-3354.
125. Frenkel, D., Smit, B. (2001). *Understanding molecular simulation: from algorithms to applications*. Academic press. London.
126. Lorentz, H. A. (1881). Ueber die Anwendung des Satzes vom Virial in der kinetischen Theorie der Gase. *Annalen der Physik*, *248*(1), 127-136.
127. Berthelot, D. (1898). Sur le mélange des gaz. *Compt. Rendus*, *126*, 1703-1706.
128. Gordillo, M. C., Marti, J. (2000). Hydrogen bond structure of liquid water confined in nanotubes. *Chemical Physics Letters*, *329*(5), 341-345.
129. Schmitt, U. W., Voth, G. A. (1998). Multistate empirical valence bond model for proton transport in water. *The Journal of Physical Chemistry B, 102*(29), 5547-5551.
130. Schmitt, U. W., Voth, G. A. (1999). The computer simulation of proton transport in water. *The Journal of Chemical Physics*, *111*(20), 9361-9381.
131. Wick, C. D., Xantheas, S. S. (2008). Computational Investigation of the First Solvation Shell Structure of Interfacial and Bulk Aqueous Chloride and Iodide Ions. *The Journal of Physical Chemistry B*, *113*(13), 4141-4146.
132. Vega, C., Abascal, J. L., Conde, M. M., Aragones, J. L. (2009). What ice can teach us about water interactions: a critical comparison of the performance of different water models, *Faraday Discussions*, *141*, 251- 276.
133. Haykin, S., Network, N. (2004). A comprehensive foundation. *Neural Networks*, *2*(2004).
134. Aleksander, I., Morton, H. (1990). *An introduction to neural computing* (Vol. 240). Chapman and Hall. London.
135. Richard, M. D., Lippmann, R. P. (1991). Neural network classifiers estimate Bayesian a posteriori probabilities. *Neural Computation*, *3*(4), 461-483.
136. Rumelhart, D. E., Hinton, G. E., Williams, R. J. (1985). Learning internal representations by error propagation. University of California. San Diego.
137. Laria, D., Martí, J., Guàrdia, E. (2004). Protons in supercritical water: a multistate empirical valence bond study. *Journal of the American Chemical Society*, *126*(7), 2125-2134.

138. Chandler, D. (1987). Introduction to modern statistical mechanics. *Oxford University Press*, New York.
139. Semino, R., Laria, D. (2012). Excess protons in water-acetone mixtures. *The Journal of Chemical physics*, *136*(19), 194503.
140. Wolf, M. G., Groenhof, G. (2014). Explicit proton transfer in classical molecular dynamics simulations. *Journal of Computational Chemistry*, *35*(8), 657-671.
141. Freeman, J. A., Skapura, D. M. (1991). *Algorithms, Applications, and Programming Techniques*. Addison-Wesley Publishing Company, Reading, MA.
142. Robinson, R. A., Stokes, R. H. (1959). Electrolyte Solutions, Butter-worths, London.
143. Krynicki, K., Green, C. D., Sawyer, D. W. (1978). Pressure and temperature dependence of self-diffusion in water. *Faraday Discussions of the Chemical Society, 66*, 199-208.
144. Kim, J., Schmitt, U. W., Gruetzmacher, J. A., Voth, G. A., & Scherer, N. E. (2002). The vibrational spectrum of the hydrated proton: Comparison of experiment, simulation, and normal mode analysis. *The Journal of Chemical Physics*, *116*(2), 737-746.
145. Lippmann, R. P. (1987). An introduction to computing with neural nets. *ASSP Magazine, IEEE*, *4*(2), 4-22.
146. Eisenberg, D. S., Kauzmann, W. (1969). *The structure and properties of water* (Vol. 123). Clarendon Press. Oxford.
147. Voth, G. A. (2006). Computer simulation of proton solvation and transport in aqueous and biomolecular systems. *Accounts of Chemical Research*, *39*(2), 143-150.
148. Von Hippel, A. (1988). The dielectric relaxation spectra of water, ice, and aqueous solutions, and their interpretation. III. Proton organization and proton transfer in ice. *Electrical Insulation, IEEE Transactions on*, *23*(5), 825-840.
149. Hummer, G., Rasaiah, J. C., Noworyta, J. P. (2001). Water conduction through the hydrophobic channel of a carbon nanotube. *Nature*, *414*(6860), 188-190.

150. Cao, Z., Peng, Y., Yan, T., Li, S., Li, A., Voth, G. A. (2010). Mechanism of fast proton transport along one-dimensional water chains confined in carbon nanotubes. *Journal of the American Chemical Society, 132*(33), 11395-11397.
151. Clark II, J. K., Paddison, S. J. (2014). Ab initio molecular dynamics simulations of water and an excess proton in water confined in carbon nanotubes. *Physical Chemistry Chemical Physics*, *16*(33), 17756-17769.
152. Achtyl, J. L., Unocic, R. R., Xu, L., Cai, Y., Raju, M., Zhang, Wesolowski, D. J. (2015). Aqueous proton transfer across single-layer graphene. *Nature Communications*, *6*.
153. Cheng, T. C., Bandyopadhyay, B., Mosley, J. D., Duncan, M. A. (2012). IR Spectroscopy of Protonation in Benzene–Water Nanoclusters: Hydronium, Zundel, and Eigen at a Hydrophobic Interface. *Journal of the American Chemical Society*, *134*(31), 13046-13055.
154. Wang, H., Agmon, N. (2015). Protonated water dimer on benzene: standing eigen or crouching zundel?. *The Journal of Physical Chemistry B, 119*(6), 2658-2667.
155. Botti, A., Bruni, F., Imberti, S., Ricci, M. A., Soper, A. K. (2004). Ions in water: The microscopic structure of a concentrated HCl solution. *The Journal of Chemical Physics, 121*(16), 7840-7848.
156. Botti, A., Bruni, F., Ricci, M. A., Soper, A. K. (2006). Eigen versus Zundel complexes in HCl-water mixtures. *The Journal of Chemical Physics*, *125*(1), 014508.
157. Marti, J., Nagy, G., Guàrdia, E., Gordillo, M. C. (2006). Molecular dynamics simulation of liquid water confined inside graphite channels: dielectric and dynamical properties. *The Journal of Physical Chemistry B*, *110*(47), 23987-23994.
158. Zhang, C., Knyazev, D. G., Vereshaga, Y. A., Ippoliti, E., Nguyen, T. H., Carloni, P., Pohl, P. (2012). Water at hydrophobic interfaces delays proton surface-to-bulk transfer and provides a pathway for lateral proton diffusion. *Proceedings of the National Academy of Sciences*, *109*(25), 9744-9749.

159. Kumar, R., Knight, C., Voth, G. A. (2013). Exploring the behaviour of the hydrated excess proton at hydrophobic interfaces. *Faraday Discussions*, *167*, 263-278.
160. Gordillo, M. C., Nagy, G., Marti, J. (2005). Structure of water nanoconfined between hydrophobic surfaces. *The Journal of Chemical Physics*, *123*(5), 054707.
161. Meiboom, S. (1961). Nuclear magnetic resonance study of the proton transfer in water. *The Journal of Chemical Physics*, *34*(2), 375-388.
162. Pfeifer, R., Hertz, H. G. (1990). Activation Energies of the Proton-exchange Reactions in Water Measured with the 1H-NMR Spin Echo Technique. *Berichte der Bunsengesellschaft für physikalische Chemie*, *94*(11), 1349-1353.
163. Moon, E. S., Yoon, J., Kang, H. (2010). Energy barrier of proton transfer at ice surfaces. *The Journal of Chemical Physics*, *133*(4), 044709.
164. Park, S. C., Moon, E. S., Kang, H. (2010). Some fundamental properties and reactions of ice surfaces at low temperatures. *Physical Chemistry Chemical Physics*, *12*(38), 12000-12011.
165. Luz, Z., Meiboom, S. (1964). The activation energies of proton transfer reactions in water. *Journal of the American Chemical Society*, *86*(22), 4768-4769.
166. Hertz, H.G.(1973). In water: A comprehensive Treatise, Vol.3.Edited by F. Franks. Plenum Press, New York.
167. Marti, J., Padró, J. A., Guàrdia, E. (1995). A molecular dynamics study of heavy water steam. *Molecular Physics*, *86*(2), 263-271.
168. Marti, J., Padró, J. A.,Guàrdia, E. (1996). Molecular dynamics simulation of liquid water along the coexistence curve: Hydrogen bonds and vibrational spectra. *The Journal of Chemical Physics*, *105*(2), 639-649.
169. Schwarz, H. A. (1977). Gas phase infrared spectra of oxonium hydrate ions from 2 to 5 μ. *The Journal of Chemical Physics*, *67*(12), 5525-5534.
170. Okumura, M., Yeh, L. I., Myers, J. D., Lee, Y. T. (1990). Infrared spectra of the solvated hydronium ion: Vibrational predissociation spectroscopy of mass selected H3O+. (H2O). (H2). *Journal of Physical Chemistry*, *94*(9), 3416-3427.

171. Asmis, K. R., Pivonka, N. L., Santambrogio, G., Brümmer, M., Kaposta, C., Neumark, D. M., Wöste, L. (2003). Gas-phase infrared spectrum of the protonated water dimer. *Science*, *299*(5611), 1375-1377.
172. Chen, S. H., Toukan, K., Loong, C. K., Price, D. L., & Teixeira, J. (1984). Hydrogen-bond spectroscopy of water by neutron scattering. *Physical Review Letters*, *53*(14), 1360.
173. Hertz, H. G. (1983). Search for Fast H+-Ion Motion in Aqueous Solutions of HCl. *Zeitschrift für Physikalische Chemie*, *135*(135), 89-105.
174. Esai Selvan, M., Keffer, D. J., Cui, S., Paddison, S. J. (2010). Proton transport in water confined in carbon nanotubes: a reactive molecular dynamics study. *Molecular Simulation*, *36*(7-8), 568-578.
175. Habenicht, B. F., Paddison, S. J., Tuckerman, M. E. (2010). The effects of the hydrophobic environment on proton mobility in perfluorosulfonic acid systems: an ab initio molecular dynamics study. *Journal of Materials Chemistry*, *20*(30), 6342-6351.
176. Bianco, R., Wang, S., Hynes, J. T. (2008). Theoretical studies of the dissociation of sulfuric acid and nitric acid at model aqueous surfaces. *Advances in Quantum Chemistry*, *55*, 387-405.

6 List of contributions of this thesis:

The work on this thesis has given rise to the following publications:

1. Tahat, A., Marti, J., Khwaldeh, A., Tahat, K. (2014). Pattern recognition and data mining software based on artificial neural networks applied to proton transfer in aqueous environments. *Chinese Physics B*, *23*(4), 046101.
2. Tahat, A., & Martí, J. (2014). Dynamical aspects of intermolecular proton transfer in liquid water and low-density amorphous ices. *Physical Review E*, *89*(5), 052130.
3. Tahat, A., & Martí, J. (2015). Proton transfer in liquid water confined inside graphene slabs. *Physical Review E*, *92*(3), 032402.
4. Multi-state Empirical Valence Bond study of temperature and confinement effects on proton transfer in water inside hydrophobic nanochannels. Submitted to Journal of Computational Chemistry (2016).